Universidade do Minho
Escola de Engenharia

Vítor Manuel Gomes Correia

Development of piezoresistive sensors for biomedical applications

Março de 2013

Vítor Manuel Gomes Correia

Development of piezoresistive
sensors for biomedical applications

UMinho | 2013

Universidade do Minho
Escola de Engenharia

Vítor Manuel Gomes Correia

Development of piezoresistive sensors for biomedical applications

Tese de Doutoramento
Engenharia Electrónica Industrial e de Computadores

Trabalho efectuado sob a orientação do
Professor Doutor José V. Gerado Rocha
Professor Doutor Senentxu Lanceros-Mendez

Março de 2013

Acknowledgements

First words to be written…

During the journey of my PhD, several people have contributed in the most different ways to make this moment possible. So, I cannot conclude this relevant step of my life without expressing my gratitude and my appreciation to all those that directly and indirectly have contributed to the development of this work throughout all these years and that helped me to grow as a person and as a professional.

My first acknowledgment is for my supervisor Prof. Gerardo Rocha, for encouraging me in the continuation of my academic career and for the opportunity to accompany him all these years as a teacher and as a friend. Thank you for your friendship.

To my co-supervisor, Prof. Senentxu, for giving me the opportunity of being a part of a fantastic research group due to scientific knowledge, work methodology, ideas, availability, shared knowledge and most of all, the friendship revealed over all these years. Thank you for your friendship and sharing of experiences.

I would like to mention my colleagues/friends of Electroactive Smart Materials group for helping me along this time, always with a constructive and mutual aid spirit. In particular to Marcos Martins for his help in simulations; Vítor Sencadas for his help in the biomechanical tests; Armando for his help with the depositions techniques; Silvia Reis, Cristina and Helder for their support and friendship.

I want to thank the financial support by the Foundation for Science and Technology-FCT under grant SFRH/BD/48708/2008.

To colleagues and researchers at Cetemmsa for the excellent reception and availability during my stay for the development of printed sensors.

I would like to thank the researchers at the Instituto de Biomecánica de Valencia (IBV) for the excellent reception and availability during my stay for the development of biomechanical tests.

I also acknowledge the INL- International Iberian Nanotechnology Laboratory for their support.

Very special thanks to my parents for everything that have done for me, for all you tried to do and for all that will be done for me. What I am today I owe it to you.

I want to thank to my brothers Ramiro, Ana and Rui for the support, inspiration and motivation they gave me.

Lastly but most important of all, I thank to my wife Goreti that has been always my support, my refuge, my inspiration, my joy and my love. Love you! :)

I dedicate this work to

Goreti, my brothers and my parents,

Thanks

Abstract

In the last decades there has been an increase in sensing systems applied in a variety of situations with a large variety of sensor ranges. This represents a growing area with high potential.

One of the areas of sensor development that require a great deal of attention is the area of sensor for biomedical applications and biosensors.

These sensors have to overcome a number of challenges and limitations inherent to the environment where they are introduced. These difficulties lead to the necessity of using new materials and new techniques for their construction together with the more traditional materials, e.g. silicon based, which have already proven their potential in this area. Among the various materials, polymers have proven to be a good choice, due to a set of advantages such as simple processing, flexibility and facility of being obtained in different shapes. Therefore it is interesting to fabricate polymer based piezoresistive sensors for functional coatings of implantable hip prosthesis.

These sensors will allow coating the prosthesis and provide new functionalities to the implants such as the possibility to measure forces and deformations between the prosthesis and the bone and therefore improving the postoperative diagnostic.

In this works, a model of hip prosthesis with coated sensors was developed. For this purpose, flexible piezoresistive sensors have been developed that allow being implanted. Strain sensors were fabricated based on thin films of n^+-nc-si.H by the technique of hot-wire chemical vapor deposition at a temperature of 150 ºC on a polymeric substrate, using the lithographic technique to construct the various layers of the sensors. The sensor has a gauge factor of -28 for low frequency deformation cycles.

Sensors with larger flexibility were also developed though inkjet printing technique. Various configurations and materials were used to evaluate which materials are most appropriate for these types of sensors. Sensors with a gauge factor of approximately 2.5 for an active layer of PeDOT were obtained. A sensor matrix of 4 x 5 sensors was fabricated with an active area of 1.8 x 1.5 mm^2 per sensor.

These sensors were subjected to a set of electromechanical tests to evaluate its performance in situations close to end use. So the prosthesis was coated with the various sensors, cemented and subjected to deformation cycles for three levels of force according to standard ISO7206.

An adaptive system read-out electronic circuit was developed and built that allows reading piezoresistive sensors with different characteristics. This system allows measuring a matrix of 8x8 sensors, but can be scaled to a large number of sensors. The readable range of the system is between 50 Ω and 100 kΩ according to the needs of the sensors being implanted.

The total area of the circuit is 135 mm^2, according to the requirements of a circuit to be used in in-vivo applications. An energy management system was also implemented that allows to activate and deactivate parts of the circuit when they are not needed, reducing the energy consumption. The system was validated by measuring a matrix of sensors with different characteristics.

Finally, simulations were performed in order to evaluate the best options for the development of a wireless communications system. Three possible operation frequency ranges were used for three types of standard antennas. The communication system was introduced into a model simulating the characteristics of the various layers that constitute the human body.

These simulations allow evaluate the frequency range most appropriate for implantable devices, the most appropriate antenna and the best location within the body. So the frequency chosen for the implementation was 868 Mhz for a Inverted-F antenna (IFA).

In conclusion, the key elements for the implementations of an instrumented hip prosthesis were development and validated. The developed and/or simulated elements, including sensors, circuits for reading and communication system can also be used in other applications due to characteristics.

Resumo

Nas últimas décadas, tem-se registado um aumento do número de sistemas de sensorização, aplicados aos mais diversos meios e grandezas. Esta é uma área em claro crescimento e ainda com elevado potencial.

Uma das áreas de desenvolvimento de sensores que tem recebido uma grande atenção é a área dos sensores para aplicações biomédicas e os biossensores, com claros benefícios para o ser humano.

Estes novos sensores necessitam, no entanto, de ultrapassar um grande número de desafios e restrições inerentes ao ambiente onde estes serão introduzidos, estas dificuldades levam à necessidade de utilizar novos materiais e novas técnicas para a sua construção junto com os mais tradicionais, e.g. baseados em silício, que tem já provado o seu interesse nesta área. Entre os diferentes materiais, os polímeros têm demonstrado ser uma boa escolha, devido ao conjunto de vantagens que apresentam, como o seu processamento simples, flexibilidade e facilidade de serem obtidos em diferentes formas, dai a sua escolha para fabricar sensores piezoresitivos implantáveis para o revestimento funcional de uma prótese de anca.

Estes sensores permitem revestir a prótese, dando assim novas funcionalidades aos implantes, tais como permitir medir força e deslocamentos entre a prótese e o osso e melhorar o diagnóstico pós-operatório.

Neste trabalho foi desenvolvido um modelo de prótese de anca com implementação de sensores. Para atingir esse objectivo, foram desenvolvidos sensores piezoresitivos flexíveis que permitam ser implantados. Assim foram fabricados sensores de deformação baseados em filmes finos de n^+-nc-si.H pela técnica de *hot-wire chemical vapor deposition* a uma temperatura de 150ºC sobre um substrato polimérico. Recorreu-se a técnica de litografia para construir as várias camadas do sensor. Os sensores apresentam um *gauge factor* de -28, para ciclos de baixa frequência em testes de *four-point-bending*.

Foram ainda desenvolvidos sensores com uma maior flexibilidade através da técnica de *inkjet printing*. Para esse desenvolvimento foram usadas várias configurações e materiais, para avaliar quais os materiais mais adequados para este tipo de sensores. Na caracterização destes sensores obteve-se um *gauge factor* de aproximadamente 2.5 para uma camada ativa de PeDOT. Com os melhores sensores obtidos foram construídas matrizes de 4 x 5 sensores que apresentam uma área ativa de 1.8 x 1.5mm^2 por sensor.

Estes sensores foram sujeitos a um conjunto de ensaios electromecânicos, para avaliar o seu desempenho em situações próximas da utilização final. Desta forma foi revestida uma prótese com os diferentes sensores, cimentada e sujeita a ciclos de deformação para três níveis de força, segundo a norma ISO7206.

Foi desenvolvido e construído um sistema de leitura adaptável que permite medir sensores piezoresistivos com diferentes características entre eles. Este sistema permite medir uma matriz de 8x8 sensores, mas pode ser escalada para um número maior de sensores. A gama de leitura do sistema varia entre 50 Ω e 100 kΩ, de acordo com as necessidades dos sensores a serem implementados.

A área total deste circuito é de 135 mm^2, de acordo com as necessidades de um circuito a ser utilizado em aplicações in-vivo. Foi também implementado um sistema de gestão de energia que permite ativar e desativar partes do circuito quando estas não são necessárias, permitindo, desta forma, reduzir os consumos de energia. O sistema foi validado através da medição de uma matriz de sensores com diferentes características.

Finalmente, foram realizadas simulações de forma a avaliar as melhores opções para o desenvolvimento do sistema de comunicação sem fios. Foram usadas três possíveis gamas de frequência de operação para três tipos de antenas *standard*. O sistema de comunicação foi introduzido num modelo simulando as características das várias camadas que constituem o corpo humano.

Estas simulações permitem aferir a gama de frequências mais adequadas para os dispositivos implantáveis, a antena mais adequada e a sua melhor localização, pois foi verificado como as várias camadas que constituem o corpo humano influenciam a comunicação. Assim, a frequência escolhida para a implementação foi de 868 MHz e a antena foi a IFA.

Em conclusão, os elementos principais para a implementação de uma prótese de anca instrumentada, foram desenvolvidos e validados. Os elementos desenvolvidos e/ou simulados, incluindo os sensores, circuitos de leitura e sistema de comunicação, poderão igualmente ser utilizados em outras aplicações devido às suas boas características.

Table of contents

List of figures

List of tables

List of symbols

Symbol	**Description**	**Unit**
e_{rad}	radiation efficiency	
f	Frequency	Hz
G	Amplification gain	
l	Length	m
m*	Carrier effective mass	kg
P_{rad}	Radiated power	w
P_{in}	Accepted power	w
q	Elementary charge	C
R	Electrical resistance	Ω
R_0	Initial electrical resistance	Ω
R_x	Sensor electrical resistance	Ω
t	Time	s
$\bar{t}$	Free time between carrier collisions	s
V	Electrical potential difference	V
v	Velocity	m/s
z	Vertical displacement	m
ε_l	Strain in length direction	
ε	Mechanical strain	
ε	Relative permittivity	
η	Radiation efficiency	%

Symbol	**Description**	**Unit**
λ	Wavelength	m
σ	Electrical conductivity	S/m
μ	Electron mobility	(m^2/(V.s))
υ	Poisson ratio	

List of abbreviations

4PBB – 4 point bending bridge

A

ADC - Analogic-digital converter

C

CIJ – Continuous inkjet printing

CNT - Carbon Nanotubes

CP – Conductive polymers

CPU – Central processing unit

CST MWS – CST Microwave Studio

D

DAC – Digital-to-analog converter

DMP – Dimatix printer

DOD – Drop on demand inkjet

E

EAP – Electroactive polymers

ERF – ElectroRheological fluid

F

FDTD – finite difference time domain

FIT – Finite Integration Technique

G

GF- Gauge factor

H

HF – High frequency

HWCVD - Hot-wire chemical vapor deposition

I

I/O – Input/output

IA – Instrumentation amplifier

IFA – Inverted-F antenna

IPG – Ionic polymer gels

IPMC – Ionic polymer metallic composite

L

LCE – Liquid crystal elastomers

M

MF – Medium frequency

MUX – Analog multiplexer

N

NB – Non balanced

O

OLEDs – Organic light emitting diodes

P

PBA – Perfect boundary approximation

PCB – Printed circuit board

PDMS - Polymethysiloxance

PI – Polyimide

PHR - Photoresist

PR – Piezoresistive

PUC- Power unit control

R

RIE – Reactive ion etching

RFID – Radio frequency identification

RF – Radio frequency

S

SG – Strain gauge

SPI – Serial peripheral interface

U

UC - Microcontroller

UHF – Ultrahigh frequency band

USB – Universal serial bus

1. Introduction

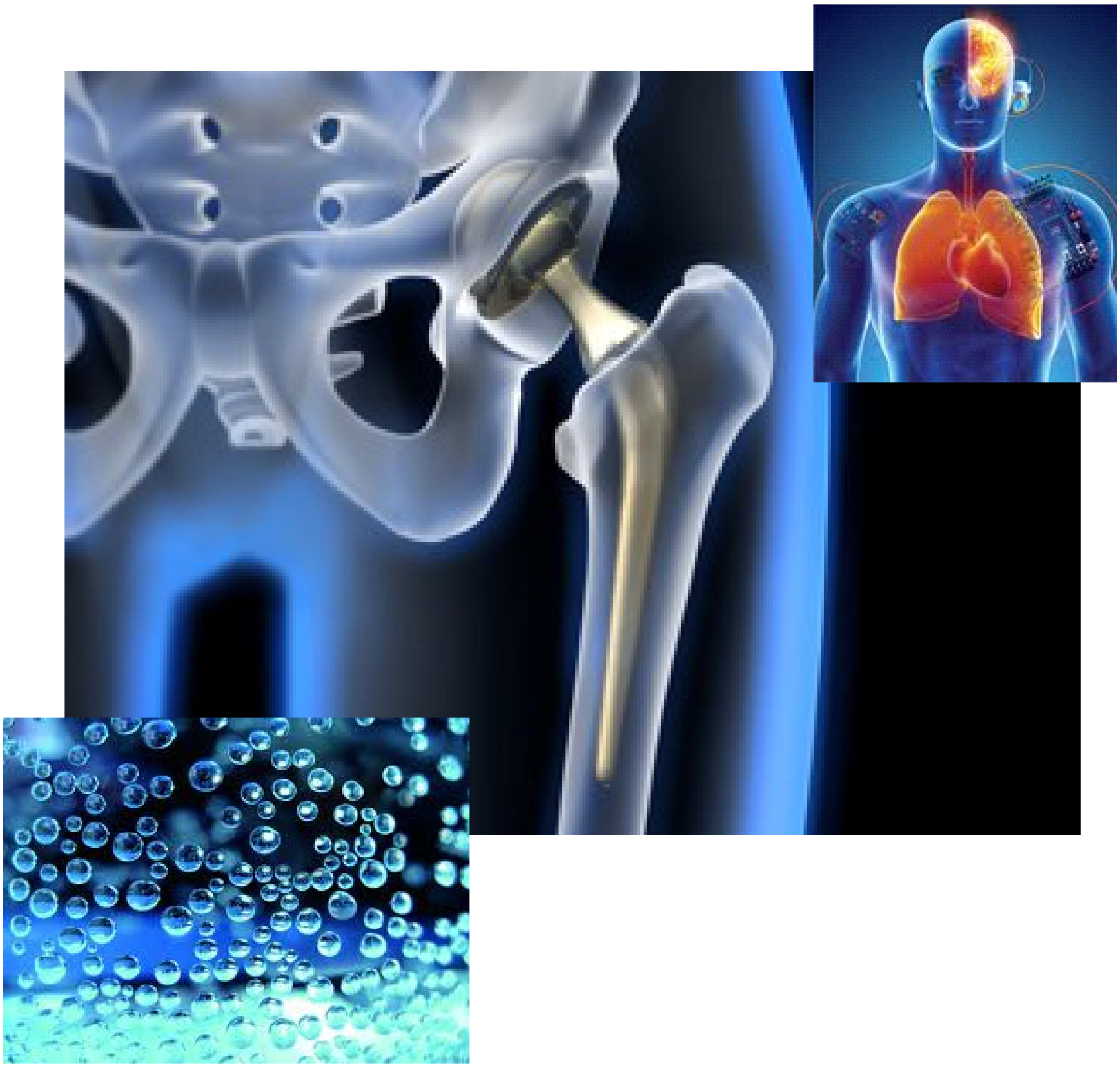

In this chapter is presented a general introduction on the main topics related to the developed investigation. A detailed introduction and the state of the art of the different items developed in the present investigation are presented at the beginning of each chapter, due to their different nature and specificity.

The introduction begins with the current developments in implantable sensors and, in particular, in sensors that can be applied for the development of sensing hip prosthesis. Special attention is paid to polymer-based sensor for the measurement of forces and deformations and, in particular, to piezoresistive sensors. In this group, metallic sensor and silicon crystal semiconductor sensors are introduced as well as polymer-based sensors.

After the description of the various techniques used in the production of polymer-based sensors, an approach to the state of the art of the reading and communication systems for implantable biosensors will be presented.

This chapter concludes with the identification of the development goals and the description of the thesis structure and methodology.

1.1. Implantable sensors

Due to technological advancements, there is an increasing demand of sensors as their implementation areas are broadening. Therefore, strong efforts are devoted to the development of new types of sensors capable to satisfy the most different needs [1–5].

One of the most active areas of research in this field is the development of implantable sensor, which can bring strong benefits in heath condition monitoring [6], [7]. On the other hand, the development of implantable sensors is also marked by the difficulties and restrictions in this research area, such as biocompatibility, dimension, autonomy, robustness, implantation facility and medical certification.

Implantable sensors have been used to provide comprehensive understanding of the musculoskeletal, biological and neuronal human system [5], [7], [8]. These complex sensor systems have improved our understanding of the in vivo environment allowing obtaining in vivo measurements of pressures, temperatures, torque, forces, chemical and electrical signals in situations such as after surgical procedures [9–11], in prolonged illness requiring continuous monitoring [9] and around implants during post-operative healing [9].

Sensors have been evolved to sensor systems in many cases incorporating also the conditioning and the communication system [9], [12], [13]. Recently, the evolution in micro- and nano-fabrication technology allows to integrate most efficiently these systems, leading to the development of novel biomedical sensors that can be incorporated into implants or tissue with minimal or no modification to the implant [14]. This technology has also allowed transforming the traditional implants into smart implants.

This new type of implants offers important advantages as it allows having direct access to real time data for diagnosis and treatment.

Being this type of sensors and implants very recent, there are no commercial systems of this type, the few existing systems being still under development such as monitoring of blood glucose level for diabetes [5], [15], [16], continuous in vitro measurement and monitoring of lactate in the bloodstream or tissues [17], minimally pressure monitoring of blood vessels and intracranial compartments [18], electronic interface to the nervous system [19] and stress/ strain measurement systems to apply in hip, knee, long bone and spinal implants [20–22].

The most common use of implantable prosthesis is a hip prosthesis. Two main techniques for hip prosthesis fixation are used: cemented technique which consist to put a layer of polymethylmethacyrlate between the bone and the prosthesis and cementless technique, which requires a longer recovery time [11].

Due to the complexity of this type of intervention the measurement of the forces and the fixation state has a considerable interest for several reasons, including:

- the understanding of the relationship between the mechanics of the hip and the degenerative joint disease;
- to improve failure detection, since the detachment of the prosthesis is a common failure mechanism.

To detect failure some techniques have been established in clinical routine in order to determine the degree of prosthesis fixation in the bone as for example radiography, bone scintigraphy or arthrography [23–25]. But this diagnostic techniques present high uncertainties which can lead to diagnostic errors [26], [27] that can lead to the bone destruction.

The measurement of the relative motion between the prosthesis and the surrounding bone provides important information on the state of attachment of the prosthesis such as the prosthesis durability and the bone construct.

New approaches are therefore under development to perform these types of measures. However there are several technical difficulties to be overcome in measuring the relative motion, because the magnitude of these movements that can vary between a few micrometers to one millimeter [28], as determined based on estimations from biomechanical assays [11], performed on models that have a good correlation with the results obtained in vivo [29], [30].

These laboratorial test are limited by the used model which cannot be extensively used for all situations at which the prosthesis is subjected is a real operation scenario. In this way, new improvement for developing measurement systems for prosthesis are focused on the creation of instrumented prosthesis for in vivo application [10], [12], [14], [31].

1.2. Polymeric materials for strain and pressure sensors

The ease of processing and low cost has lead to the widespread use of polymer in materials in our everyday life. In the electrical industry these materials were initially used as electrical insulating due to its lightweight and good characteristics as electrical insulator [32].

With the incorporation of suitable fillers such as carbon black, graphite powder, carbon fibers or metal nanoparticles within the polymer matrix, the composites show large electrical conductivity, in the order of 10^6 S/m [33] after the percolation threshold [33], [34]. These material are called extrinsic conductors [33] as there are the charges incorporated into polymer material which ensure the electrical conduction [33].

Due to these developments, the application potential of polymers has grown considerably, including the fabrications of electrodes for rechargeable batteries [33], [35], [36], electrical shielding [37], capacitors [38], electroluminescent devices [39], and new types of sensors for the many different applications, such as strain and force sensors [4], [40], [41], chemical sensors [42], [43], biological sensor and position sensors.

Nowadays, there is an increasing trend to develop smart sensors based on polymer materials due to their processing versatility [44–46]. In this way, polymer based strain and pressure sensors are used in the form of films [47], fibers [48], nanowires [49] and multi-layer [50], among others.

The main types of polymer-composites used for mechanical sensing are generally classified as electrically active (electrical response) and optically active (photonic response) materials [51].

The optically active sensors are based on the monitoring of the wavelength shift of the returned Bragg-signal as a function of the strain force [52]. Being these materials optically active, the wavelength of the signal that crosses the material varies as a function of its geometry, hence its application as strain and pressure sensors [41], [52].

The fact that certain types of polymers can change shape in response to electrical stimulation and vive-versa has been known for decades, being the first registration of this phenomenon dated of 1880 by Roentgen using a rubber-band with fixed end and a mass attached to the free-end, which was charged and discharged [53]. These polymers fall into the category of electroactive polymers (EAP)

The larger progress in the field of EAP took place mainly in the last decade where efficiency of these materials in the electromechanical conversion increased more than 300% [54].

EAP can be divided into two major categories based on their activation mechanism, ionic and electronic (table 1.1). In the electronic EAP type the activation forces are generated by a dielectric response driven by the electric field, whereas in the ionic EAP type the forces are generated by diffusion of mobile ions [55]. As the activation methods are different, they have the different time responses and activation voltages [56].

Table 1.1 - List of the principal EAP materials classification [55].

Electronic EAP	**Ionic EAP**
• Dielectric EAP • **Electrostrictive Graft Elastomers** • Electrostritive Paper • Electro-Viscoelastic Elastomers • Ferroelectric Polymers • Liquid Crystal Elastomers (LCE) • **Piezoelectric Polymers**	• **Carbon Nanotubes (CNT)** • **Conductive polymers (CP)** • ElectroRheological Fluid (ERF) • Ionic Polymer Gels (IPG) • **Ionic Polymer Metallic Composite (IPMC)**

There are two major groups of polymer based sensors to measure forces and displacements, the piezoresistive sensors that are typically used to measure forces and quasi static and low frequency displacements and piezoelectric sensors that are typically applied in dynamical systems. Piezoelectric sensors are based on piezoelectric materials which are characterized by converting mechanical energy into to electrical energy and vice versa [57]. When a mechanical force is applied to a piezoelectric material this will produce an electrical response. The reverse phenomenon also occurs: when an electrical voltage is applied to the piezoelectric material, this material presents a mechanical deformation. In this way, piezoelectric materials can be used as sensors and actuators in applications such as dynamic force sensors [4], [58], micro position system [59], communication transducers [60], among others.

Due to the nature of the system which will be implemented the focus will be mainly on piezoresistive sensors.

1.3. Piezoresistive sensors

An interesting effect commonly used for the development of deformation sensors is the change of electrical resistance due to an applied load, which was first discovered by Lord Kelvin in 1856 in metals, being the large piezoresistive effect first discovered in 1954 with the use of single crystals silicon and germanium. As in the case of metals, also the semiconductors change their resistivity as a function of strain.

The sensitivity of a piezoresistive sensor (equation 1.1) can be represented by the gauge factor (*GF)*, which represents the relative change in electrical resistance due to mechanical deformation:

$$GF = \frac{dR/R}{dl/l}$$

. (eq. 1.1)

In this equation, *R* is the steady-state material electrical resistance before deformation and d*R* is the resistance change caused by the variation in length d*l* [61]. The resistance change under strain results from the contribution of the dimensional change a geometrical effect (ΔR_D) and from the intrinsic piezoresistive effect (ΔR_l) . For the surface mode measured in the present investigation the *GF* can be written as [61]:

$$GF = \frac{dR/R}{\varepsilon_l} = \Delta R_D + \Delta R_l$$

$$= 1 + \upsilon + \frac{\frac{d\rho}{\rho}}{\varepsilon_l}$$

(eq. 1.2)

where, $dl/l = \varepsilon_l$ and υ is the Poisson ratio.

The typical gauge factor values of the main materials used for strain sensors described in the literature are presented in table 1.2.

Table 1.2 - Typical gauge factor values of the main materials used for strain sensors.

Sensor Material	Gauge Factor	Reference
Metal foil strain gauge	2-5	[62]
Thin-film metal	2	[62]
Crystalline silicon	± 50 -150	[63]
Thin film crystalline silicon	± 15	[64]
Polymer	18	[65]

1.3.1. Metallic

The metallic strain sensors uses the dependence of the electrical conductance of the material on the conductor's geometry. That is, when a conductor is straightened to the limit of its elasticity, it will diminish its cross-section which leads to a increase of the resistance of the conductor. When the conductor is subjected to a compression, the opposite phenomenon is observed.

When the conductor is attached to the medium to be measured, the change in the conductor resistance is proportional to the deformation of the medium. Thus to increase the resistance variation of the material, a pattern in Zig-Zag format (figure 1.1) is fabricated to increase sensitivity for stress in the parallel direction of the conductive lines.

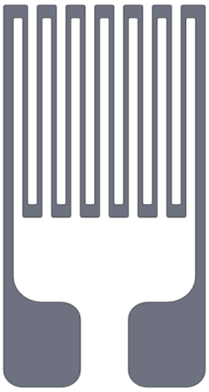

Figure 1.1 - Zig-Zag pattern format for a metallic sensor.

The most used type of metallic sensor is the strain gauge due to its simplicity of construction and operation in spite of presenting a low GF value (table 1.2). It shows also good linearity in the electro-mechanical response.

1.3.2. Crystal silicon semiconductor

In the case of semiconductors its resistivity depends on the mobility and amount of charge carriers, at a given temperature. Equation 1.3 represents the formula for the mobility [66].

$$\mu = \frac{q\bar{t}}{m^*}$$

(eq. 1.3)

here, q is the change, $\bar{t}$ is the free time between carrier collision events and m^* the effective mass of carrier in the crystal lattice. The effective mass and free time are related to the average atomic spacing in a semiconductor lattice, which is subject to change under applied physical strain and deformation. The piezoresistive effect can be explained in more detail using the quantum-physics which is present in reference [66] .

Currently there are many materials used to build stress and deformation piezoresistive sensors, however, most of them based on silicon due to its high sensitivity. Examples are accelerometers [67], pressure sensors [43], [68], gyro rotation rate sensors [69], [70], tactile sensors [71], [72] and flow sensors [42], among others.

Although the sensors based on silicon are excellent for particular applications, they can mainly be applied in semi-rigid and low deformation sensors [73].

Thus arises the possibility to deposit silicon thin films on polymer substrates. This method allows increased flexibility in comparison to the previously described sensor at the cost of a decrease in performance (table 1.2).

Some of the most interesting films with this characteristics have been prepared by Hot-wire chemical vapor deposition (HWCVD). This is a technique that based on the decomposition of precursor gases on a heated filament (normally tungsten), with the constituent radical species often reacting in the gas phase that is depositing onto substrate, with HWCVD there are a large number of reactor variables that can influence the quality of the film obtained. These variables include, among others, wire temperature, total pressure, gas flow rate, and substrate temperature.

This technique has proved to be a very adequate technique to deposit hydrogenated Nano crystalline silicon thin films, nc-Si:H, due to its high efficiency in breaking H_2 molecules into atomic hydrogen that diffuses from the heated tungsten filament to the growing film surface [74].

1.3.3. Polymer-based sensors

It is increasingly intended to introduce sensors in the most varied surfaces. For this reason there is a growing interest in the development of a third group of piezoresistive sensors, based on polymers, which allow the construction of large deformation, large area, flexible sensors [65], [75], [76], allowing its molding into specific shapes and associated to facility of production and low costs.

The model of operation of this type of sensors is very similar to the previous ones and is shows gage factor with large contributions of the intrinsic piezoelectric effect [77]. When a polymer film is deformed, the conduction paths are modified (figure 1.2), influencing electron transfer rates between near molecules [78], [79], leading therefore to a deformation dependence electrical resistance.

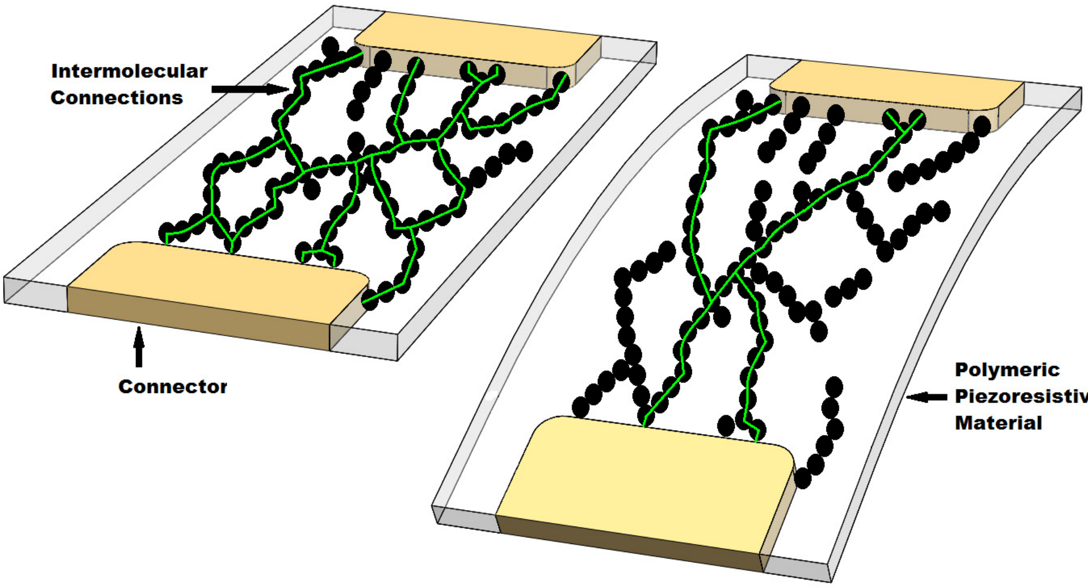

Figure 1.2 - Piezoresistive intrinsic effect, intermolecular connections variation by a mechanical deformation.

1.4. Polymeric sensors productions technics

Currently there are several processing techniques used for the development of polymer based strain and force sensors. Some of them are conventional techniques used in industry, such as:

Extrusion, where the raw polymeric material is heated and forced out through a die in the form of the profile to produce along its extension, after cooling. Varying the form of the die it is possible to obtain different products in the form of films, plates, hoses, tubes and other profiles [80].

Injection processing is similar to the previous one in the mode of operation but in this case the material is forced to enter in the injection channels of the mold and in the mold cavities using high pressure, which reproduce the form of the product to be manufactured. With this technique is possible to obtain the most diverse forms of pieces according to the mold [80].

Apart from these conventional techniques, other techniques are used for micro and nano-fabrication, to introduce functional layers, or to incorporate layers that permit acquiring the sensor response such as:

Bar-coating is a widely used method to develop coatings due to its simplicity. This method is based on a rod on which a filament is coiled. This filament may present different diameters according to the thickness of the coating to be obtained. Thus by passing the rod above the film, the excess of material is removed leaving a layer with the desired thickness [81] as shown in figure 1.3.

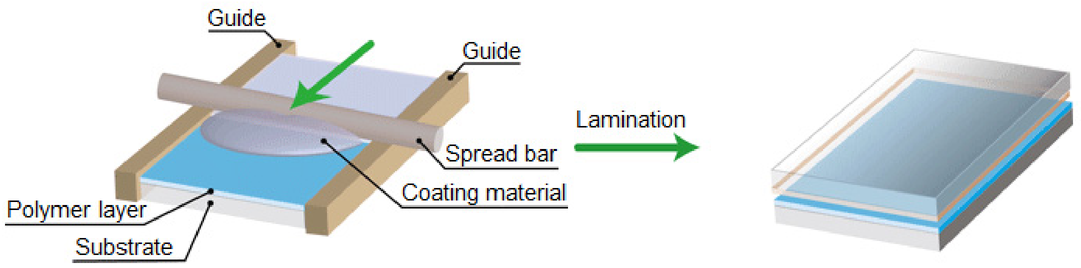

Figure 1.3 - Production of polymer films using a bar-coating method.

Spin-coating is a procedure used to apply uniform thin films to flat substrates. It can be also applied on flexible substrates. An excess of a solution is placed on the substrate, which is then rotated at high speed in order to spread fluid by centrifugal force (figure 1.4).

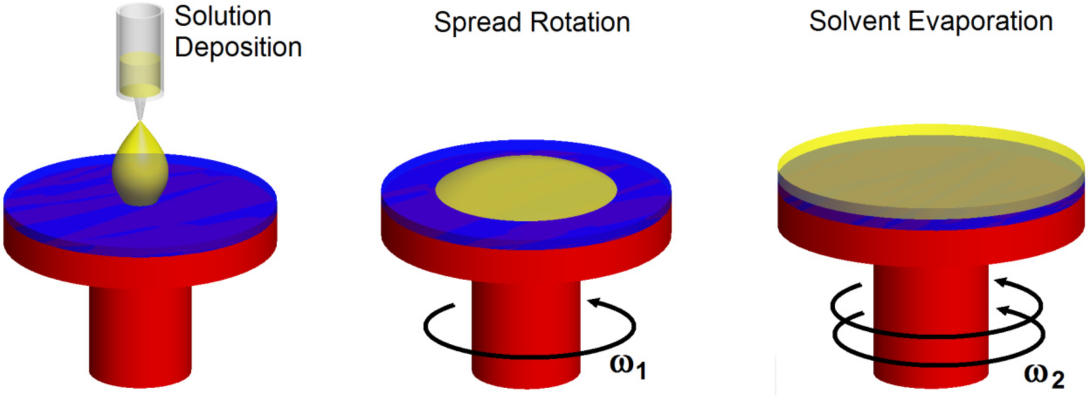

Figure 1.4 - Production of polymer films using a spin-coating method

The layer thickness is defined by a set of parameters such as the rotation speed, the solution concentration and the type of solvent [81].

Inkjet printing has gained special attention during the last decade as it is a fast and versatile method [82–84] with high reproducibility and applicable in large areas. Its use in the fabrication of sensors is still very limited with just a few recent developments [85], [86]. In the area of inkjet printing microelectronic devices this method also begins to be used in the production of organic light emitting diodes (OLEDs) [39], thin-film transistors [87], RC filter circuit [88], radio frequency identification (RFID) tags [83] and solar cells [89], among other applications.

The inkjet technologies can fundamentally be described as a digitally controlled ejection of drops of a fluid from a printhead onto a substrate. This can be accomplished in many ways.

The inkjet printing systems are broadly classified as deflection continuous inkjet (CIJ) or drop on demand inkjet (DOD) [90], as shown in figure 1.5.

In continuous inkjet printing (CIJ) [90] a pump directs fluid from a reservoir to one or more small nozzles, which eject a continuous stream of drops at high frequency using a vibrating piezoelectric crystal. A flow of drops is thus created which are electrically charged as they pass in a charge electrodes.

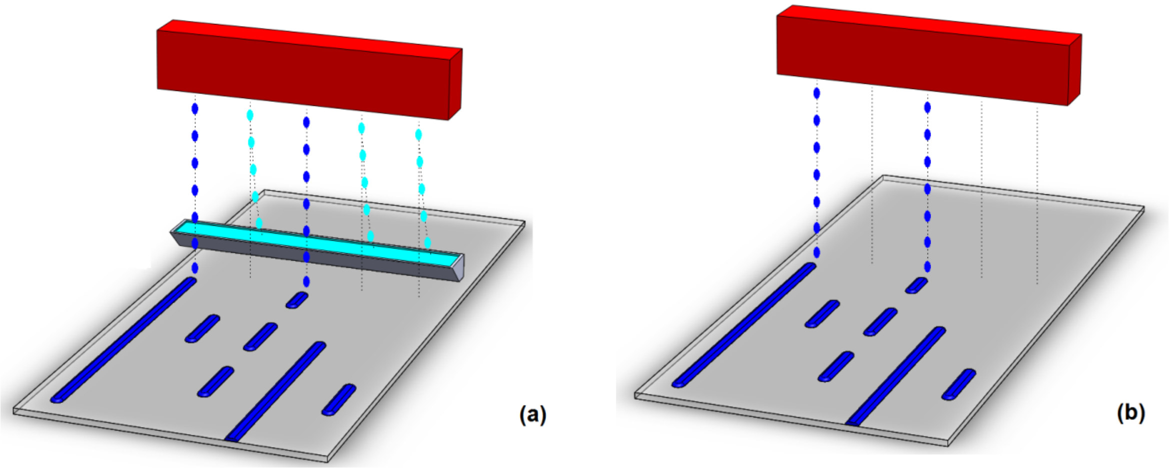

Figure 1.5 - Inkjet printing main classification: a) multi deflection continuous inkjet and b) drop on demand inkjet.

These drops pass through a series of deflection plates which uses an high voltage electrostatic field to select drops that are to be printed or collected for recycling, as shown in figure 1.5a) and figure 1.6.

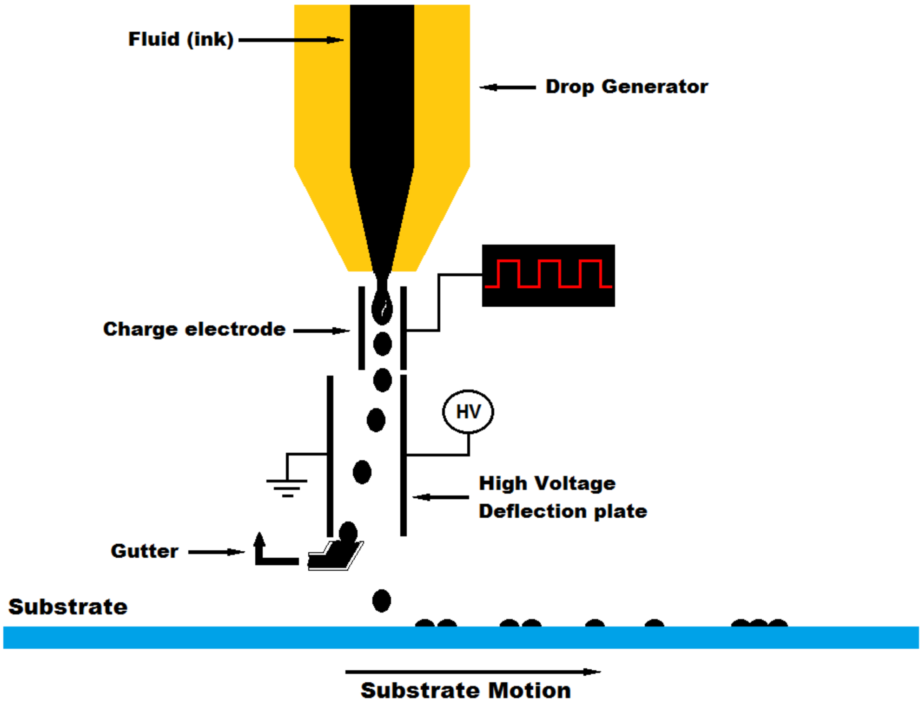

Figure 1.6 - Schematic representation of the continuous inkjet printing (CIJ) technology operation mode.

This system allows a very high speed inkjet printing, but with low resolution.

In the DOD method [90], drops are ejected from the printhead only when required, as shown in figure 1.5b). In general, the drops are formed by the creation of a pressure pulse within the printhead, There are two main subcategories of DOD inkjet printing systems, thermal and piezoelectric, existing also electrostatic and acustic, which are documented but of little use.

In thermal inkjet technology [90], the drops are formed by a fast heating with a resistive element within a small chamber containing the ink. The temperature rises to 350-400ºC, which causes an ink vaporization that is in contact with the heating element causing a pressure pulse which forces the drop out, as represented in figure 1.7.

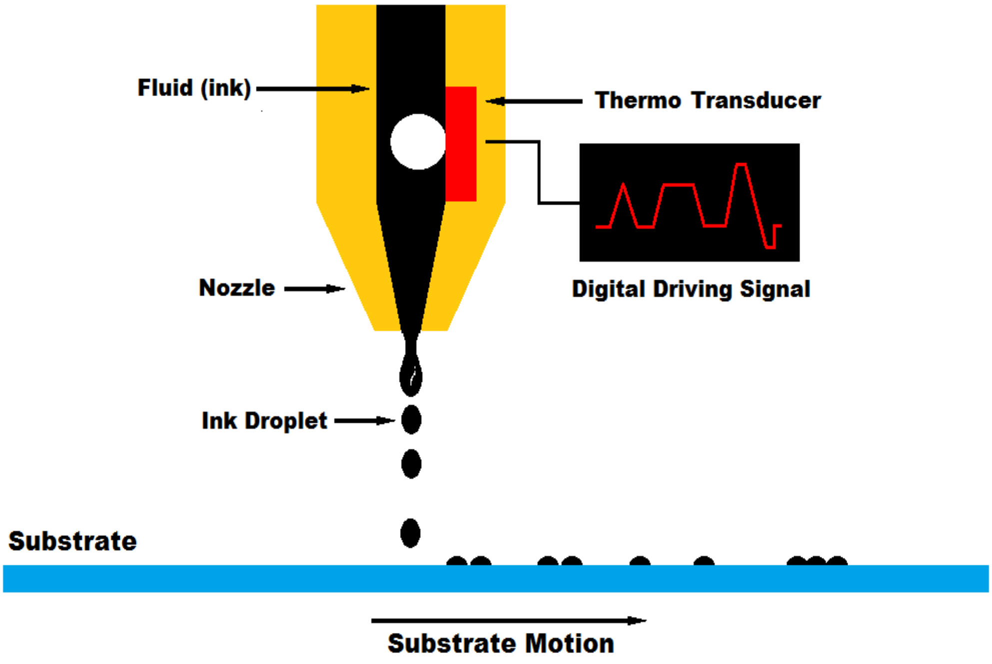

Figure 1.7 - Schematic representation of the thermal inkjet technology operation mode.

The injection of the drop leaves a void in the chamber which is filled by the ink that is present in the cartridge.

The principal vantage of this technology is the fact of allowing very small drop sizes and high nozzle density that allows printouts with high resolution.

The main disadvantage of this technology is the limitation of the materials that constitute the ink, as the ink has to support high temperatures and must be able to vaporize with increasing temperature and exit trough the nozzle.

The piezoelectric drop on demand inkjet technology [90] is increasingly used in industrial and research environments. In this technology a piezoelectric crystal (usually lead zirconium titanate) changes its dimensions when subjected to an electrical field. This variation causes a pressure increase in the chamber with the ink, which originates a drop to be ejected from the nozzle, as it is shown in figure 1.8.

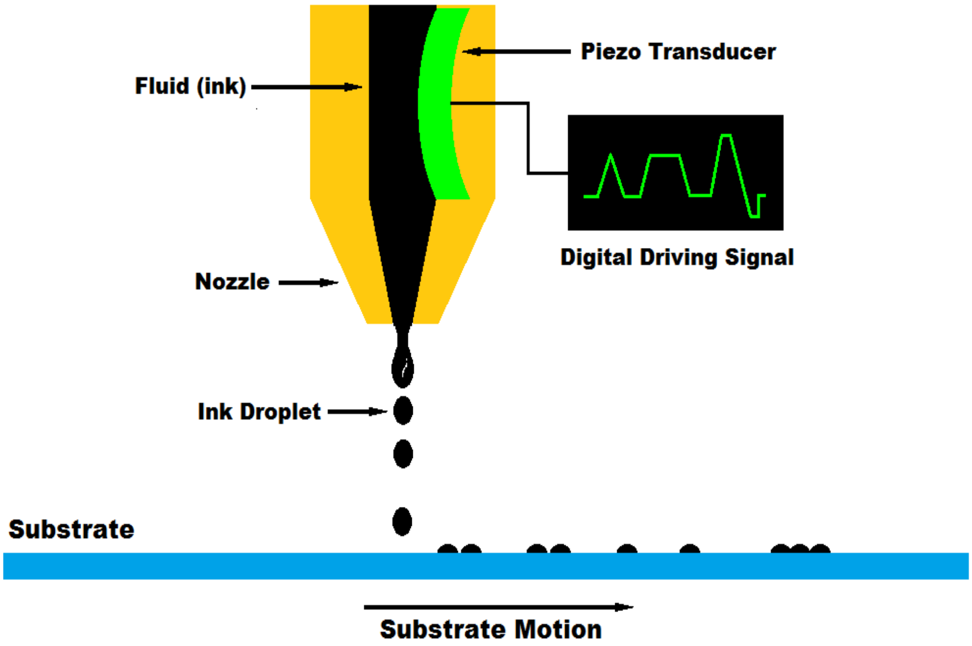

Figure 1.8 - Schematic representation of the piezoelectric drop on demand inkjet technology operation mode.

The main advantage of this technology is the possibility to operate with any type of fluid and the facility in controlling the quantity of injected fluid by the amplitude of electric field.

1.5. Electronic interface and communications systems for biosensors

Technological advances led to the development of many types of sensors used to measure the most diverse quantities, applied in many different ways and formats which are being increasingly associated in array and matrix [91].

Associate with the sensor development there is also the need to develop systems of signal conditioning capable to responding to the needs of new sensors as well as meet the demand for systems with higher capacity for integration between the sensor and signal condition circuit [3], [92] and to reduce the final dimensions of the system. All of this is motivated by the need to integrate sensors in the own devices to be measured, i.e. to allow the device itself to act as a sensor and not to have two distinct sub-systems were one limits the other [93].

In the biosensors area, mainly in the implantable sensor area this need is more evident due the higher restrictions of this type of applications with respect to dimensions, autonomy, precision, biocompatibility and hardness [7].

Further, when the aim is to read a number of sensors, these restrictions are more evident [94].

To increase of the level of miniaturization of the circuits various techniques have been used, such as multiplexed systems [3], [93], [95], [96], which allows reading a wide range of sensors with a single reading circuit. Another method is the construction of all the architecture on-chip, where the multiplexing circuit, the amplifier circuit and microcontroller are integrated in a single device [3], [93], [95], [96].

In the presence of multi sensor architectures, commonly several sensors are not equal, raising the need to develop an adaptive circuit [3], [95], i.e. a circuit capable to adapt to the type of sensor to be measured and to adjust the circuit parameters to obtain the maximum resolution.

To develop this kind of circuits, it is necessary to build a fully digital circuit system as the ones in [3], [95], i.e. a circuit that allows to change its characteristics digitally by firmware, as only in this case it is possible to change the parameters of the circuit by a microcontroller. This type of circuit has also the advantage of allowing the calibration of the sensors after the integration in the system.

In many cases, such as in-body applications, it is also necessary to implement a wireless communication system to a remote platform.

For example, the use of wireless communication systems for implants allows monitoring in real time the state of the implant and how the body reacts to the implant [97].

Many electronic implants have been already developed such as brain pacemakers for treatment of Parckinson’s disease [98], muscle stimulators [99], implantable drug pumps [100] and blood glucose sensing [5].

Although there are many types of implants, there are very few with implemented data communication. With the recent developments of radio frequency (RF) communication systems, motivated by the developments of mobile phones, it has allowed the emergence of research related to communication systems from the inside to outside of human body [101], [102].

This set of studies are based on simulation models, based on Finite Integration Technique (FIT) and finite-difference time-domain (FDTD) [103] .

These simulation methods allow perform simulations in a wide range of frequencies, thus the published studies also focus on frequencies between 150 Mhz and more than 2400 Mhz [104–106].

Various types end formats of antennas have been also analyzed, including elliptic, circular and IFA antennas [106], [107], since the response characteristics of the implantable communication systems depend heavily on their location and the depth at which they placed due to the electrical characteristics (permittivity and conductivity) of the layers that are between the device and outside of the body.

1.6. Objectives

The main objective of this thesis is to develop flexible piezoresistive sensors for coating implantable prosthesis and develop the electronic interface and signal transmission for the developed sensors.

The main focus areas of the present work are:

- Development and characterization of silicon piezoresistive sensors in single sensor and sensor array format.
- The fabrication and characterization of piezoresistive sensors by inkjet printing technology.
- Design and fabricate and adaptive electronic circuit interface for multi piezoresistive sensors.
- Study and development of implantable communication system, for sensor data communications.
- Study and characterization of the system when subjected to real use conditions.

1.7. Structure and methodology

The present thesis is divided in seven chapters with the objective to provide a comprehensive description of the progress reached during this investigation. The chapters are presented in such a way that show the sequential progress obtained in a variety of works.

Five of those chapters are based on published or submitted scientific articles. The development of flexible force and deformation sensors and the respective reading and communication system for implants has been achieved and the development is described as follows:

Chapter 1 shows the main objectives, structure and methodology of this work as well as a brief introduction on the main topics of the thesis.

Chapter 2 consists on the development of a piezoresistive silicon thin film array by HWCVD technic on a flexible polymeric substrate. The sensors were characterized using a four point bending technic and the gauge factor of the sensors determined.

The sensors were used to coat a hip prosthesis, in order to evaluate its performance in a real application. Chapter 3 describes the performed tests on the model, which were conducted according to standards. It is still made a comparison of the obtained results with computer simulations.

Chapter 4 shows the development of inkjet printed sensors as well as their main characteristics.

The sensors were also incorporated into a hip prosthesis and their performance evaluated after the corresponding standard.

Due to the need to measure a large number of sensors that can present different characteristics, it has been studied and developed an adaptive read out circuit. Its development is described in chapter 5. This chapter also focuses on the remaining electronic circuit and its characteristics and shows a proof of concept of operation and operation mode.

After the development of the sensor matrix, a study based on simulations was performed in order to evaluate the best choice regarding to the communication frequency, antenna type and the most favorable position of the communication system. This study is described throughout the chapter 6.

Finally, chapter 7 presents the overall conclusions and suggestions for the future work.

1.8. References

[1] S. Ni and C. Zhang, “Attitude Determination of Nano Satellite Based on Gyroscope, Sun Sensor and Magnetometer,” *Procedia Engineering*, vol. 15, no. 0, pp. 959–963, 2011.

[2] W. Qingmin, Y. Yaoen, S. Mubiao, and L. Yuhong, “Research on Application of Micro-Nano Acceleration Sensor in Monitoring the Vibration State of Vehicles,” *Procedia Engineering*, vol. 29, no. 0, pp. 1213–1217, 2012.

[3] C.-Y. Wu and K.-T. Tang, “A polymer-based gas sensor array and its adaptive interface circuit,” *VLSI Design Automation and Test (VLSI-DAT), 2010 International Symposium on*. pp. 355–358, 2010.

[4] G. M. Krishna and K. Rajanna, “Tactile sensor based on piezoelectric resonance,” *Sensors Journal, IEEE*, vol. 4, no. 5. pp. 691–697, 2004.

[5] E. Renard, “Implantable glucose sensors for diabetes monitoring,” *Minimally Invasive Therapy & Allied Technologies*, vol. 13, no. 2, pp. 78–86, 2004.

[6] C.-P. Lau, D. C. W. Siu, and H.-F. Tse, “Optimizing heart failure therapy with implantable sensors,” *Journal of Arrhythmia*, vol. 28, no. 1, pp. 4–18, Feb. 2012.

[7] R. D. Black, “Recent Advances in Translational Work on Implantable Sensors,” *Sensors Journal, IEEE*, vol. 11, no. 12. pp. 3171–3182, 2011.

[8] B. Johnson, S. T. Peace, T. A. Cleland, and A. Molnar, “A scalable CMOS sensor array for neuronal recording and imaging,” *Sensors, 2011 IEEE*. pp. 924–927, 2011.

[9] M. Frischholz, L. Sarmento, M. Wenzel, K. Aquilina, R. Edwards, and H. B. Coakham, “Telemetric Implantable Pressure Sensor for Short- and Long-Term Monitoring of Intracranial Pressure,” *Engineering in Medicine and Biology Society, 2007. EMBS 2007. 29th Annual International Conference of the IEEE*. p. 514, 2007.

[10] J. S. P. et al. S.J. Taylor, P.S. Walker, “The forces in the distal femur and the knee during walking and other activities measured by telemetry,” *J Arthroplasty*, vol. 13, p. 428, 1998.

[11] J. R. Britton, C. G. Lyons, and P. J. Prendergast, “Measurement of the Relative Motion Between an Implant and Bone under Cyclic Loading,” *Strain*, vol. 40, no. 4, pp. 193–202, 2004.

[12] B. A. Kotzar GM, Davy DT, Goldberg VM, Heiple KG, Berilla J, Heiple KG Jr, Brown RH, “Telemeterized in vivo hip joint force data: a report on two patients after total hip surgery,” *J Orthop Res*, vol. 9, pp. 621–33, 1991.

[13] C. R. and S. L.-M. Vítor Correia, José G. Rocha, “Ultra-High Band Radiowave Propagation Analysis for implanted Biosensors Communication System,” *Journal IEEE Transactions on Biomedical Engineering*, vol. Submitted, 2013.

[14] D. D. D’Lima, S. Patil, N. Steklov, S. Chien, and C. W. Colwell Jr., “In vivo knee moments and shear after total knee arthroplasty,” *Journal of Biomechanics*, vol. 40, Supple, no. 0, pp. S11–S17, 2007.

[15] S. A. Jaffari and A. P. F. Turner, “No Title Recent advances in amperometric glucose biosensors for in vivo monitoring,” *Physiological Measurement*, vol. 16, pp. 1–15, 1995.

[16] A. B. Islam, S. K. Islam, and T. Rahman, “A vertically aligned carbon nanofiber (VACNF) based amperometric glucose sensor,” *Semiconductor Device Research Symposium, 2009. ISDRS ’09. International*. pp. 1–2, 2009.

[17] D. A. Baker and D. A. Gough, “A Continuous, Implantable Lactate Sensor,” *Analytical Chemistry*, vol. 67, no. 9, pp. 1536–1540, 1995.

[18] C. Hierold, B. Clasbrummel, D. Behrend, T. Scheiter, M. Steger, K. Oppermann, H. Kapels, E. Landgraf, D. Wenzel, and D. Etzrodt, “Low power integrated pressure sensor system for medical applications,” *Sensors and Actuators A: Physical*, vol. 73, no. 1–2, pp. 58–67, Mar. 1999.

[19] K. D. Wise, D. J. Anderson, J. F. Hetke, D. R. Kipke, and K. Najafi, “Wireless implantable microsystems: high-density electronic interfaces to the nervous system,” *Proceedings of the IEEE*, vol. 92, no. 1. pp. 76–97, 2004.

[20] E. L. Tan, B. D. Pereles, B. Horton, R. Shao, M. Zourob, and K. G. Ong, “Implantable Biosensors for Real-time Strain and Pressure Monitoring,” *Sensors*, vol. 8, no. 10, pp. 6396–6406, 2008.

[21] D. L. Glos, F. E. Sauser, I. Papautsky, and D. I. Bylski-Austrow, “Implantable MEMS compressive stress sensors: Design, fabrication and calibration with application to the disc annulus,” *Journal of biomechanics*, vol. 43, no. 11. Elsevier Science, pp. 2244–2248, 10-Aug-2010.

[22] M. K. Moore, S. Fulop, M. Tabib-Azar, and D. J. Hart, “Piezoresistive pressure sensors in the measurement of intervertebral disc hydrostatic pressure,” *The spine journal : official journal of the North American Spine Society*, vol. 9, no. 12. Elsevier Science Inc.,, pp. 1030–1034, 01-Dec-2009.

[23] D. O’Neill and W. Harris, “Failed total hip replacement: assessment by plain radiographs, arthograms, and aspiration of the hip joint,” *The Journal of Bone and Joint Surgery*, vol. 66, pp. 540–546, 1984.

[24] G. Qi, W. P. Mouchon, and T. E. Tan, “How much can a vibration aldiagnostic tool reveal in total hip arthroplasty loos-ening?,” *Clinical Biomechanics*, vol. 18, pp. 44–458, 2003.

[25] O. Temmerman, P. Raijmakers, J. Berkhof, E. David, R. Pi-jpers, Marinus, Molenaar, O. Hoekstra, G. Teule, and I. Heyligers, “Diagnostic accuracy and interobserver variability of plain radiography, subtraction arthrography, nuclear arthrog-raphy, and bone scintigraphy in the assessment of aseptic femoral component loosening.,” *Archives of the Orthopaedic and Trauma Surgery*, vol. 126, pp. 316–323, 2006.

[26] P. H. and B. øballe, K., Hansen, E. S., Brockstedt-Rasmussen, H., Jorgensen, “Tissue ingrowth into titanium and hydroxyapatite-coated implants during stable and unstable mechanical conditions,” *J. Orthop*, vol. 10, pp. 285–299, 1992.

[27] J. D. and H. W. H. Engh, C. A., O’Connor, D., Jasty, M., McGovern, T. F., Bobyn, “Quantification of implant micromotion, stress shielding, and bone resorption with porous-coated anatomic medullary locking femoral prostheses,” *Clin. Orthop*, vol. 285, pp. 13–29, 1992.

[28] P. and M. Kärrholm, J., Nivbrant, B., Thanner, J., Anderberg, C., Borlin, N., Herberts, “Radiostereometric evaluation of hip implant design and surface finish,” Orlando, 2000.

[29] F. Kärrholm, J., Borssen, B., Lowenhielm, G. and Snorrason, “Does early micromotion of femoral stem prostheses matter,” *J. Bone Joint Surg*, vol. B76, pp. 912–917, 1994.

[30] D. W. Alfaro-Adrian, J., Gill, H. S. and Murray, “Cement migration after THR: a comparison of Charnley Elite and Exeter femoral stems using RSA,” *J. Bone Joint Surg*, vol. B81, pp. 130–134, 1999.

[31] J. J. O. et al. T.W. Lu, S.J. Taylor, “Influence of muscle activity on the forces in the femur: an in vivo study,” *J Biomech*, vol. 30, p. 1101, 1997.

[32] J. F. Hall, “History and bibliography of polymeric insulators for outdoor applications,” *Power Delivery, IEEE Transactions on*, vol. 8, no. 1. pp. 376–385, 1993.

[33] D. B. Anthony R. Blythe, *Electrical properties of polymers.*, II., vol. 33, no. 9. Cambridge University Press, 2005, p. 480.

[34] J. Li and J.-K. Kim, “Percolation threshold of conducting polymer composites containing 3D randomly distributed graphite nanoplatelets,” *Composites Science and Technology*, vol. 67, no. 10, pp. 2114–2120, Aug. 2007.

[35] M. L. Soria, J. Fullea, F. Sáez, and F. Trinidad, “Lead–acid batteries with polymer-structured electrodes for electric-vehicle applications,” *Journal of Power Sources*, vol. 78, no. 1–2, pp. 220–230, Mar. 1999.

[36] T. Lee, P. Singh, M. V Baker, and T. B. Issa, “Polydivinylferrocene surface modified electrode for measuring state-of-charge of lead–acid battery,” *Journal of Power Sources*, vol. 182, no. 2, pp. 639–641, Aug. 2008.

[37] A. Gupta and V. Choudhary, “Electromagnetic interference shielding behavior of poly(trimethylene terephthalate)/multi-walled carbon nanotube composites,” *Composites Science and Technology*, vol. 71, no. 13, pp. 1563–1568, Sep. 2011.

[38] M. Morita, J.-L. Qiao, N. Yoshimoto, and M. Ishikawa, “Application of proton conducting polymeric electrolytes to electrochemical capacitors,” *Electrochimica Acta*, vol. 50, no. 2–3, pp. 837–841, Nov. 2004.

[39] S.-H. Lee, J. Y. Hwang, K. Kang, and H. Kang, “Fabrication of organic light emitting display using inkjet printing technology,” *Optomechatronic Technologies, 2009. ISOT 2009. International Symposium on*. pp. 71–76, 2009.

[40] D. R. Myers and A. P. Pisano, “Torque measurements of an automotive halfshaft utilizing a MEMS resonant strain gauge,” *Solid-State Sensors, Actuators and Microsystems Conference, 2009. TRANSDUCERS 2009. International*. pp. 1726–1729, 2009.

[41] J.-S. Heo, J.-H. Chung, and J.-J. Lee, “Tactile sensor arrays using fiber Bragg grating sensors,” *Sensors and Actuators A: Physical*, vol. 126, no. 2, pp. 312–327, Feb. 2006.

[42] D. Li, T. Zhao, L. Qian, Z. C. Yang, and D. Zhang, “A monolithic integrated micromachined piezoresistive flow sensor,” *Solid-State Sensors, Actuators and Microsystems Conference, 2009. TRANSDUCERS 2009. International*. pp. 260–263, 2009.

[43] A. Dehe, K. Fricke, K. Mutamba, and H. L. Hartnagel, “A piezoresistive GaAs pressure sensor with GaAs/AlGaAs membrane technology,” *Journal of Micromechanics and Microengineering*, vol. 5, no. 2, p. 139, 1995.

[44] E. O. Fernando Martinez, Gregorio Obieta, Ion Uribe, Tomasz Sikora, “Polymer-Based Self-Standing Flexible Strain Sensor,” *Journal of Sensors*, vol. 2010, 2010.

[45] C. W. M. Cheng, X. Y. Tsang, H. Y. J. Li, Y. Leung, M. Y. Tao, X. M. Cheng, X. X. Xue, P. Yuen, “Polypyrrole-Coated Large Deformation Strain Fabric Sensor and Its Properties Study,” *MATERIALS RESEARCH SOCIETY SYMPOSIUM PROCEEDINGS*, vol. 920, pp. 127–134, 2006.

[46] A. Tognetti, N. Carbonaro, G. Zupone, and D. De Rossi, “Characterization of a novel data glove based on textile integrated sensors,” *Annual International Conference of the IEEE Engineering in Medicine and Biology Society (EMBS ’06)*, pp. 2510–2513, 2006.

[47] V. Mohammadi, M. H. Sheikhi, S. Torkian, A. Barzegar, E. Masumi, and S. Mohammadi, “Design, modeling and optimization of a piezoelectric pressure

sensor based on thin-film PZT diaphragm contain of nanocrystalline powders," *Mechatronics and its Applications, 2009. ISMA '09. 6th International Symposium on*. pp. 1–7, 2009.

[48] I.-B. Kwon, M.-Y. Choi, and H. Moon, "Strain measurement using fiber optic total reflected extrinsic Fabry–Perot interferometric sensor with a digital signal processing algorithm," *Sensors and Actuators A: Physical*, vol. 112, no. 1, pp. 10–17, Apr. 2004.

[49] M. Fernández-Regúlez, J. A. Plaza, E. Lora-Tamayo, and A. S. Paulo, "Lithography guided horizontal growth of silicon nanowires for the fabrication of ultrasensitive piezoresistive strain gauges," *Microelectronic Engineering*, vol. 87, no. 5–8, pp. 1270–1273, May 2010.

[50] L. Lou, S. Zhang, W.-T. Park, L. Lim, D.-L. Kwong, and C. Lee, "Characterization of a multi-layered MEMS pressure sensor using piezoresistive silicon nanowire within large measurable strain range," *Nano/Micro Engineered and Molecular Systems (NEMS), 2012 7th IEEE International Conference on*. pp. 99–103, 2012.

[51] E. by A. D. Rodić, "Simultaneous Localization and Mapping (SLAM) of a Mobile Robot Based on Fusion of Odometry and Visual Data Using Extended Kalman Filter," in *Contemporary Robotics - Challenges and Solutions*, 2009, p. 392.

[52] B. Lee, S. Roh, and J. Park, "Current status of micro- and nano-structured optical fiber sensors," *Optical Fiber Technology*, vol. 15, no. 3, pp. 209–221, Jun. 2009.

[53] W. C. Roentgen, "About the changes in shape and volume of dielectrics caused by electricity," *Ann. Phys.*, vol. 11, no. 771–786, 1880.

[54] H. Wang and C. Li, "A Linear Dielectric EAP Actuator with Large Displacement Output," *Measuring Technology and Mechatronics Automation, 2009. ICMTMA '09. International Conference on*, vol. 1. pp. 73–76, 2009.

[55] Y. Bar-Cohen, "Biomimetics using electroactive polymers (EAP) as artificial muscles - A review," *Journal of Advanced Materials*, pp. 3–9, 2006.

[56] R. Shankar, T. K. Ghosh, and R. J. Spontak, "Dielectric elastomers as next-generation polymeric actuators," *Soft Matter*, vol. 3, no. 9, pp. 1116–1129, 2007.

[57] W. G. Nelson, *Piezoelectric Materials: Structure, Properties and Applications*. Nova Science Pub Incorporated, 2010.

[58] D. Kolev and V. Todorova, "Quasi 3D model of resonance piezoelectric array sensor," *Microelectronics Proceedings (MIEL), 2010 27th International Conference on*. pp. 205–208, 2010.

[59] B. Watson, J. Friend, and L. Yeo, “Piezoelectric ultrasonic micro/milli-scale actuators,” *Sensors and Actuators A: Physical*, vol. 152, no. 2, pp. 219–233, Jun. 2009.

[60] M. Martins, V. Correia, J. M. Cabral, S. Lanceros-Mendez, and J. G. Rocha, “Optimization of piezoelectric ultrasound emitter transducers for underwater communications,” *Sensors and Actuators A: Physical*, vol. 184, no. 0, pp. 141–148, Sep. 2012.

[61] a Ferreira, P. Cardoso, D. Klosterman, J. a Covas, F. W. J. van Hattum, F. Vaz, and S. Lanceros-Mendez, “Effect of filler dispersion on the electromechanical response of epoxy/vapor-grown carbon nanofiber composites,” *Smart Materials and Structures*, vol. 21, no. 7, p. 075008, Jul. 2012.

[62] RS-Components., “Strain gauge and load cells,” 1997. [Online]. Available: http://docs-europe.electrocomponents.com/webdocs/0099/0900766b80099349.pdf.

[63] L. Zhou, S. Jung, E. Brandon, and T. N. Jackson, “Flexible substrate micro-crystalline silicon and gated amorphous silicon strain sensors,” *Electron Devices, IEEE Transactions on*, vol. 53, no. 2. pp. 380–385, 2006.

[64] U. Schultes, Guenter; Koppert, Ralf; Goettel, Dirk; Freitag-Weber, Olivia; Probst, Anne C.; Werner, “New perspectives for pressure and force sensors Thin films combining high gauge factor and low TCR,” in *Smart Sensors, Actuators, and MEMS IV*, 2009, vol. 7362.

[65] P. Costa, J. Silva, V. Sencadas, R. Simoes, J. Viana, and S. Lanceros-Méndez, “Mechanical, electrical and electro-mechanical properties of thermoplastic elastomer styrene–butadiene–styrene/multiwall carbon nanotubes composites,” *Journal of Materials Science*, vol. 48, no. 3, pp. 1172–1179, 2013.

[66] C. Liu, V. B. Mungurwadi, and A. V Nandi, *Foundation of MEMS*. Prentice Hall, 2011.

[67] V. Hung, N. Minh, L. Minh, N. Hung, D. Dao, C. Hoang, R. Amarasinghe, B. Tung, and S. Sugiyama, “Design and Fabrication of a Miniaturized Three-Degree-of-Freedom Piezoresistive Acceleration Sensor Based on MEMS Technology Using Deep Reactive Ion Etching,” in *Physics and Engineering of New Materials*, vol. 127, D. Cat, A. Pucci, and K. Wandelt, Eds. Springer Berlin Heidelberg, 2009, pp. 377–383.

[68] C.-H. Wu, C. A. Zorman, and M. Mehregany, “Fabrication and testing of bulk micromachined silicon carbide piezoresistive pressure sensors for high temperature applications,” *Sensors Journal, IEEE*, vol. 6, no. 2. pp. 316–324, 2006.

[69] M. Sasaki, M. Tabata, and K. Hane, “Passivated Piezoresistive Rotation Angle Sensor Integrated in Micromirror,” *Optical MEMS and Nanophotonics, 2007 IEEE/LEOS International Conference on*. pp. 193–194, 2007.

[70] M. Sasaki, M. Tabata, and K. Hane, “Driving of Micromirror and Simultaneous Detection of Rotation Angle using Integrated Piezoresistive Sensor,” *Solid-State Sensors, Actuators and Microsystems Conference, 2007. TRANSDUCERS 2007. International*. pp. 2151–2154, 2007.

[71] Z. Zhou, M. Wong, and L. Rufer, “The design, fabrication and characterization of a piezoresistive tactile sensor for fingerprint sensing,” *Sensors, 2010 IEEE*. pp. 2589–2592, 2010.

[72] T. Lomas, A. Tuantranont, and A. Wisitsoraat, “Polysilicon Piezoresistive Tactile Sensor Array Fabricated by PolyMUMPs Process,” *Sensors, 2006. 5th IEEE Conference on*. pp. 1313–1316, 2006.

[73] V. M. Van Meer, D. Esteve, A. Giraud, and A. M. Gue, “2D Silicon Macro-Force Sensor for Tele-Operated Surgical Instrument,” *MEMS, NANO and Smart Systems, 2004. ICMENS 2004. Proceedings. 2004 International Conference on*. pp. 468–472, 2004.

[74] P. Brogueira, V. Chu, A. C. Ferro, and J. P. Conde, “Doping of amorphous and microcrystalline silicon films deposited by hot-wire chemical vapor deposition using phosphine and trimethylboron,” *Journal of Vacuum Science & Technology A: Vacuum, Surfaces, and Films*, vol. 15, no. 6. pp. 2968–2982, 1997.

[75] C. Grimaldi, T. Maeder, P. Ryser, and S. Strässler, “Piezoresistivity and conductance anisotropy of tunneling-percolating systems,” *Physical Review B*, vol. 67, no. 1, p. 14205, Jan. 2003.

[76] M. Hussain, Y.-H. Choa, and K. Niihara, “Conductive rubber materials for pressure sensors,” *Journal of Materials Science Letters*, vol. 20, no. 6, pp. 525–527, 2001.

[77] W. Heywang, K. Lubitz, and W. Wersing, *Piezoelectricity: Evolution and Future of a Technology*. Springer London, Limited, 2008, p. 580.

[78] D. Braun and A. J. Heeger, “Visible light emission from semiconducting polymer diodes,” *Applied Physics Letters*, vol. 58, no. 18. pp. 1982–1984, 1991.

[79] B. M. Chandrasekhar, S. Guha, and W. Graupner, “Squeezing Organic Conjugated MoleculesĐ What Does One Learn ?**,” no. 8, pp. 613–618, 2001.

[80] D. Klempner, V. Sendijarevi′c, V. Sendijarevic, and R. M. Aseeva, *Handbook of polymeric foams and foam technology: Daniel Klempner and Vahid Sendijarevic*. Hanser, 2004.

[81] J. K. Fink, *Polymeric Sensors and Actuators*. Wiley, 2012, p. 536.

[82] J. Mei, M. R. Lovell, and M. H. Mickle, “Formulation and processing of novel conductive solution inks in continuous inkjet printing of 3-D electric circuits,” *Electronics Packaging Manufacturing, IEEE Transactions on*, vol. 28, no. 3. pp. 265–273, 2005.

[83] A. Benchirouf, E. Sowade, A. Al-Hamry, T. Blaudeck, O. Kanoun, and R. Baumann, “Investigation of RFID passive strain sensors based on carbon nanotubes using inkjet printing technology,” *Systems, Signals and Devices (SSD), 2012 9th International Multi-Conference on*. pp. 1–6, 2012.

[84] K. Kirschenmann, K. W. Whites, and S. M. Woessner, “Inkjet printed microwave frequency multilayer antennas,” *Antennas and Propagation Society International Symposium, 2007 IEEE*. pp. 924–927, 2007.

[85] F. Molina-Lopez, D. Briand, N. F. de Rooij, and M. Smolander, “Fully inkjet-printed parallel-plate capacitive gas sensors on flexible substrate,” *Sensors, 2012 IEEE*. pp. 1–4, 2012.

[86] K. Crowley, A. Morrin, M. R. Smyth, A. J. Killard, R. Shepherd, M. in het Panhuis, and G. G. Wallace, “Fabrication of chemical sensors using inkjet printing and application to gas detection,” *Sensors, 2008 IEEE*. pp. 13–16, 2008.

[87] S. Chung, S. O. Kim, S.-K. Kwon, C. Lee, and Y. Hong, “All-Inkjet-Printed Organic Thin-Film Transistor Inverter on Flexible Plastic Substrate,” *Electron Device Letters, IEEE*, vol. 32, no. 8. pp. 1134–1136, 2011.

[88] C. Sriprachuabwong, C. Srichan, T. Lomas, and A. Tuantranont, “Simple RC low pass filter circuit fabricated by unmodified desktop inkjet printer,” *Electrical Engineering/Electronics Computer Telecommunications and Information Technology (ECTI-CON), 2010 International Conference on*. pp. 929–932, 2010.

[89] A. Shafiee, M. M. Salleh, and M. Yahaya, “Fabrication of organic solar cells based on a blend of donor-acceptor molecules by inkjet printing technique,” *Semiconductor Electronics, 2008. ICSE 2008. IEEE International Conference on*. pp. 319–322, 2008.

[90] X. T. Ltd, “Industrial inkjet printing,” *2012*, 2012. [Online]. Available: http://www.xennia.com. [Accessed: 15-Dec-2012].

[91] L. R. Allain, D. N. Stratis-Cullum, and T. Vo-Dinh, “Investigation of microfabrication of biological sample arrays using piezoelectric and bubble-jet printing technologies,” *Analytica Chimica Acta*, vol. 518, no. 1–2, pp. 77–85, Aug. 2004.

[92] A. De Marcellis, A. Depari, G. Ferri, A. Flammini, D. Marioli, V. Stornelli, and A. Taroni, “A CMOS Integrable Oscillator-Based Front End for High-Dynamic-Range Resistive Sensors,” *Instrumentation and Measurement, IEEE Transactions on*, vol. 57, no. 8. pp. 1596–1604, 2008.

[93] C. Yang, A. Mason, J. Xi, and P. Zhong, “Configurable Hardware-Effcient Interface Circuit for Multi-Sensor Microsystems,” *Sensors, 2006. 5th IEEE Conference on*. pp. 41–44, 2006.

[94] C. N. Kotanen, F. G. Moussy, S. Carrara, and A. Guiseppi-Elie, “Implantable enzyme amperometric biosensors,” *Biosensors and Bioelectronics*, vol. 35, no. 1, pp. 14–26, May 2012.

[95] J. Xi, C. Yang, A. Mason, and P. Zhong, “Adaptive Multi-Sensor Interface System-On-Chip,” *Sensors, 2006. 5th IEEE Conference on*. pp. 50–53, 2006.

[96] N. Yazdi, A. Mason, K. Najafi, and K. D. Wise, “A generic interface chip for capacitive sensors in low-power multi-parameter microsystems,” *Sensors and Actuators A: Physical*, vol. 84, no. 3, pp. 351–361, Sep. 2000.

[97] M. N. Gasson, E. Kosta, and D. M. Bowman, *Human ICT Implants: Technical, Legal and Ethical Considerations*. T. M. C. Asser Press, 2012.

[98] J. Cavuoto, “Neural engineering’s image problem,” *Spectrum, IEEE*, vol. 41, no. 4. pp. 32–37, 2004.

[99] R. F. Weir, P. R. Troyk, G. DeMichele, and T. Kuiken, “Implantable myoelectric sensors (IMES) for upper-extremity prosthesis control- preliminary work,” *Engineering in Medicine and Biology Society, 2003. Proceedings of the 25th Annual International Conference of the IEEE*, vol. 2. pp. 1562–1565 Vol.2, 2003.

[100] H. Gensler, R. Sheybani, P.-Y. Li, R. Lo, S. Zhu, K.-T. Yong, I. Roy, P. N. Prasad, R. Masood, U. K. Sinha, and E. Meng, “Implantable MEMS drug delivery device for cancer radiation reduction,” *Micro Electro Mechanical Systems (MEMS), 2010 IEEE 23rd International Conference on*. pp. 23–26, 2010.

[101] A. Alomainy and Y. Hao, “Modeling and Characterization of Biotelemetric,” vol. 57, no. 4, pp. 999–1005, 2009.

[102] J. Kim and Y. Rahmat-samii, “Implanted Antennas Inside a Human Body :,” vol. 52, no. 8, pp. 1934–1943, 2004.

[103] T. Weiland, “A Discretization Method for the Solution of Maxwell’s Equations for Six-Component Fields,” *Electronics and Communications AEUE*, vol. 31, pp. 116–120, 1977.

[104] L. C. Chirwa, P. a Hammond, S. Roy, and D. R. S. Cumming, “Electromagnetic radiation from ingested sources in the human intestine between 150 MHz and 1.2 GHz.,” *IEEE transactions on bio-medical engineering*, vol. 50, no. 4, pp. 484–92, Apr. 2003.

[105] Y. Ahmed, Y. Hao, and C. Parini, “A 31.5 GHz Patch Antenna Design for Medical Implants,” *International Journal of Antennas and Propagation*, vol. 2008, pp. 1–6, 2008.

[106] W. G. Scanlon, J. B. Burns, and N. E. Evans, “Radiowave propagation from a tissue-implanted source at 418 MHz and 916.5 MHz.,” *IEEE transactions on bio-medical engineering*, vol. 47, no. 4, pp. 527–34, Apr. 2000.

[107] M. Z. Azad and M. Ali, “A Miniature Implanted Inverted-F Antenna for GPS Application Antenna for GPS Application,” vol. 57, pp. 1854–1858, 2009.

2. Piezoresistive silicon thin film sensor array for biomedical applications

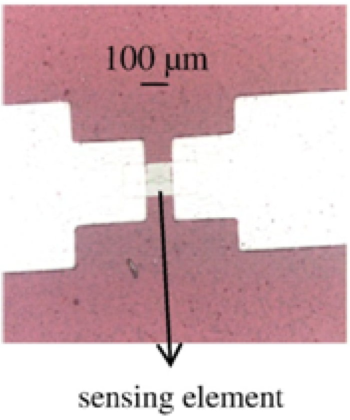

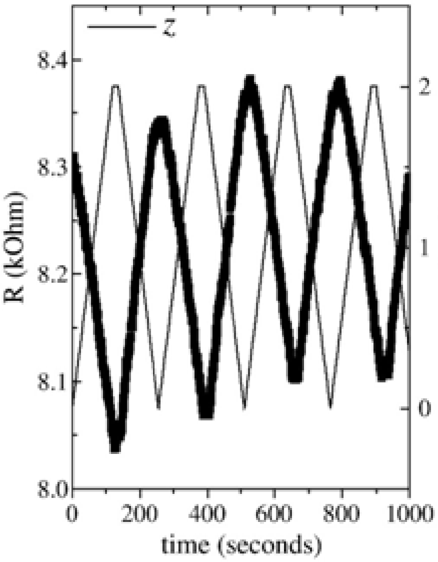

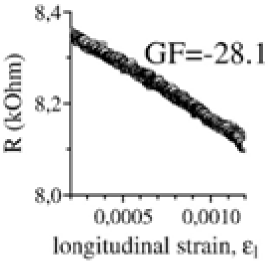

This chapter is based on the following publication: P. Alpuim, V. Correia, E.S. Marins, J. G. Rocha, I.G. Trindade and S. Lanceros-Méndez. *Piezoresistive silicon thin film senor array for biomedical applications*. Thin solid Films. 2011. 519: 4574-4577.

2.1. Introduction

Since the piezoresistive property of silicon was first reported by C. Smith [1] it has been used in different kinds of sensors that make use of the change of conductivity under strain to probe and measure deformation of surfaces and solids. The piezoresistive devices can be simple n- and p-type resistors, field-effect N- and P-MOS transistors or p-i-n and Schottky diodes [2 - 4]. Usually, these devices are fabricated on Si wafers using standard lithographic techniques [3]. Doped hydrogenated nanocrystalline silicon thin films, nc-Si:H, exhibit piezoresistive behavior that is some type of average over all its randomly oriented crystallites of the piezoresistrive response of a single Si crystal. The effect is expected to be weaker than in c-Si since only those crystallites with the proper orientation relative to the principal axis of the applied stress will contribute strongly to the overall effect. In the line of this reasoning, n-type nc-Si:H films have negative gauge factor (GF) ~ -30 (GF is the proportionality constant relating relative resistance change and applied strain)[5] and [6] reminiscent of the larger in absolute value n-type c-Si π-coefficient: $\pi 11 = -102 \times 10-11$ Pa-1 (π-coefficients are defined as the relative change in resistivity per stress) [1].

Hot-wire chemical vapor deposition has proved to be a very adequate technique to deposit hydrogenated nanocrystalline silicon thin films, nc-Si:H, due to its high efficiency in breaking H2 molecules into atomic hydrogen that diffuses from the heated tungsten or tantalum filament to the growing film surface where it very effectively promotes crystalline growth [7]. Although nc-Si:H has a much lower carrier mobility than c-Si due to carrier scattering at grain boundaries [8], it can, however, be deposited at low temperatures on virtually any type of substrate that stands the deposition temperature. In the present work we use polyimide plastic foil as substrate and deposit n^{+}-nc-Si:H by Hot-wire chemical vapor deposition (HWCVD) at a temperature of 150 °C thus obtaining a flexible composite of an isolating polymer covered by a piezoresistive semiconductor. Previous work has shown that, as far as piezoresistance is concerned, nc-Si:H films are isotropic in planes perpendicular to the growth direction [9]. The combined characteristics of flexibility, piezoresistance and isotropy allow the design of novel types of strain or shape sensing devices, for example for biomedical applications. It is shown that large-area flexible thin film Si piezoresistors deposited by

HWCVD on plastic substrates can respond and survive to quasi-static as well as to dynamical loading conditions up to at least hundreds of Hertz. The fabrication of micro-devices using standard lithographic techniques with minor adaptations due to the chemistry of the plastic substrates is demonstrated. Finally, the control electronics for data acquisition using an array of resistors is proposed. Data processing, storage and communication are also addressed.

2.2. Experimental

2.2.1. Hot-wire chemical vapor deposition.

Depositions were performed in a load-locked research chamber under high-vacuum conditions (base pressure better than 10−6 Torr). After loading, before starting deposition and while heating the substrates to the deposition temperature of 150 °C, the time necessary for the pressure to recover to the pre-load values was allowed (this could take tens of minutes due to the long degassing time of the polyimide foils). A single S-shaped tantalum filament, 0.5 mm thick and 14 cm long, was heated up to 1750 °C. Filament-to-substrate distance was 7 cm. The filament was first heated up to the working temperature, in a hydrogen atmosphere, and then the source gases, SiH4 and PH3 (for gas phase P-doping), were added while the hydrogen flow was adjusted to a value corresponding to 95% of the total gas flow. Working gas pressure was 40 mTorr for all depositions. During the filament heating time, a shutter was closed in order to protect the substrate from spurious species emitted from the filament. Deposition rate was ~ 1.5 Å/s and the final thickness of the films was in the range 100–150 nm.

2.2.2. Sensor array fabrication

nc-Si:H films deposited on square shaped (side length = 35 mm) polyimide (PI) flexible substrates with thickness ds = 125 μm were patterned by photolithography into strain sensing microresistors in an array with seven lines and four columns. The PI substrates were glued with photoresist (PHR) to a 2″ Si carrier wafer for processing. Each sensing element consists of rectangular islands with lateral dimensions (length × width) in the range from 210 μm × 70 μm to 450 μm × 150 μm, connected to metallic leads at each end of the island and extending to large pads (3 mm × 2 mm). Two masks were used to define the sensors: first, a bright field mask defined the semiconductor islands pattern; second, a dark field mask defined the electrically conductive leads and pads in a lift-off process, using a positive PHR (AZ Electronic Materials GmbH).

A reactive ion etching (RIE) step was used to etch the nc-Si:H islands (etch rate ~ 28 nm/min) on the PI substrate. Under the processing conditions used (pressure = 55 mTorr, Power = 150 W, CHF3flow = 50 sccm, SF6 flow = 5 sccm and O_2 flow = 5 sccm), the Si etch rate was approximately 28 nm/min. The metallic leads and pads, consisting of a tri-layered film of Ta 10 nm/Al 40 nm/Ta 5 nm, were deposited by ion beam deposition followed by lift-off in acetone soak.

Large-area piezoresistors with a similar structure to that of the individual microresistors were fabricated using shadow masks in a four lines by two columns matrix. The piezoresistor dimensions are set by the 1 mm gap between the contacts, the width of the island (3 mm) and the thickness of the films.

2.3. Results and discussion

Figure 2.1 shows the piezoresistive response, under loading by 4-point bending cycles (Shimadzu-AG-IS 500 N), of one nc-Si:H microresistor with thickness 120 nm, belonging to a larger array fabricated on a 125 µm thick polyimide substrate. Figure 2.1a) shows the microresistor width × length dimensions of 100 × 100 μm^2. The bright parts of the optical micrograph are the metallic leads and the darker zone is the PI substrate. Figure 2.1b) shows the resistance, R (thick line, left axis), and the vertical displacement, z (thin line, right axis), of the inner loading bars of the 4-point bending bridge (4PBB) as a function of time. The 4PBB is operated in a quasi-static mode (velocity of the loading bars v = 1 mm/min) during a four-cycles loading experiment. The microresistors stand in the region between the inner loading bars of the 4PBB, on the tensile surface of the specimen. In that region the longitudinal strain in the film as a function of the displacement of the bars, assuming that the neutral plane of the sensor is symmetrically placed between the two free surfaces of the substrate, is given by [10]:

$$\varepsilon_{xx} = \frac{3d_s Z}{(3l - 4a)a}$$

(eq. 2.1)

where *l* is the distance between the 4PBB outer loading bars and *a* is the distance between the first and second loading bars. In our set-up *l* = 25 mm and *a* = 7.5 mm. Using Eq. (2.1), the resistance (Agilent 34401A digital multimeter) of the microresistor can be plotted as a function of the applied strain, which is done in figure 2.1c).

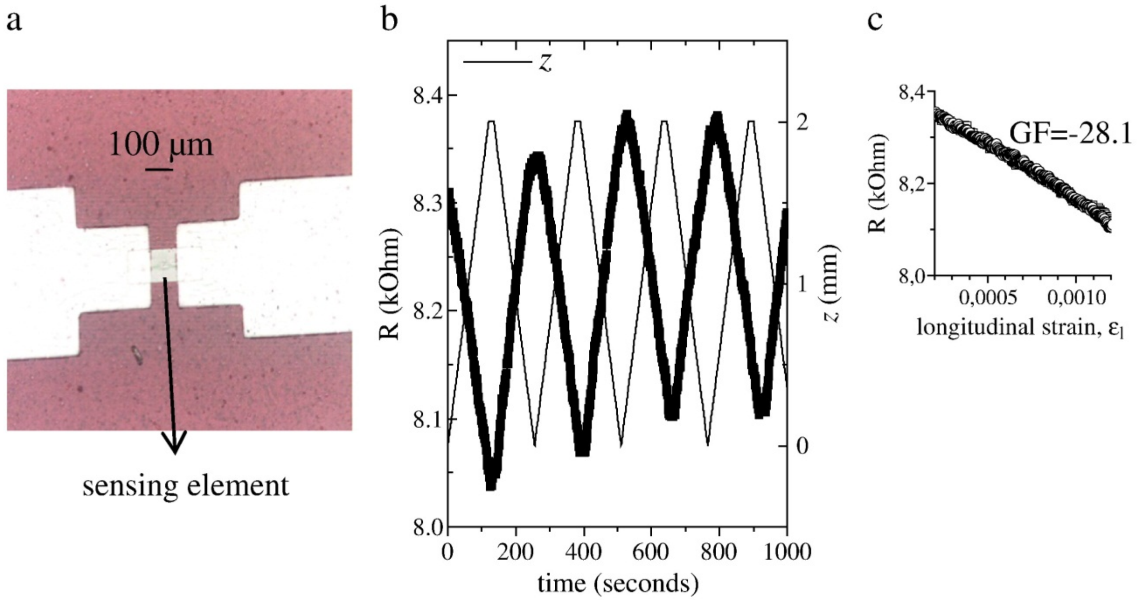

Figure 2.1 - Piezoresistive response, under 4-point bending loading cycles of one nc-Si:H microresistor with dimensions W×L=100×100 µm^2 and thickness 120 nm on a 125 µm thick polyimide substrate. a) Optical micrograph of sensor and metallic leads; b) Sensor resistance, R (left axis) and vertical displacement of loading bars, z (right axis) as a function of time; c) Sensor resistance, R, as a function of strain, ε, calculated from data in b) using eq. (2.2). The slope is the GF (−28.1).

The slope of the graph is the longitudinal GF of the n^+–nc-Si:H sensing element. Here, longitudinal means that resistor current and applied strain are parallel. From the figure, GF = −28.1. Notice the minus sign of the GF, meaning that the resistance of the sensor decreases (increases) when tensile (compressive) strain is applied to the substrate. Hence the phase opposition that is patent between the two graphs of figure 2.1b).

Figure 2.2 shows the time-domain results of the dynamic actuation of large-area sensors. Each piezoresistor, RS, in the sensor is connected through the pads to a Wheatstone bridge external circuit in a quarter-bridge configuration and to a NI-USB 6210 data acquisition module connected to a PC laptop. The Wheatstone bridge is operated as close as possible to its maximum sensitivity point [r = 1 in (eq. 2.2)], using two 27 kΩ resistances, a value close to RS. A variable resistor, R4, is used to set the bridge into equilibrium (V_{out} = 0 V) while the sensor is in the flat, unstrained condition (RS = R_0).

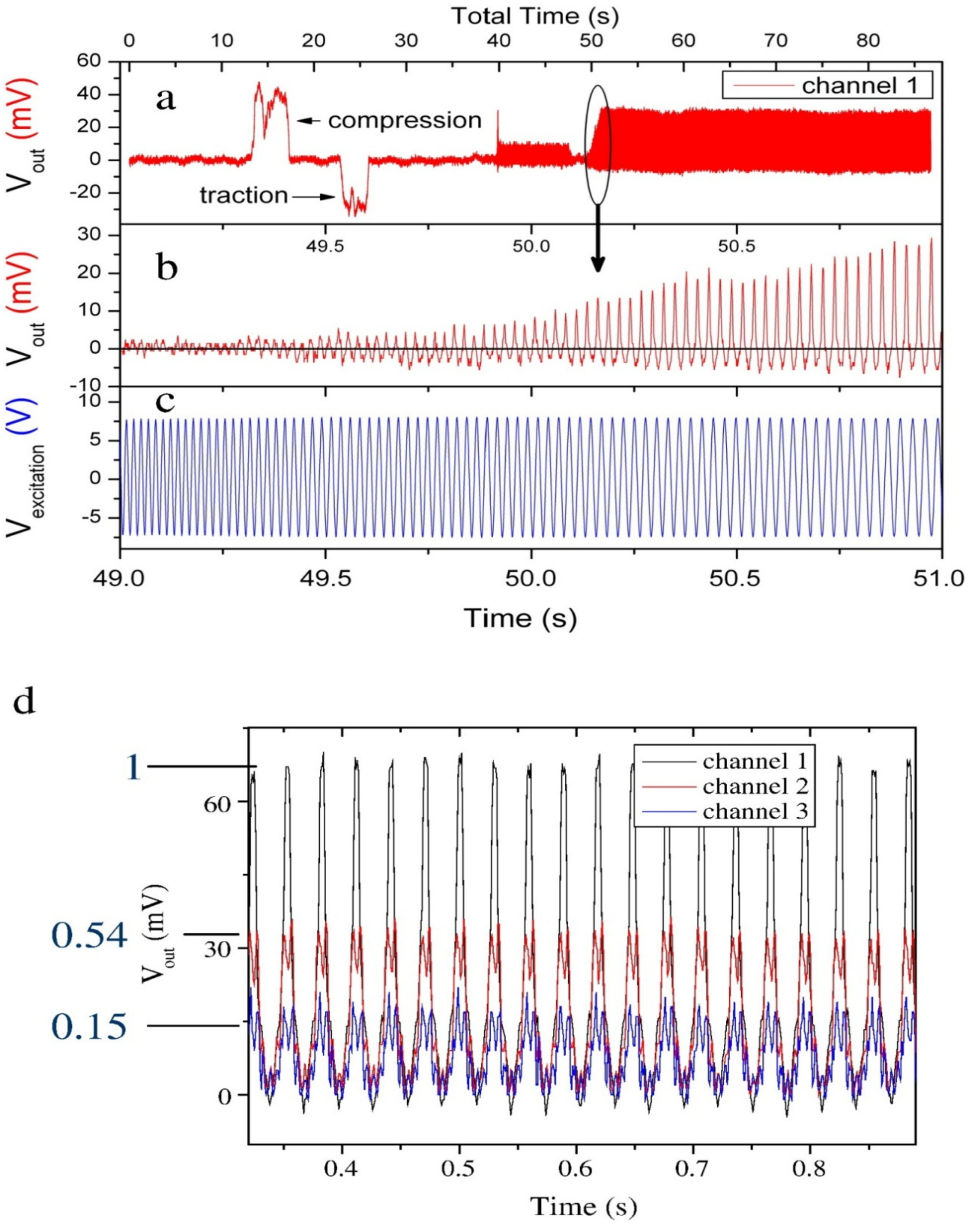

Figure 2.2 - Time-domain results of the dynamic actuation of large-area sensors. Each piezoresistor, RS, in the sensor is part of a Wheatstone bridge circuit in a quarter-bridge configuration. In a) the output voltage of the sensor (the unbalanced V_{out} of the bridge) is displayed. In b) a detail of graph a), between 49 and 51 s, is zoomed in. In c) the constant

amplitude, variable frequency excitation voltage, Vexcitation, driving the mechanical oscillator (see text) is shown for the time interval [49,51] s. In d) the signal amplitudes and their ratio (1 : 0.54 : 0.15) given by three piezoresistors in the sensor (channels 1 to 3) located at different distances from the clamped edge of the sensor.

The output voltage of the sensor under applied strain is the unbalanced V_{out} of the bridge. No filtering, amplification, or other type of signal conditioning is used. V_{out} is related to the relative resistance change of the piezoresistor by [11]:

$$V_{out} = \frac{r}{(1+r)^2} \frac{\Delta R_S}{R_0} V_{IN}$$

(eq. 2.2)

where $r = 27$ kΩ/R4 and $V_{IN} = 5$ V is the voltage supplied to the bridge by the USB bus.

Dynamic tests were performed using a Frederiksen Vibration Generator driven by a Function Generator that applied forced sinusoidal oscillations to its axle in the range 0.1–100 Hz. The rectangular sensor is clamped to the vibrating axle of the Generator by one of its smaller edges in a cantilever configuration. Data acquisition rate was set to 1000 −1s.

Figure 2.2a) shows V_{out} for the entire 86.775 s time interval that lasted the experience. During the first 37.7 s the oscillator axle was moving up and down at a frequency of f = 0.3 Hz. At this quasi-DC frequency the sensor basically executes translation following the axle where it is fixed and does not vibrate. In this region the sensor signal is essentially noise. The two bumps centered at t = 15 s and t = 25 s, respectively, are the response to large deflections up (compression) and down (traction) imposed to the sensor with the operator finger, as a test. For t > ~ 40 s the sensors start to oscillate at the frequency of the excitation but the amplitude of the signal V_{out} strongly changes at some frequencies. If one concentrates on the transition that occurs in V_{out} between t ~ 49 s and 51 s [figure 2.2b)] and compares to the constant-amplitude excitation, Vexcitation, driving the oscillator in the same time interval [figure 2.2c)], it is clear that while the frequency of excitation decreases from ~ 55 Hz to 34.3 Hz, the amplitude V_{out} increases (compressive side) from ~ 2 mV to V_{out} ~ 30 mV.

The reason is that the plastic substrate has a mechanical resonance mode at this frequency. This fact was visible to the naked eye and was confirmed by finite element simulation. Figure 2.2d) shows the signals recorded at the resonance condition from three piezoresistors in the sensor (channels 1 to 3) situated at three different distances from the clamped edge of the sensor, along a longitudinal axis. The ratio of the signal amplitudes (1 : 0.54 : 0.15) is the same as the ratio between the strains felt by the three piezoresistors at the resonance, according to the finite element simulation of the resonant mode. These results demonstrate the accuracy of the sensor as a strain-voltage transducer.

In moving from test structures with a few resistors to arrays of sensors the readout electronics should be re-designed. The most common techniques of measuring resistance changes are based either on four wires or in Wheatstone bridges (see above). However, these techniques are not suitable when the resistive elements are disposed into a matrix form. On the other hand, with a two wires technique, it is possible to perform the readout of a resistive matrix without switching elements (e.g. MOSFETs) inside it, which greatly simplifies the fabrication process. In this technique, a voltage is applied to each row and the current is measured in each column. The readout can then be performed by scanning the array using a mutiplexer on each row and column of the matrix. The digital data is then processed, interpreted and stored internally by an ultra low-power micro controller, also responsible for the communication of two-way wireless data, e.g. from inside to outside the human body in case of invasive applications. Figure 2.3a) shows the readout circuit for a 4 × 4 matrix, where the switches are connected to read R11. The matrix columns that are not being read must be connected to ground (and not to high impedance). As the impedance of the current-to-voltage converter, formed by A1 and Rf in figure 2.3a), is very low, R12, R13 and R14 are shunted and their currents are null. Otherwise, the currents of these resistors would affect the measurement of R11. The currents of R21, R31 and R41 are not null, but they flow directly to the ground. These currents cause a voltage drop in the switch and thus an error in the measurement of R11. This error increases with the resistance of the switch, so, it must be kept as low as possible.

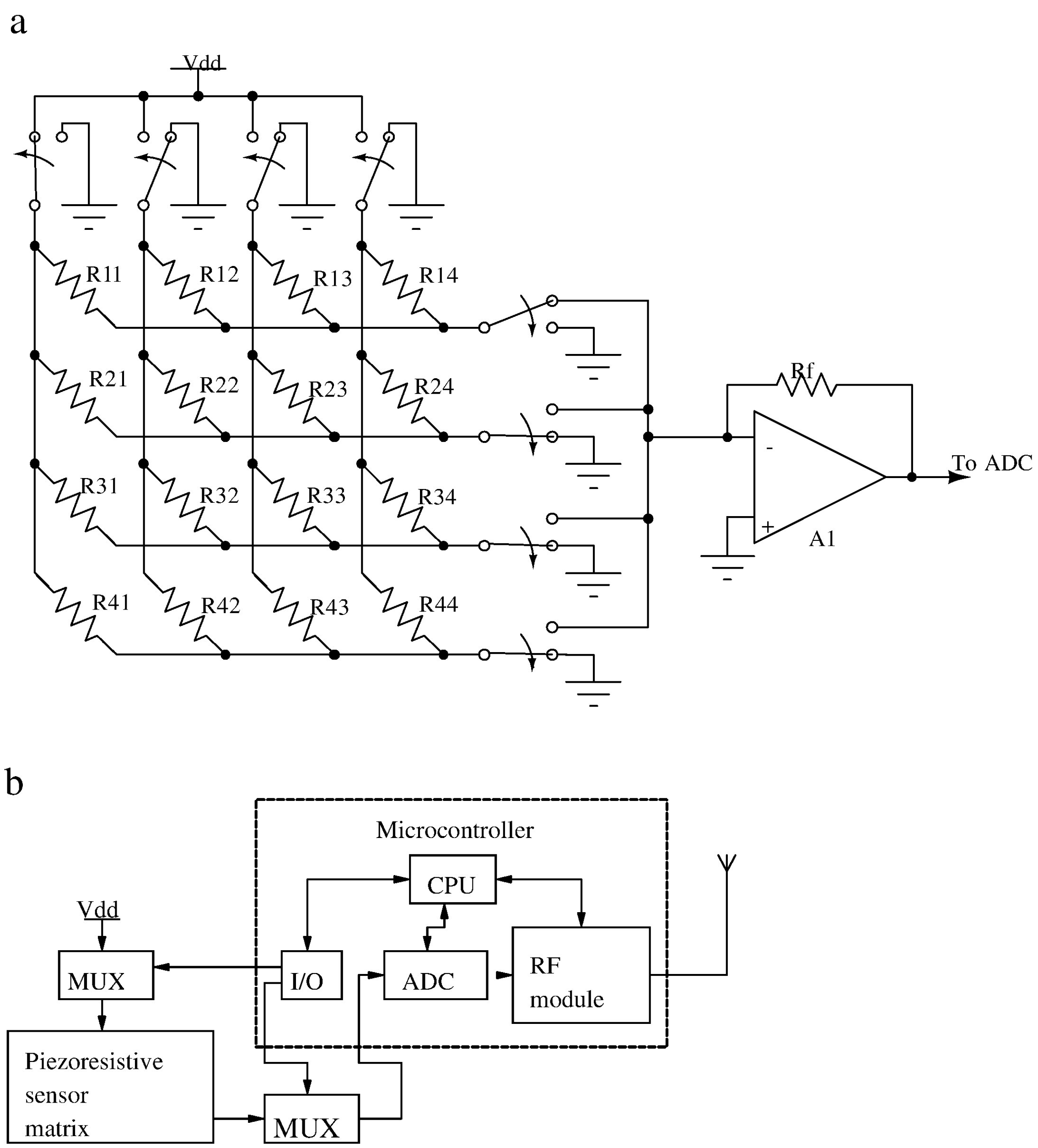

Figure 2.3 - a) Readout circuit for a 4×4 sensor array. The switches are connected in the right position for reading R11. In this case, a voltage is applied to R11 and its current is measured. R12, R13 and R14 are shunted, so their currents are null. b) Block diagram of the sensor electronic interface.

The piezoresistive sensor matrix output signals are multiplexed in time and then converted to digital by the analogic-digital converter (ADC) [see figure 2.3b)]. Afterward, they are read by the central processing unit (CPU), which sends them to the radio-frequency (RF) module, in order to be transmitted to a remote computer. The

CPU, ADC and RF module are internal components of a microcontroller, as well as the input/output (I/O) interface, which is used to control the multiplexers.

2.4. Conclusions

Strain sensors based on the piezoresistive property of n^+–nc-Si:H thin film microresistors were fabricated by HWCVD at 150 °C on plastic substrates using standard lithographic techniques. For large-area devices the piezoresistive response was converted in an output voltage by use of a Wheatstone bridge circuit in the quarter-bridge configuration. V_{out} thoroughly monitored the mechanical oscillations imposed to the sensor and accurately detected its resonance frequency peak, confirmed by finite element analysis. Microresistors, with gauge factor −28.1, followed the low-frequency oscillations of a four-point bending bridge. A two-wire readout circuit was designed to operate the sensor array without switching elements. Data will be subsequently processed and stored internally by a microcontroller, also responsible for the communication of two-way wireless data.

2.5. References

[1] C. S. Smith, "Piezoresistance Effect in Germanium and Silicon," Physical Review, vol. 94, pp. 42-49, 1954.

[2] W. G. Pfann and R. N. Thurston, "Semiconducting Stress Transducers Utilizing the Transverse and Shear Piezoresistance Effects," *Journal of Applied Physics,* vol. 32, pp. 2008-2019, 1961.

[3] S. Middelhoek, "Quo vadis silicon sensors?," *Sensors and Actuators A: Physical,* vol. 41, pp. 1-8, 1994.

[4] J. Bartholomeyczik, S. Brugger, P. Ruther, and O. Paul, "Multidimensional CMOS in-plane stress sensor," *Sensors Journal, IEEE,* vol. 5, pp. 872-882, 2005.

[5] S. Nishida, M. Konagai, and K. Takahashi, "Piezoresistive Effect of Hydrogenated Microcrystalline Silicon Prepared by Plasma- and Photo-

Chemical Vapor Deposition," *Japanese Journal of Applied Physics,* vol. 25, p. 17, 1986.

[6] P. Alpuim, V. Chu, and J. P. Conde, "Piezoresistive sensors on plastic substrates using doped microcrystalline silicon," *Sensors Journal, IEEE,* vol. 2, pp. 336-341, 2002.

[7] J. P. Conde, P. Brogueira, and V. Chu, "Amorphous and microcrystalline silicon films obtained by hot-wire chemical vapour deposition using high filament temperatures between 1900 and 2500°C," *Philosophical Magazine Part B,* vol. 76, pp. 299-308, 1997/09/01 1997.

[8] J. Kanicki, *Amorphous and Microcrystalline Semiconductor Devices: Materials and Device Physics*: Artech House, 1992.

[9] J. G. P. Alpuim, P. Gieschke, C. Ehling, J. Kistner, N.J. Gonçalves, M.I.Vasilevskiy, O. Paul, , " Oral communication EMRS Spring Meeting 2010, Symposium A," ed. Congress Center Strasbourg, France, 2010.

[10] S. Timoshenko, *Strength of materials*. Malabar, FL: Krieger, 1976.

[11] W. H. Paul Horowitz, *The Art of Electronics*, 2nd Edition ed.: Cambridge University Press, 1989.

3. Piezoresistive sensors for force mapping of hip-prostheses

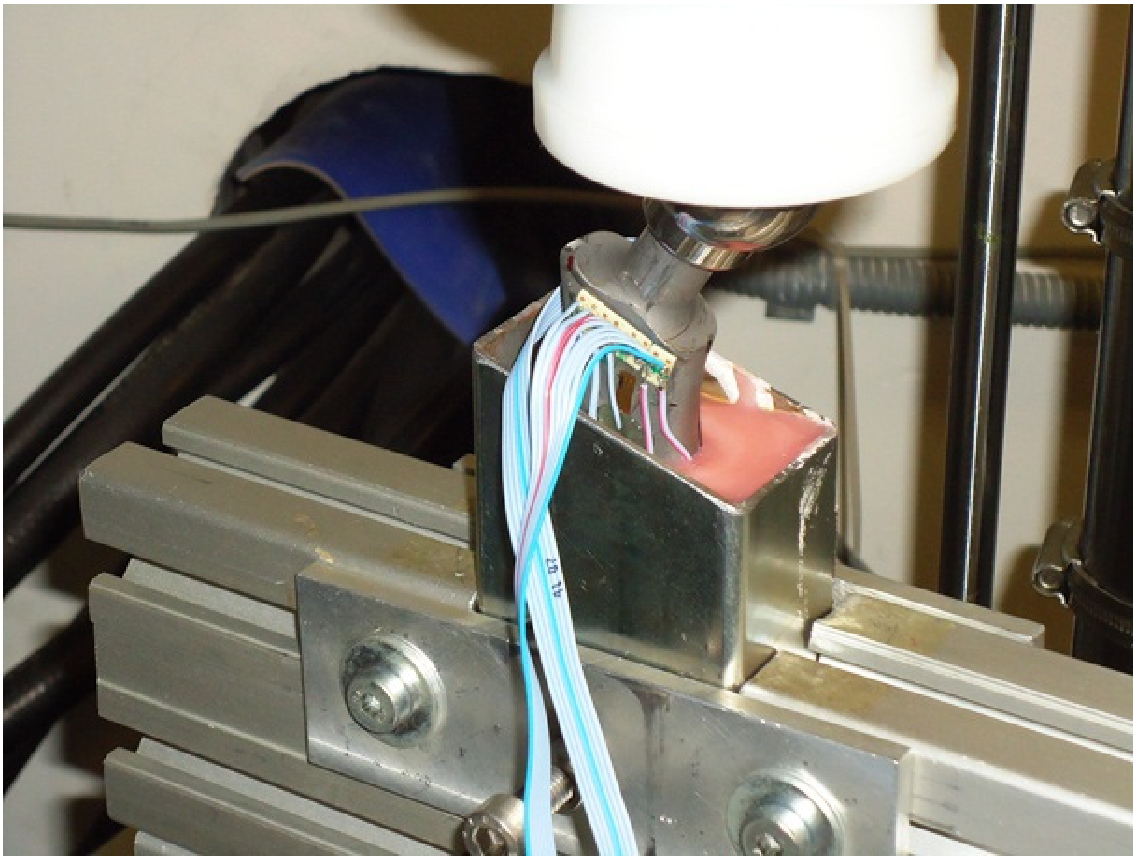

This chapter is based on the following publication: V. Correia , V. Sencadas, M. S. Martins, C. Ribeiro, P. Alpuim, J. G. Rocha, I. Morales, C. Atienza, and S. Lanceros-Mendez. *Piezoresistive sensors for force mapping of hip-prostheses.* Accepted in Sensors and Actuators A, 2012.

3.1. Introduction

The use of artificial prosthetic replacements has become an important surgical procedure in orthopedic human joint diseases. The success of this kind of procedure largely depends on the fixation of the artificial prosthetic component after being implanted in the thighbone [1]. Typically, hip-joint prosthesis consists of a ball and a socket joint [2].

Most frequent fixation problems are related to infection, wear and wear particulates generated by friction between the joint and the bone, or even between the femoral cup and the joint, migration and failure of the implants, and loosening. These problems manifest into osteolysis in the bone bed which is the major cause of long term loosening, mostly for the femoral stem. Some problems were identified that cause loosening of the implant, thereby dramatically shortening its lifetime, such as mismatch of the physical properties between tissues and implant, low biocompatibility of the implant, deterioration of the physical properties of implant materials, and bad design , among others [3].

The biocompatibility and bio-stability with the body tissues are key issues of any implant material used for the manufacture of hip-joint prosthesis. The physical and chemical properties of the materials must match the respective function of the prosthetic component and should not undergo any changes under the influence of the relatively aggressive biologic environment in the human body [4]. The materials to anchor stems that are subjected to bending and torsional stresses should be selected with regard to their high yield, fatigue strength, and toughness. Permanent deformations, incipient cracks and even fatigue fractures of loosened femoral component stems can in this way be prevented. A smooth operation of the artificial joint and its anchorage, especially in the first stage of implantation inside human body, is critical for the patient comfort and for the success of the hip-joint performance at long term service [4]. There is insufficient data available regarding the hip-joint performance inside the human patient, and consequently no information is available how the prosthesis behaves over time and, in particular, during the first days of post medical procedure. Information concerning mechanical stress of bone cement and hip-joint small dislocations monitoring are fundamental to promote high durability of the prosthesis, comfort and reliability to the patient. In this sense strong efforts are being done in order to develop sensors for the measurement of cement-prostheses interface forces based on different transducers and geometries [5-10], but the issue is far from being solved for practical situations.

Thin-film silicon piezoresistive sensors attract particular attention due to their versatility, widespread application and due to their convenience for integration in microsystems [11]. Fabrication of such sensors requires a number of technological steps that influences the sensor properties, as well as their reliability [11]. The sensors were deposited by hot-wire chemical vapor deposition, which has proven to be a versatile and suitable technique to obtain highly doped hydrogenated nanocrystalline silicon thin films (nc-Si:H) [12].

The present work shows an approach to monitoring mechanical stresses over time in a prosthesis. High sensitivity silicon piezoresisitive thin-film sensors were fabricated and attached to prosthesis. Their performance was compared with that of commercial strain gauge sensors.

3.2. Experimental

Nanocrystalline silicon deposition on polyimide substrates was performed in a load-locked chamber under high-vacuum conditions (base pressure better than 10-6 Torr). After loading, before starting deposition, the substrates were allowed to degase while heating to the deposition temperature of 150 ºC, up to the point where the chamber pressure recovered to the pre-load values. A single tantalum filament, 0.5 mm thick and 14 cm long, was heated up to 1750 ºC. Filament-to-substrate distance was 7 cm. The filament was first heated up to the working temperature, in a hydrogen atmosphere, and then the source gases, SiH4 (as a Si precursor) and PH3 (as a P precursor) were added while the hydrogen flow was adjusted to a value corresponding to 95 % of the total gas flow. Working pressure was 40 mTorr for all depositions. During the filament heating time, a shutter was closed in order to protect the substrate from spurious species emitted from the filament. Deposition rate was ~1.5 nm/s and final thickness of the films was in the range 100 – 150 nm. More details on the preparation procedure and on the characteristics of the sensors can be found in [12], [13].

Commercial metallic piezoresistive sensors with a Gauge Factor (GF) of 2 (reference number: N11-FA-5-120 (11, 16, 23)) were purchased from RS Components. All piezoresistive sensors were placed in a commercial hip-joint prosthesis from Lima-Lto (Orthopaedic, L.C.) taking into account the calculated stress distribution obtained by computer simulation. The thin-film silicon and commercial sensor gauges were placed in opposite sides of the implant, in positions exactly symmetric relative to the symmetry plane of the prosthesis. After placing the sensors in their positions, bone cement (SR Triplex Cold Polymer) was prepared according to manufacturer instructions by mixing powder poly(methyl methacrylate) (PMMA, from *Ivoclarvivadent*) with the liquid monomer at room temperature (Ivoclarvivadent).

The hip-joint prosthesis was then placed in the middle of a carbon steel machined rectangular mold. The prosthesis with the attached sensors was fitted into a mold cavity, the bone cement was poured into the other side of the cavity and pressure was applied by hand to keep the hip-joint prosthesis well bonded to the cement. After the polymerization of the bone cement was complete, the specimens were transferred to a universal testing machine *Instron* 8501 (figure 3.1).

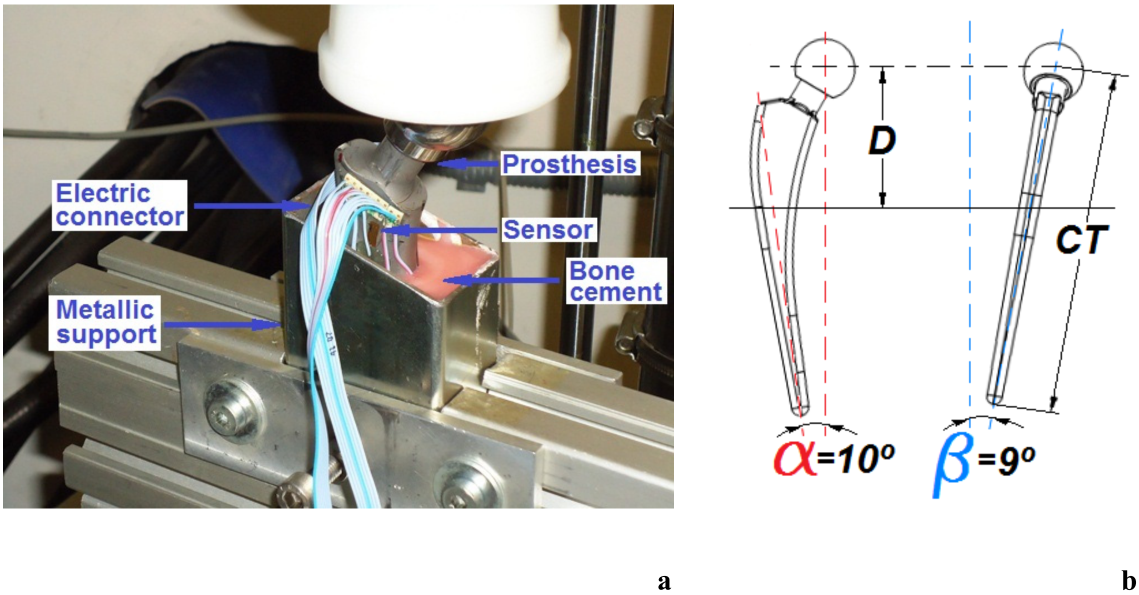

Figure 3.1 - a) Image of the hip-joint prosthesis in the stress-strain experimental setup, and b) inclination angles α and β of the axis of the prosthesis

Mechanical fatigue test were performed in the compressive mode, according to standard ISO 7206 [14]. The typical fatigue test consists on the fitting of the prostheses to a 60% of the CT length (distance between the lower end of the prostheses to the geometrical center of the head) within the mold with inclination angles α (10º ±1) and β (9º ±1) of the axis of the prosthesis with respect to the front and lateral sides of the mold cavity (figure 3.1). With respect to the testing conditions, a maximum load was applied to the material and then a dynamical load was applied from a minimum load of 10 % of the maximum load up to the maximum load, during 10,000 cycles. Experimental data were recorded at 0.5 Hz, 1 Hz and 5 Hz. The mechanical conditions applied in the experiments performed in the hip-joint prosthesis are summarized in table 3.1 and a schematic view of experimental setup is presented in figure 3.1.

Finally a burst test was performed to the hip-joint prosthesis in the compression mode, at a velocity of dl/dt = 2 mm/min.

Table 3.1 - Mechanical experimental conditions applied to the hip-joint prosthesis

Dynamic tests 10000 cycles	130N to 1300N at 1Hz
	230N to 2300N at 1Hz
	400N to 4000N at 1Hz
	230N to 2300N at 0.5Hz
	230N to 2300N at 5Hz

A data acquisition electronic circuit and software were implemented in order to record the signals from the sensors. The block diagram of the acquisition setup is shown in figure 3.2.

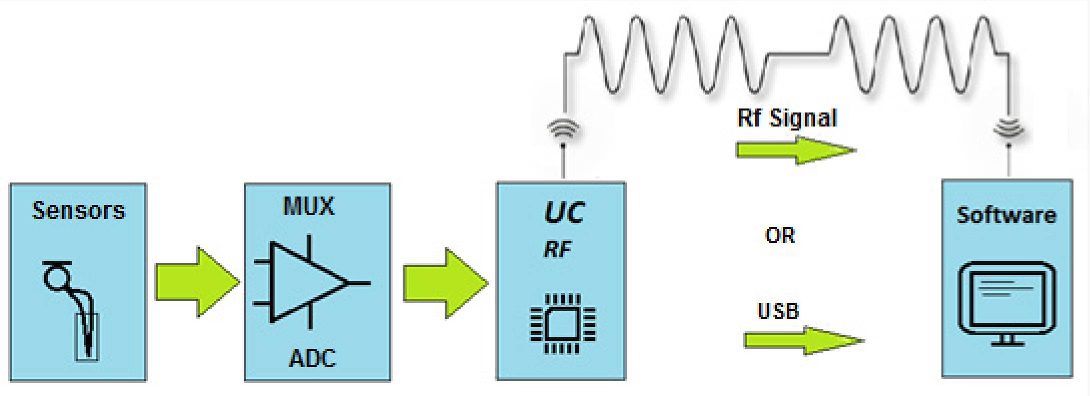

Figure 3.2 - Block diagram of the electronic signal acquisition and recording of the output sensors signal.

Briefly, the sensors were connected to an analog multiplexer (MUX) that performs the switching between the different sensors. The voltage variation generated by the deformation of the selected sensor under mechanical solicitation is amplified, converted to digital (ADC) and acquired by the microcontroller (UC). The microcontroller sends the data to the computer either by a wired, universal serial bus (USB) or by a wireless (RF) link.

Finite element software in a 3D space was used with the mechanical stress-strain module to calculate the stress and strain in the 3D hip prosthesis model under the same loading conditions in which the experimental tests were performed, following the ISO 7206 standard. The parameters used to simulate the mechanical performance of the prosthesis are summarized in table 3.2.

Results and Discussion

Table 3.2 - Material properties of the hip prosthesis model.

Property	**Steel AISI 316L**	**Polyamide (M2)**	**Bone cement**
Young's modules	205×10^{9} [Pa]	3×10^{9} [Pa]	18×10^{9} [Pa]
Poisson's ratio	0.28	0.35	0.40
Density	7850 [kg/m^3]	1350 [kg/m^3]	1500 [kg/m^3]
Thermal expansion	1.23×10^{-5} [1/K]	1.20×10^{-5} [1/K]	1.20×10^{-5} [1/K]

3.3. Results and Discussion

Computer simulations were performed in order to characterize the stress distribution along the artificial prosthetic device. Figure 3.3 shows the simulation results, where it is possible to observe that the positions submitted to higher mechanical effort are the ones placed at the bone cement interface. Then, the piezoresistive sensors (S4, S21, S1, S3, S22 and S2) were attached to the hip-joint prosthesis at the places indicated in figure 3.3 and corresponding to different stress levels.

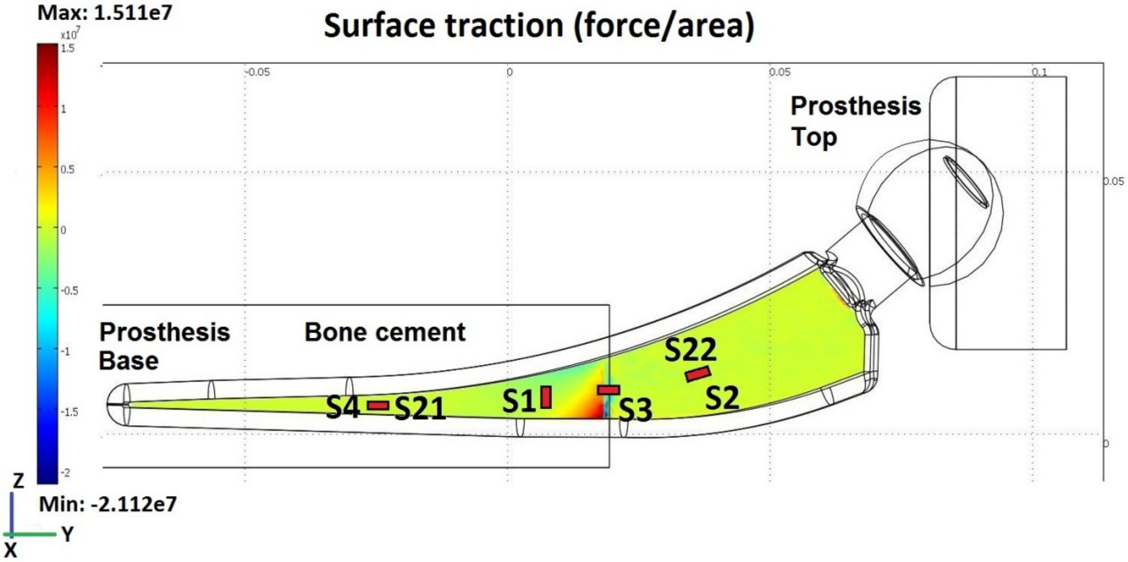

Figure 3.3 - Simulated stress distribution for the hip-joint prosthesis with solicitation along y. The horizontal rectangle indicates the placement of the cement.

The positions S4 up to S2 correspond to the pairs of sites (one on each side of the implant) where commercial strain gauges and the thin-film Si gauges fabricated in this work were placed, on opposite sides of the implant, which is shown here (figure 3.3) along his main symmetry plane.

The hip-joint was then fixed to the universal testing machine according to the ISO 7602 standard, to carry out the cyclical mechanical loading tests. The obtained results for the piezoresistive sensors at different testing frequencies are reported in figure 3.4. The piezoresistive signal of the commercial sensors follows the mechanical excitation and the electrical response is stronger for the sensors outside the cement fixation (sensor S2) which is closer to the jaw that transmits the mechanical stimulus. For the sensor embedded inside the bone cement (S4) a similar result as the one found for sensor S1 was observed, which reveals that the mechanical stress is distributed uniformly along the hip-joint prosthesis. The piezoresistive sensor placed in the bone cement boundary has the weakest electrical signal due to the damping that occurs between the implant, the bone cement and the open air, decreasing the amplitude of the electrical response of the sensor. Moreover, it was observed that the amplitude of the electrical signal acquired for each single commercial sensor increases with increasing applied frequency to the hip-joint prosthesis. A phase lag between the mechanical stimulus and the electrical signals around 10º was observed, in particular for sensors S3 and S4. This fact is to be attributed to the mechanical experimental setup, as the hip-joint prosthesis is placed, after the norm ISO 7206, with the specific inclination (angles α and β) shown in figure 3.1, promoting shear-stress contributions detected by the electrical measurement as phase lag between the mechanical stimulation and the electrical reading (figure 3.4a). The obtained results of the amplitude for the electrical signal of the commercial strain gauges at 0.5 and 1 Hz are very similar.

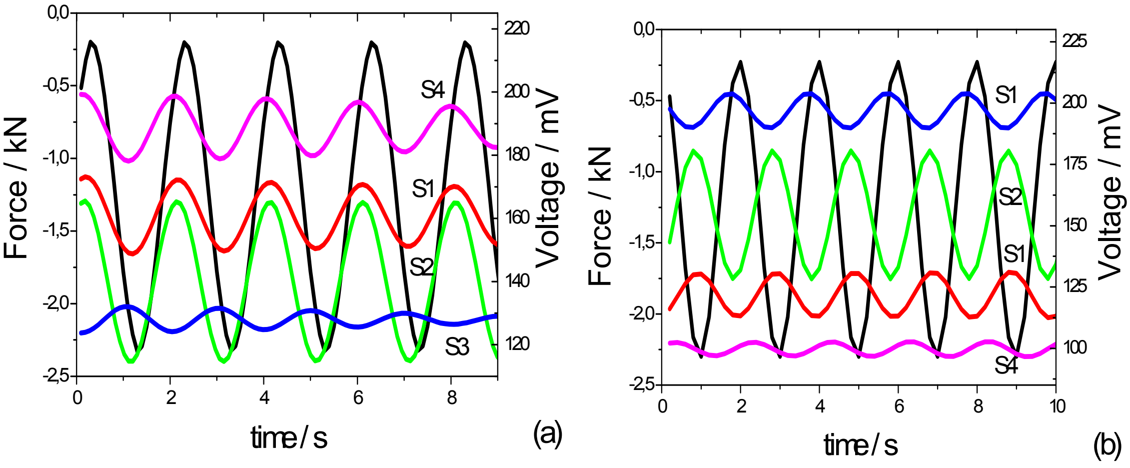

Figure 3.4 - Piezoresistive response for the commercial metallic sensors performed with a maximum force of 2300 N and: a) 0.5 Hz, b) 5 Hz.

Moreover, at 5 Hz, the amplitude of the electrical signal of sensors S1 and S2 (inside and outside the bone cement, respectively) remains unchanged, with the same phase lag that was observed at 1 Hz. For the sensor at the boundary region (S3), an increase of the electrical amplitude was observed, with a slight phase lag compared to the mechanical excitation. On the other hand, the sensor in the base of the prosthesis (S4) presents a decrease of the electrical signal and also a phase lag, which leads to conclude that the commercial metallic piezoresistive sensors have some offset relatively to the mechanical stimulus for frequencies above 0.5 Hz (figure 3.4).

The influence of applied force on the electrical response for the commercial strain gauge sensors was characterized. Two different measurements were carried out at a maximum force of 1300 N and at 4000 N (the minimum force, according to the ASTM standard is 10 % of the maximum applied force) and a frequency of 1 Hz (figure 3.5).

For lower mechanical applied force, the amplitude of the electrical signal is quite similar for all metallic sensors and a phase lag of about 180º was observed, independently of the sensors position along the hip-joint prosthesis (figure 3.5a).

For the higher mechanical load and at 1 Hz (figure 3.5b), sensor S2 has the largest electrical signal amplitude, showing that the hip joint-prosthesis region immediately below the femoral cup is more exposed to the mechanical solicitation. Also, sensor S1, placed in a region covered by bone cement, has a high electrical signal amplitude, but smaller when compared to sensor S2. In a different part of the prosthesis, sensor S4, the amplitude of the electrical signal decreases as compares to S1 and S1, which reveals that the mechanical load distribution pattern along the hip-joint prosthesis is dependent on the value of the mechanical load.

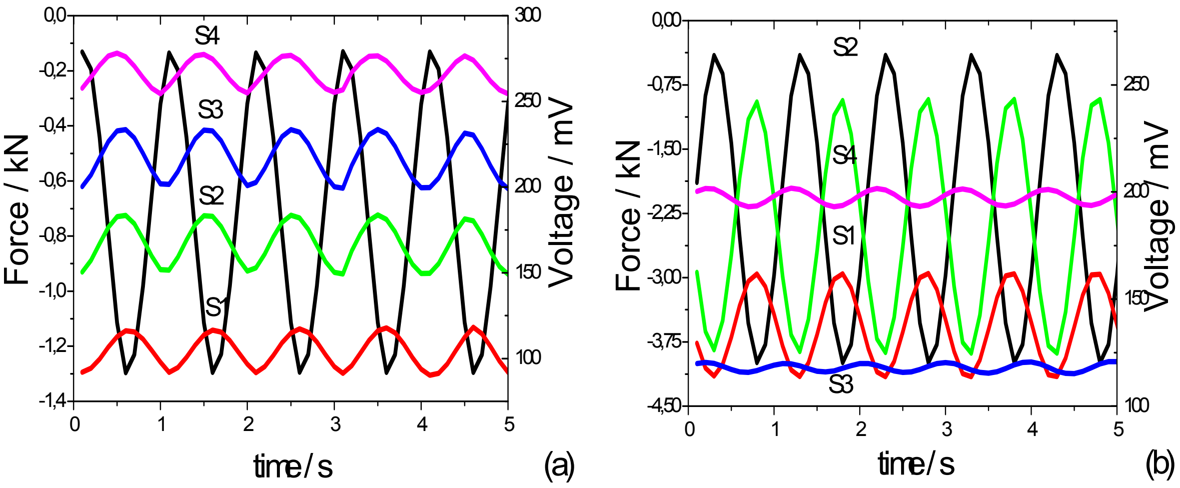

Figure 3.5 - Piezoresistive response for the commercial metallic sensors performed with at 1 Hz for: a) 1300 N and b) 4000 N.

For the higher mechanical load and at 1 Hz (figure 3.5b), sensor S2 has the largest electrical signal amplitude, showing that the hip joint-prosthesis region immediately below the femoral cup is more exposed to the mechanical solicitation. Also, sensor S1, placed in a region covered by bone cement, has a high electrical signal amplitude, but smaller when compared to sensor S2. In a different part of the prosthesis, sensor S4, the amplitude of the electrical signal decreases as compares to S1 and S1, which reveals

that the mechanical load distribution pattern along the hip-joint prosthesis is dependent on the value of the mechanical load.

The sensor at the base of the prosthesis (S4) shows electrical response amplitude smaller than the previous ones, and a phase lag to sensor S2 and S1 is observed. The phase lag of the electrical response of the sensor relative to the mechanical solicitation is of approximately 10º. The sensor at the boundary region between the bone cement and the open-air, reveals poor electrical response revealing that a damping effect and release of the mechanical energy occurs in this region. This effect was observed for the prosthesis tested at different frequencies (figure 3.4).

Besides the commercial sensors, two n-type piezoresistive nc-Si:H microresistors with thickness around 120 nm, fabricated on 125 μm polyimide polymer substrates (a picture of the sensor can be seen in [12] were mounted in the hip-joint prosthesis at exactly the same position as the metallic commercial strain gauges, but at the other side of the prosthesis. The evolution of the electrical signal of the piezoresistive nc-Si:H sensor was registered and compare to the signal of the commercial gauges.

P-doped thin-film silicon piezoresistive sensors show an electric signal output higher than the metallic commercial ones (figure 3.6), when subject to the same experimental conditions. The electrical response of the sensor placed inside of the bone cement shows output voltage amplitude around 200 mV, which is quite high when compared to the 20 mV (figure 3.4a) of voltage output amplitude obtained for the commercial sensors placed in the same position. For 0.5 Hz experiment, it was observed a phase lag of almost 180 º between the applied mechanical stress and the output electrical signal for the sensor placed inside the bone cement, but the sensor placed outside shows a good matching between the mechanical loading and the electrical signal (figure 3.6a).

By increasing the applied mechanical frequency, the phase lag of the micro resistor placed inside the bone cement decreases and for the experiment performed at 5 Hz, no phase lag between the mechanical loading and the electrical voltage output was detected (figures 3.6 b and c). On the other hand, the sensor placed outside the bone cement showed an opposite response of the electrical output voltage. It was observed that with increasing applied mechanical load frequency, the phase lag between the mechanical loading and the electrical output voltage increases (figure 3.6 b and c). At 5 Hz, this sensor shows a small electrical response, but as it can be observed in figure 3.6d), the output voltage still allows evaluating the mechanical load.

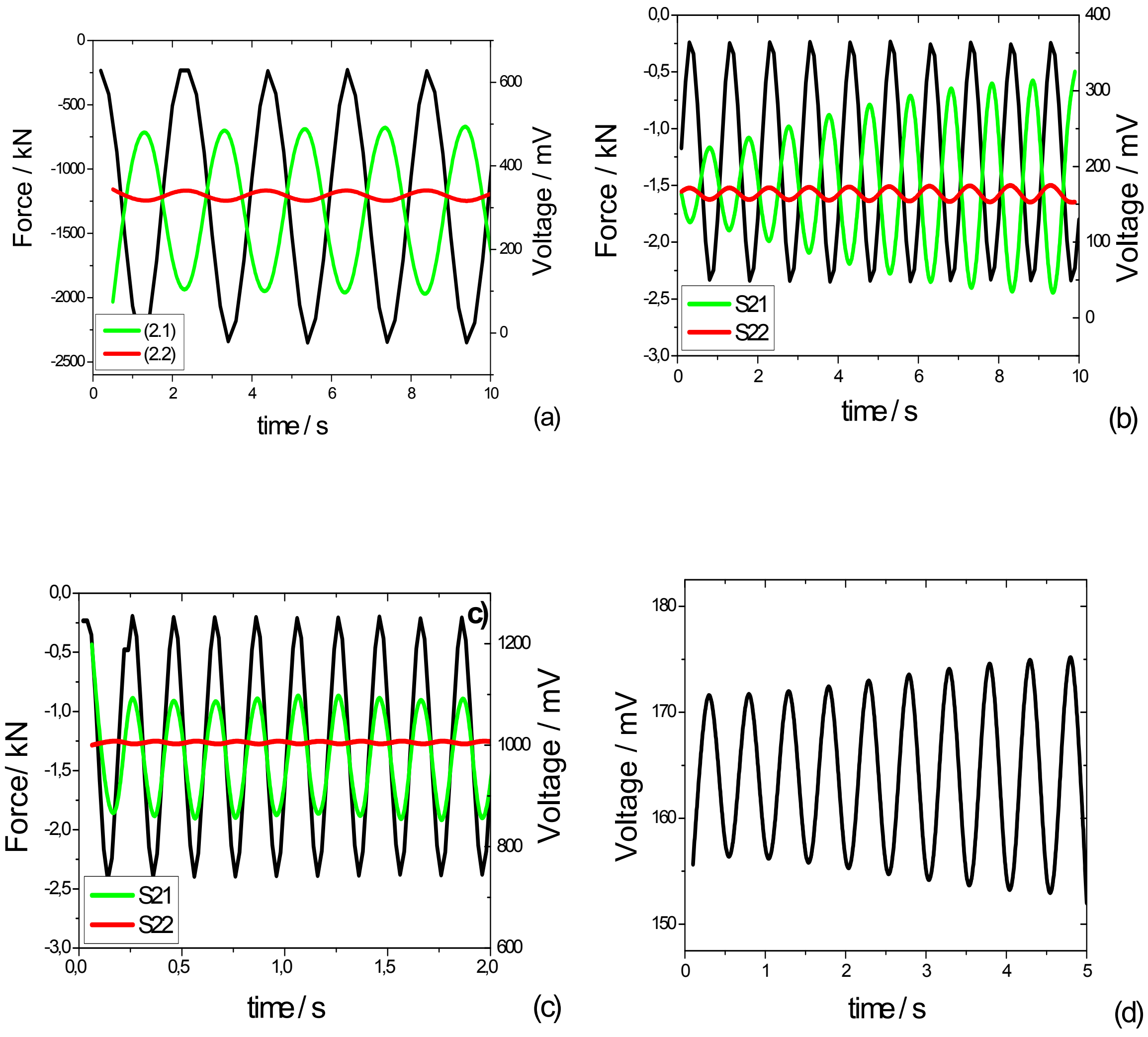

Figure 3.6 - Piezoresistive measurement for the ni-S:H microresistor performed with a maximum force of 2300 N and: a) 0.5 Hz, b) 1 Hz, c) 5 Hz and d) detail of the electrical output of sensor S22 of figure c.

In order to have a better understanding of the nc-S:H microresistor (R_x) response, the Gauge factor (GF) was determined taking into account the characteristics of the implemented electronic circuit (figure 3.7).

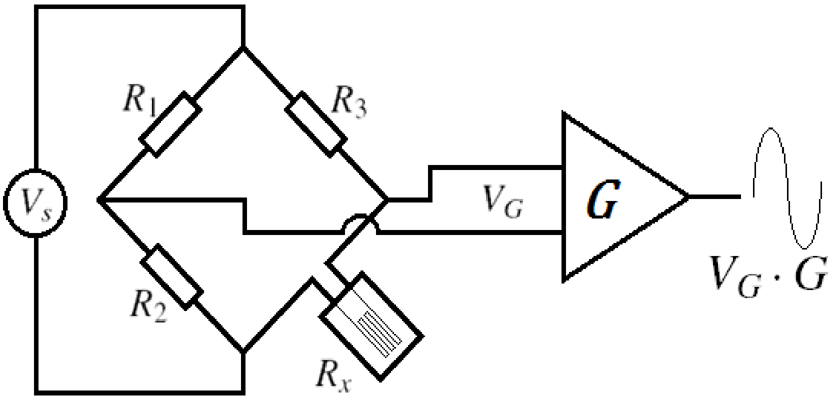

Figure 3.7 - Electrical circuit used to obtain the value of the sensor resistance (Rx).

For R1=R2=R3, the change in resistance of the sensor is given by:

$$\Delta R = \frac{4R_x\left(\frac{\Delta V_G}{V_s}\right)}{1-2\left(\frac{\Delta V_G}{V_s}\right)}$$

(eq. 3.1)

By replacing the known parameters of the electrical circuit of figure 3.7, the resistance changes of the piezoresisitive sensors are shown in table 3.3.

Table 3.3 - Resistance variation for the commercial (S2, S4) and ni-S:H (S22, S21) piezoresistive sensors, when the prosthesis is subject to 4000 N and 2300 N.

Sensor	**R without deformation**	**ΔR at 4000N**	**ΔR at 2300N**
S2	120 Ω	0.118 Ω	0.0306 Ω
S4	120 Ω	0.042 Ω	0.0334 Ω
S22	10.16 K Ω	12.0 Ω	3.24 Ω
S21	10.02 K Ω	41.1 Ω	32.6Ω

It is assumed a GF value of 2 for the commercial metallic strain gauges, and that, due to the fact that the nc-S:H microresistor were placed at similar positions, they were submitted to the same mechanical strain (ε) so with the substitution of commercial metallic strain gauge parameters in the equation 3.1 it is possible to calculate the strain for nc-S:H microresistor. From equation 3.2, the Gauge Factor of the nc-S:H microresistor are calculated (table 3.4).

$$GF = \frac{\Delta R/R_0}{\varepsilon}$$

(eq. 3.2)

Table 3.4 - Gauge Factor obtained for the nc-S:H piezoresistive sensors.

GF	4000N	2300N
S22	-2.4	-2.5
S21	-23.4	-23.4

The GF obtained values for the nc-S:H piezoresistive sensors were around 2.4 for the sensor placed outside the bone cement and -23.4 for the piezoresitor encapsulated within the bone cement. These results are lower than the ones obtained previously, under 4-point bending loading cycles , for the same piezoresistive sensors, which showed a GF of -28.1 [12]. The difference can be explained by the fact that all the manipulation needed to fix the sensors to the prosthesis somehow damaged them. It is necessary to point out that, contrary to the commercial sensors, the nc-Si:H sensors fabricated in this work had no encapsulation.

3.4. Conclusions

The monitoring of mechanical stress over time in prosthesis is reported in this work. Silicon thin-film piezoresistive sensors were developed, attached to a prostheses and their results compared with commercial strain gauge sensors. Mechanical stress-strain experiments in compressive mode show that the thin-film silicon piezoresistive sensors are much more sensitive than the commercial ones due to their higher gauge factors (-23.5), when compared to the gauge factors of commercial sensors (2).

3.5. References

[1] J. B. Park, "Hip Joint Prosthesis Fixation-problems and Possible Solutions: Second Edition," in *The Biomedical Engineering Handbook*, J. D. Bronzino, Ed., ed Boca Raton: CRC Press LLC, 2000.

[2] C. Fu-Chai, H. Jui-Ping, and L. Yuan-Lung, "Finite Element Analysis on the Mechanical Effect of a Roughened Stem for Cemented Hip Prosthesis," in *Computer Science and Information Engineering, 2009 WRI World Congress on*, 2009, pp. 254-258.

[3] Sumit Pramanik, Avinash Kumar Agarwal, and K. N. Rai, "Chronology of Total Hip Joint Replacement and Materials Development," *Trends Biomaterials and Artifical Organs,* vol. 19, pp. 15-26, 2005.

[4] M. Semlitsch and H. Willert, "Properties of implant alloys for artificial hip joints," *Medical and Biological Engineering and Computing,* vol. 18, pp. 511-520, 1980.

[5] L. Cristofolini, A. Marchetti, A. Cappello, and M. Viceconti, "A novel transducer for the measurement of cement–prosthesis interface forces in cemented orthopaedic devices," *Medical Engineering & Physics,* vol. 22, pp. 493-501, 2000.

[6] D. L. Glos, F. E. Sauser, I. Papautsky, and D. I. Bylski-Austrow, "Implantable MEMS compressive stress sensors: Design, fabrication and calibration with application to the disc annulus," *Journal of biomechanics,* vol. 43, pp. 2244-2248, 2010.

[7] U. Marschner, H. Grätz, B. Jettkant, D. Ruwisch, G. Woldt, W. J. Fischer, and B. Clasbrummel, "Integration of a wireless lock-in measurement of hip prosthesis vibrations for loosening detection," *Sensors and Actuators A: Physical,* vol. 156, pp. 145-154, 2009.

[8] C. Ruther, H. Ewald, W. Mittelmeier, A. Fritsche, R. Bader, and D. Kluess, "A Novel Sensor Concept for Optimization of Loosening Diagnostics in Total Hip Replacement," *Journal of Biomechanical Engineering,* vol. 133, pp. 104503-5, 2011.

[9] H.-Y. Zhang, L. Brown, S. Barrans, L. Blunt, and X.-Q. Jiang, "Investigation of relative micromotion at the stem—cement interface in total hip replacement," *Proceedings of the Institution of Mechanical Engineers, Part H: Journal of Engineering in Medicine,* vol. 223, pp. 955-964, November 1, 2009 2009.

[10] D. W. Bühler, T. R. Oxland, and L. P. Nolte, "Design and evaluation of a device for measuring three-dimensional micromotions of press-fit femoral stem prostheses," *Medical Engineering & Physics,* vol. 19, pp. 187-199, 1997.

[11] M. M. Jevtić and M. A. Smiljanić, "Diagnostic of silicon piezoresistive pressure sensors by low frequency noise measurements," *Sensors and Actuators A: Physical,* vol. 144, pp. 267-274, 2008.

[12] P. Alpuim, V. Correia, E. S. Marins, J. G. Rocha, I. G. Trindade, and S. Lanceros-Mendez, "Piezoresistive silicon thin film sensor array for biomedical applications," *Thin Solid Films,* vol. 519, pp. 4574-4577, 2011.

[13] ISO, "Implants for surgery -- Partial and total hip joint prostheses," vol. 7206, ed: International Organization for Stardardization 2010.

[14] P. Alpuim, E. S. Marins, P. F. Rocha, I. G. Trindade, M. A. Carvalho, and S. Lanceros-Mendez, "Ultra-sensitive shape sensor test structures based on piezoresistive doped nanocrystalline silicon," *Vacuum,* vol. 83, pp. 1279-1282, 2009.

[15] RS-Components. (2011). Available: http://uk.rs-online.com/web/p/strain-gauges/0632168/

4. Development of inkjet printed strain sensors

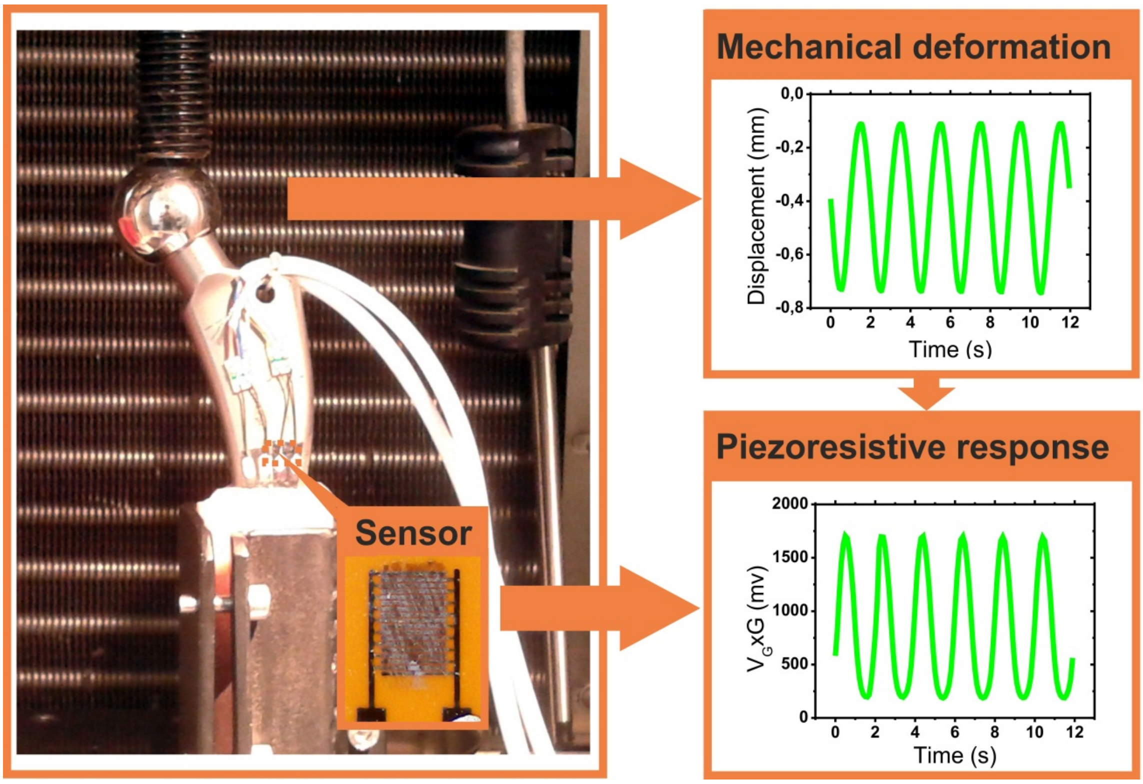

This chapter is based on the following publication: V. Correia, C. Caparros, C. Casellas, L. Francesch, J. G. Rocha, and S. Lanceros-Mendez. *Development of inkjet printed strain sensors*. Submitted to Applied Materials and Interfaces, 2013.

4.1. Introduction

There is an increasing interest in using the techniques of graphic industry for the production of flexible electronics and sensors due to its reduced cost and large production areas [1], [2], which allows mass production of radio frequency identification (RFID) tags, flexible antennas and sensors [3], [4], among others.

Flexible sensors is an increasing area of research and development due to the growing demand of biosensors, artificial skins, chemical sensors, force and deformation sensor, among others. The common methods currently used for the fabrication of these type of sensors are vacuum deposition, photolithography and spin-coating [5–7] but these methods present show some drawbacks for these applications, as there were mainly developed for production of microelectronics involving multiple fabrication steps, high processing temperatures and produce toxic waste [8] for a single layer production.

In this way, direct printing techniques such as screen printing and ink jet printing have received increasing attention for the implementation of sensors [9]. Screen printing is widely used for industrial production when it is not necessary large resolution and therefore there is no need of precise matching in the case of multi-layer fabrication. Further, this fabrication technique requires the use of masks for each printed layer.

On the contrary, inkjet printing does not require masks for the production of different layers, allowing a more versatile process. Further, it is a non-contact method with the large advantage of reduced contamination and risk of substrate damage [10–12]. The later issue is particularly important in the case of the production of biosensors and chemical sensors.

Inkjet printing allows precise control of the layer thickness and the quantity of applied ink, which allows to obtain printed areas according to specific requirements, this being a critical factor for the fabrication of flexible electronic circuits and sensors [13], [14], in order to allow the required performance, but also for granting reproducibility of the impression for large scale production demands.

Force and deformation sensors are among the most required ones for a set of applications ranging from biomedical [15] to automotive [16], [17], among many others. One of the most used physical mechanism for this type of measurements is based on the piezoresistive (PR) effect. Polymer based materials with large deformation sensitivity have been recently developed based on conductive polymers [18] or polymer composites [19] based on polymer elastomers [20], thermoplastics [20] or epoxies [21], which allow to use polymer instead of the more conventional strain gages [22] for these type of measurements. Further, polymer based sensors allow the use of conventional polymer processing techniques, including printing technologies such as ink jet printing.

The development of PR sensors using printing techniques is therefore taking the firsts steps due to its large potential.

Typical PR sensors are silicon based and fabricated on wafers which are subsequently divided and integrated with all necessary microelectronic for signal manipulation [23, 24]. However, this technique does not allow to obtain flexible sensors for large areas and therefore hinders direct integration into some devices, so new sensors were developed using deposition techniques [15].

With this in mind, this paper reports on the design, fabrication and test of printed strain sensors. Various types of strain printed sensors were developed and characterized. A matrix and an array of sensors were also be printed and tested. The developed sensors were applied to a hip prosthesis and the performance tests conducted according to ISO normalized procedures [25].

4.2. Experimental details

4.2.1. Inkjet printed and inks

Inkjet printing of the sensors was performed using a Fujifilm Dimatix DMP 2831 with a DMC-11610 [26] (propylene; silane/SiO2) cartridge with 16 nozzles at 254 µm spacing. The drop volume was 10 picoliters and the capacity of ink per cartridge was 1.5 ml.

The Dimatix Printer (DMP) allows defining a large set of parameters such as cartridge temperature, substrate temperature, gains of nozzles voltage and frequencies of the nozzles in order to optimize printing according to the substrate, ink and application.

Several inks were used for the development of the sensors: the conductive layer used for printing a Strain Gauge (SG) sensor, the interdigitated structures and the electrical connections was based on a commercial conductive silver particle based ink (Sunchemical). The piezoresistive active layers were developed with two types of inks: a Organo PeDOT containing solution (Agfa) and a ink based on TIPS-Pentacene (716006, Sigma Aldrich) prepared using 22 mg of TIPS-Pentacene mechanically mixed in 2 mL of 1,2-dichlorobenzene for 30 min.

For the printing of the matrix structures an insulating ink based on PVPh (Polyvinylphenol) was also used to avoid the short circuit of rows and columns.

Sensors were developed on a KAPTON substrate with a thickness of 75 µm, due to its temperature resistance.

After printing a particular layer it was necessary to cure the respective printed ink with specific optimized curing condition. the curing condition for the silver ink were 150 ºC for 40 min; 130 ºC for 15 min for the PeDot ink and 120 ºC for 5 min for the case of TIPS-pentacene ink. The insulated ink was cured at 150ºC for 30 min.

4.2.2. Electrical conductivity measurement

The d.c. electrical resistance of the single sensors was measured at room temperature with an Agilent 34401A digital multimeter with 6 ½ digits resolution. The multimeter was connecter directly to the silver printed connection paths with dimension of 0.8 mm x 0.4 mm.

This measurement allowed the characterization of the sensor with no deformation, i.e., the resistance value indicated as R_0. In the case of the sensor array and matrix structures it was necessary to develop an electronic circuit to allow the measurement of 20 sensors simultaneously. Therefore, the sensors were integrated into a Wheatstone bridge and the resulting differential voltage (V_G) variation was amplified by an instrumentation amplifier (G), as shown in figure 4.1.

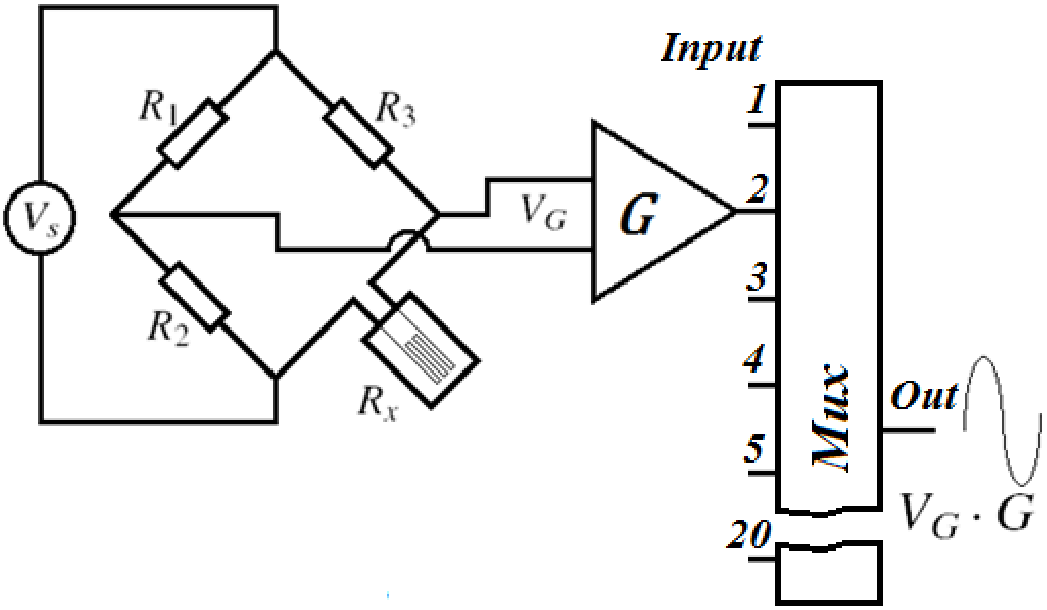

Figure 4.1 - Electrical circuit used to obtain the value of the multi-sensor resistance (R_x). Here R_1 to R_3 are the resistances of the bridge, V_S is the voltage supply, V_G is the differential voltage between the bridge terminals, G is the gain of the amplifier and Out is the output voltage corresponding to $V_G * G$.

Considering all the parameters of the circuit and for $R_1=R_2=R_3=R_{x0}$ which corresponds to balanced bridge, the resistance variation of the R_x sensor (ΔR_x) is given by:

$$\Delta R_x = \frac{4R_{x0}\left(\frac{\Delta V_G}{V_s}\right)}{1-2\left(\frac{\Delta V_G}{V_S}\right)}$$

(eq. 4.1)

where, R_{x0} is the sensor resistance, ΔV_G is the voltage variation of the bridge terminals and V_S is the bridge power supply.

4.2.3. Electro-mechanical characterization

The sensitivity of a PR sensor to a given deformation can be quantified by the gauge factor, *GF*, which represents the relative change in electrical resistance due to mechanical deformation:

$$GF = \frac{\left(\frac{\Delta R}{R_0}\right)}{\left(\frac{\Delta l}{l_0}\right)}$$

(eq. 4.2)

In this equation, R_0 is the steady-state material electrical resistance before deformation and ΔR is the resistance change caused by the variation in length Δl [21]. The resistance change under strain results from the contribution of the dimensional change a geometrical effect (ΔR_D) and from the intrinsic PR effect (ΔR_l) (equation 4.3). Therefore, for the surface mode measured used in the present investigation (figure 4.2), the *GF* can be written as [21]:

$$GF = \frac{\left(\frac{\Delta R}{R_0}\right)}{\varepsilon_l} = \Delta R_D + \Delta R_l = 1 + \upsilon + \frac{\left(\frac{\Delta \rho}{\rho}\right)}{\varepsilon_l}$$

(eq. 4.3)

where, $dl/l=\varepsilon_l$ and υ is the Poisson ratio.

The experiments were performed in mechanical 4-point-bending mode using a Shimadzu-AG-IS universal testing machine. Figure 4.2 presents a schematics of the 4-point bending set-up.

Assuming pure bending of a plate to a cylindrical surface, the strain (ε) between the inner loading points can be calculated from [21]:

$$\varepsilon = \frac{3dZ}{5a^2}$$

(eq. 4.4)

Where *Z* is the vertical displacement of the piston, *d* is the sample thickness and *a* is the distance between the two bending points.

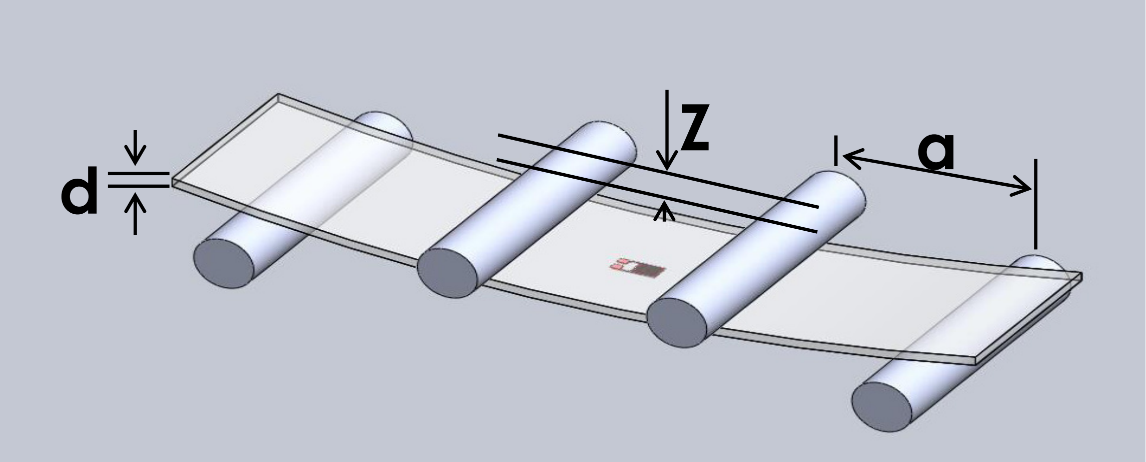

Figure 4.2 - Schematics of the 4-point bending test used for the electromechanical evaluation of the sensors. z is the vertical displacement of the piston, d is the sample thickness and a is the distance between the two bending points. The sensors are placed at the bottom surface of the substrate.

Electromechanical tests consisted in several loading/unloading cycles at room temperature, with a test speed and *Z* displacement defined according to the dimensional characteristics of the sensors, while recording at the same time the electrical resistance variation. The *GF* was calculated for each cycle from the z-displacement and the electrical resistance curves by taking the best fit curve by linear regression. Finally, the average *GF* value was calculated for each sample. The value of the *GF* for the loading and unloading mechanical cycles at a given set of conditions was the same, unless indicated.

4.3. Results and discussion

4.3.1. Single sensor development

4.3.1.1. Printing and optimization of the conductive layer

Printing of a conductive layer is required both for the development of the SG sensors, which are composed uniquely by one conductive layer, and for the interdigitated electrodes, as the conductive layer serves as electrodes for the remaining sensors. During this process it was necessary to optimize printing conditions.

The desired pattern of the SG sensor is shown in figure 4.3a). It was designed for a drop space of 20 µm in order to obtain the lowest possible dimension for the sensors considering that the drop diameter of the silver ink is 42µm. The final dimension of sensor active area was 2.5 mm x 1.75 mm (figure 4.3).

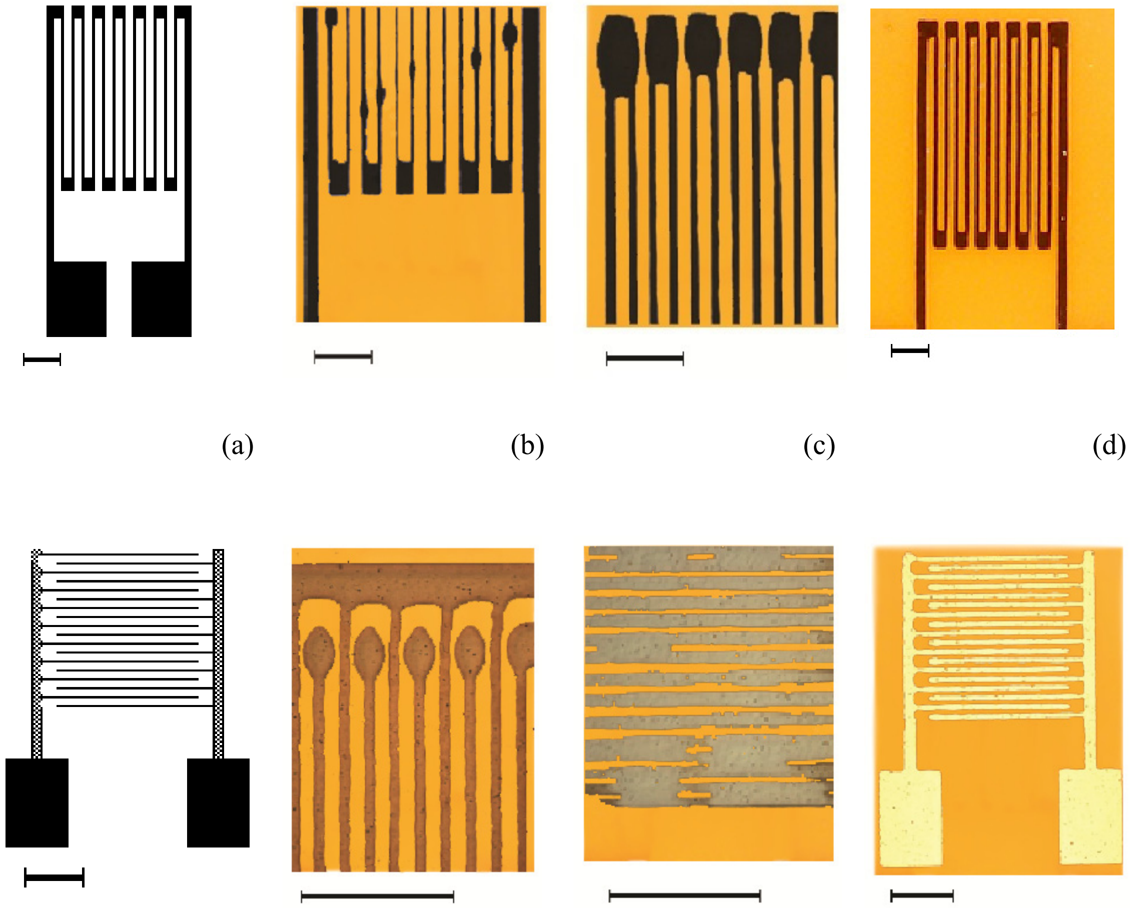

(a) (b) (c) (d)

(e) (f) (g) (h)

Figure 4.3 – a) Projected pattern for Strain gauge sensor, b) defects at the middle of the printed lines, c) defects at the end of the printed lines, d) final result of strain gauge sensor, e) Desired pattern for the interdigitated conductive layer for piezoresistive sensors, f) excess of material at the end of the lines, g) short-circuit between the lines and h) final result of the interdigitated printed pattern. All bar scales correspond to 0.5 mm.

Initial tests showed an excess of material at the middle (figure 4.3b) and the end (figure 4.3c) of the lines. These errors were corrected by removing pixels in areas of excess at the end of the line tracks (figure 4.3c) and by printing in a horizontal configuration instead of the vertical one. In this printing configuration, the pattern is performed line by line along the horizontal axis and lines without excess of material are obtained (figure 4.3d).

For interdigitated structures (figure 4.3e, f, g and h) the main objective for miniaturization is to reduce as much as possible the spaces between the lines of the interdigitated fingers without creating a short-circuit. The desired pattern of the interdigitated layer is shown in figure 3e, which is also designed for a drop space of 20μm.

Figures 4.3f) and 4.3g) show intermediate steps in the optimization process showing the most common defects: excess of material and short-circuit between lines. Figure 4.3h shows the final printed interdigitated structure with a distance between the lines of the fingers of 30 μm and a sensor active dimension of 1.8 mm x 1.5 mm, which is one of the best results reported in the literature in terms of miniaturization with inkjet printing technologies. The average electrical resistance of the sensors was 830 Ohm.

4.3.1.2. Printing and optimization of the PeDOT and the TIPS-Pentacene layer

The piezoresistive sensors are composed by the interdigitated silver layer mentioned before and a polymer layer on top of this layer. The pattern of the top layer just consists on a homogeneous layer on top of the interdigitated fingers. Despite the apparent simplicity of this layer, problems can also arise with respect to homogeneity of the layer due to the 3D pattern of the conductive silver layer on the top layer (figure 4.4a).

This problem has to be solved by adding several layers of the active polymer material in order to overcome the dimensional effect of the pattern of the previously printed materials. The printing process involved therefore heating the substrate at a temperature of 50 ºC in order to accelerate the curing process and to allow a rapid deposition of the different layers. The homogeneous surface of PeDOT was achieved after the deposition of six layers, producing a final thickness of ~ 18 μm. The result is shown in figure 4.4b). The average resistance of the sensors was 1.42 KOhm.

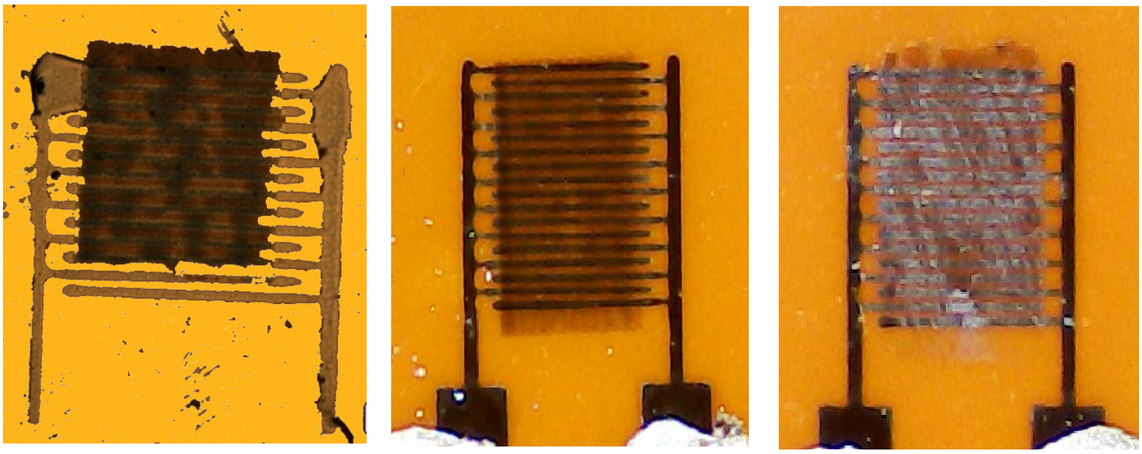

(a) (b) (c)

Figure 4.4 – a) Representation of the homogeneity problems arising with the deposition of the PeDOT layer, b) final PR sensor based on PeDOT and c) semiconductor sensor based on TIPS-Pentacene.

In the case of the sensor based on TIPS-Pentacene, the same problems were found as with PeDOT and similar solutions were used. In this case, just three layers of TIPS-Pentacene were required to form a homogeneous layer of material with a final thickness of 12 μm (figure 4.4c). For these sensors, the average resistance was 100 KOhm.

4.3.2. Single sensor characterization

Electrical and electromechanical characterization of the sensors was carried out in order to assess the characteristics and performance of the development of single and multi sensor structures. Due to the better performance of the sensors and the similarity of the printing and testing procedures, the following sections will be concentrated in the strain gauges and the piezoresistive sensors based on PeDOT.

4.3.2.1. Strain Gauge based on printed silver ink

Four-point bending tests were performed for the inkjet printed silver ink SG, which showed an average resistance of 830 Ohm. Five cycles were applied to the sensors with a deformation of 0.5 mm at a speed of 0.5 mm/min at room temperature and the distance between the two bending points (figure 4.2) is 15 mm.

Figure 4.5a) shows a typical example of the data obtained from the strain tests performed for the SG sensors with simultaneous measurement of electrical resistance. It was verified that all sensors show a linear response with the resistance variation following the applied deformation. The overall electrical response slightly decreases with increasing number of cycles due to mechanical relaxation of the material, the material recovering the initial resistance when the deformation is definitively resealed [18].

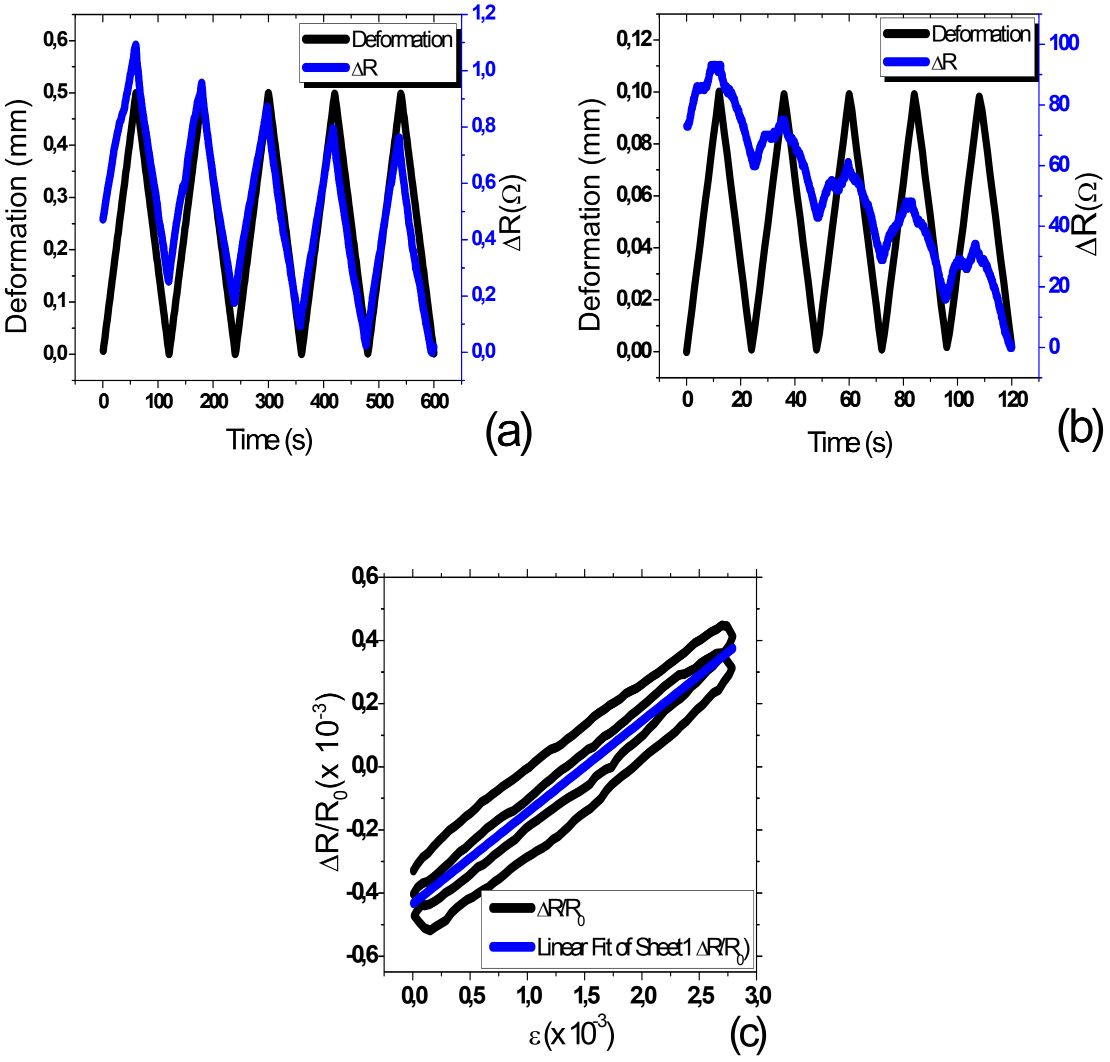

Figure 4.5 – a) Representative cyclic deformation applied to a sample of strain gauge b) PR sensor with the corresponding resistance variation as a function of time and c) relative change in electrical resistance due to mechanical deformation, for several up-down cycles applied to a sample.

The GF was calculated by applying equation 4.2 to the measured data and fitting with a linear regression as shown in figure 4.5c). The typical value for the GF of SG printed sensors is around 0.35 ±2%. This value is the same, within experimental error, for the up and down cycles and for the different cycles. The obtained value of the GF indicates that the response of the sensor is completely to be ascribed, as expected, to the geometrical variation of the sensors [18], [19].

4.3.2.2. Piezoresistive sensor composed by interdigitated silver electrodes and a PeDOT layer

Four-point bending experiments with simultaneous measurement of the electrical variations were performed in the PR sensor with PeDOT layer. These sensors had an average electrical resistance of 1.42 KOhm. The maximum applied deformation was 0.1 mm at a deformation speed of 0.5 mm/min at room temperature. A typical example of the results is presented in figure 4.5b). The small deformation in this case is due to the strong sensibility of the sensors and the presence of nonlinear phenomena for larger deformations. For this sensor, it is also observed reproducibility in the form of the response and in the values of the variation of the resistance with the applied deformation, but a decrease of the overall value of the resistance with increasing number of cycles. This variation is due to residual strains and stresses remaining in the material during the dynamic solicitation [19], as the material recovers the initial resistance when the deformation is resealed. In any case the small variation of the overall resistance (approximately 100 Ohm) together with the reproducibility of the resistance variation for the several cycles makes these sensors suitable for applications. Further, the sensors show a GF of ~2.48 ± 2,6%, as calculated after equation 4.2 with a procedure similar to the one shown in figure 4.5c). The values of the GF indicates the contribution of the intrinsic piezoelectric effect of the polymer layer over the geometrical factors [27].

The GF of the materials and therefore their sensitivity as sensors can be further tuned by varying processing conditions. For examples, GF between up to 40 can be obtained by applying o pre-cure time at 50 ºC for 30 min instead of 74 min. In any case, as reduced pre-cure time can affect the long time stability of the sensors, this effect is still under investigation.

4.3.3. Sensor array and matrix developed

The array design was based on the results obtained for single printed sensors. The following conditions were used: drop space of 20 µm for all inks, six printed layers of active material using a pre-cure time at 50 ºC for 30 min and a final cure at 130 ºC for 15 min.

Figures 4.6a) and 4.6b) show the selected pattern for the sensor array and the final result, respectively. It is to notice that the printing of a sensor array consist in the replication of the printing procedure of a single sensor. No interconnections between individual sensors are present.

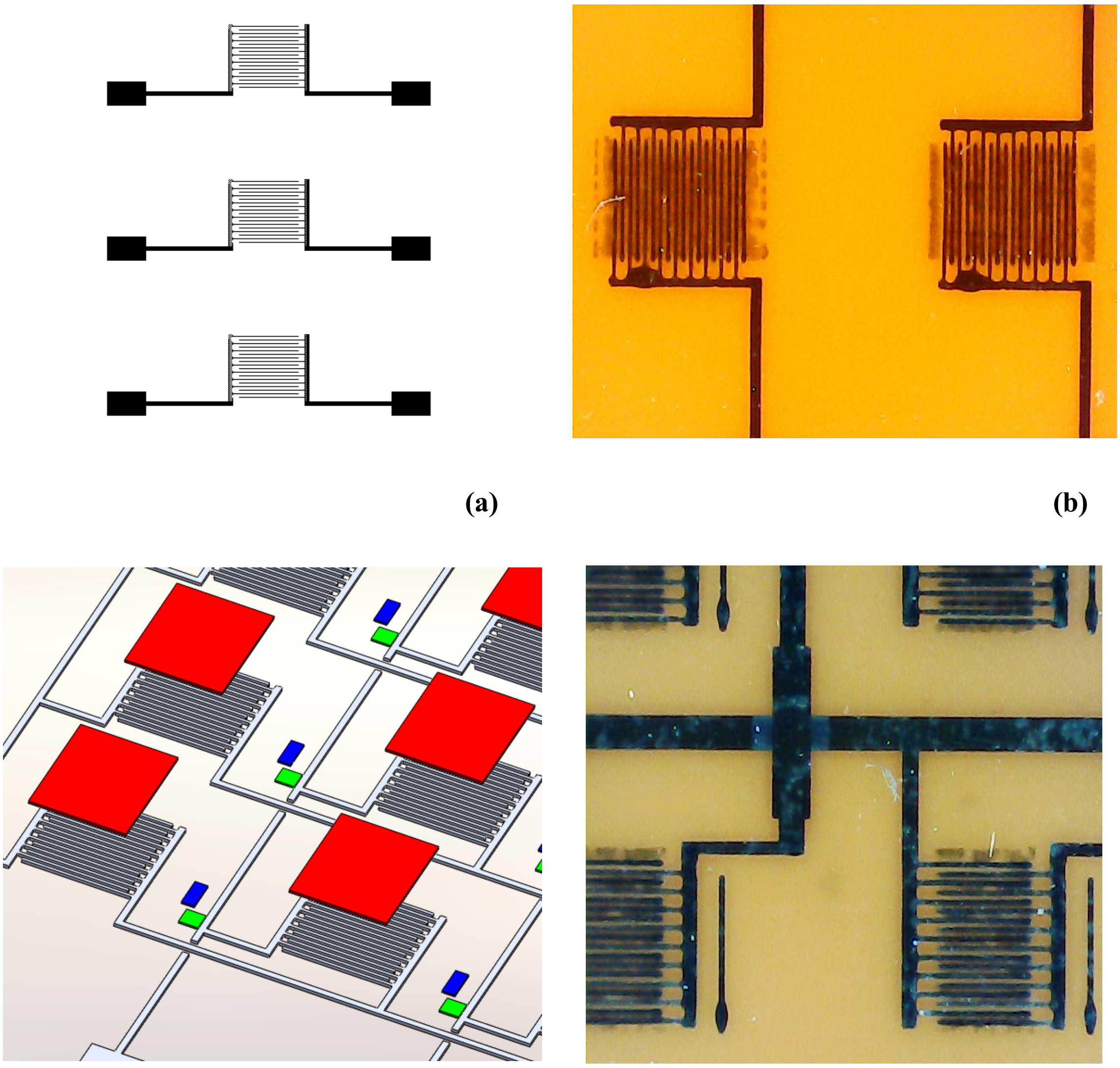

(a) **(b)**

(c) **(d)**

Figure 4.6 – a) Design of the array pattern, b) final result of the printed array, c) design of the different layers needed for the printing of the sensor matrix and d) printed sensor matrix.

The design of the sensor matrix is more complex (figure 4.6c) due to the set of connections that defines the sensor matrix. Further, the printing of a large number of sensors, a matrix of 4 x 5 sensors in the present case, increases the risk of defects that can invalidate the entire printed structure.

For the development of the matrix, four different layers have to be printed as shown in figure 4.6c). The first layer is the more complex: it is composed by the interdigitated electrodes and the mesh of connections. The area of interception between lines and columns is left out of printing. The fact of printing the entire conductive structure in the first printing step allows detecting early eventual defects in the printing structure which can hinder the functioning and performance of the sensors.

The second layer is printed using the insulating ink to allow the printing of conducting rows and columns without short-circuiting. It was necessary to print two layers able to guarantee the prefect insulation between the conductive layers.

The third layer corresponds to another conductive layer used to complete the connection of the various segments of column-line connections as shown in figures 4.6c) and 4.6d). The second layer has a height corresponding to the sum of the thickness of the first conductive layer and the second insulating layer. The second conductive layer has to overcome this difference of heights to guarantee the continuity of the lines by printing two layers.

Finally, the PeDOT layer is printed following the optimized conditions obtained for the single sensor printing.

Certainly, other printing configurations and strategies could be proposed for the same final objective, but this configuration allows an easy printing of the first layer, which is the most complex, and therefore the rapid verification of possible errors or discontinuities that could prevent the successful fabrication of the sensor matrix. A detail of the printed sensor matrix is shown in figure 4.6d).

4.3.4. Electro-mechanical sensor array and matrix characterization

Four point bending tests with simultaneous measurement of the electrical resistance were performed for the sensor arrays and matrix. Five cycles were applied with a maximum deformation of 2 mm at a deformation speed of 1 mm/min at room temperature, the distance between the two bending points being 26 mm (figure 4.2).

As previously mentioned, an electronic system was developed able to measure the 20 sensors simultaneously. The variation of the sensor resistance is converted to a variation of voltage that is the output data of the system. The recorded data can be converted to the variation of the resistance of the sensor using equation 4.1.

Figure 4.7a) shows a typical example of the data obtained for the tests performed in the PR sensors array. The response of the sensors is similar to the obtained results for the individual sensors and also reproducible among the different sensors. The decrease of the d.c. component with increasing number of cycles due to the effect of relaxation of the material, as verified in the case single sensors, is maintained.

It is concluded that compared with the case of single sensors, the response in array configuration is the same, indicating the validity of the printing technique for reproducing the characteristics of several printed sensors and therefore for large scale production.

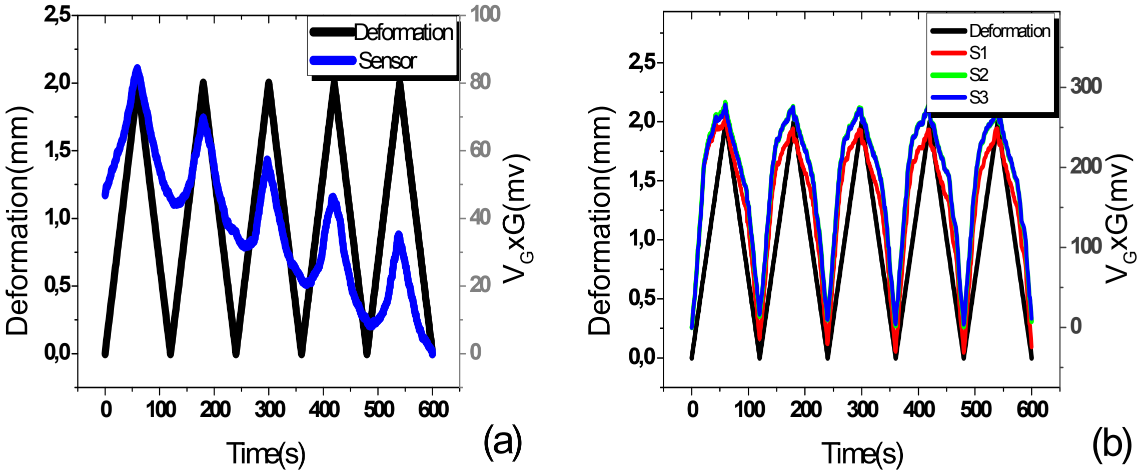

Figure 4.7 – a) representative cyclic strain applied to an array of sensors and the corresponding electrical variation over time and b) representative cyclic strain applied to a sensor matrix and electrical response of 3 sensors within the matrix.

Figure 4.7b) shows a typical example of the response of 3 sensors of the array when cyclic deformation tests were performed for PR sensor matrix. It can be verified that the response is identical to the single sensors and with a high reproducibility of the response among the various sensors.

The GF of matrix and array were also identical, within experimental error, to those found in single sensors tests, which demonstrates the good reproducibility of ink-jet fabrication technique.

4.3.5. Smart prosthesis development

Finally, the developed PR sensors were applied to the development of smart hip-prostheses. The use of artificial prosthetic replacements has become an important surgical procedure in orthopedic human joint diseases, but the success of this kind of procedure depends on the fixation of the artificial prosthetic component after being implanted in the thighbone [28]. The materials used for the fixation are subject to mechanical stresses, which originate permanent deformations, incipient cracks and even fatigue fractures[29], [30].

The concept of smart hip-prostheses is understood as the placing force and deformation sensors that will allow to perform a monitoring of small dislocations between the prostheses and the bone. This information is very important in order to improve prosthesis design and to promote high durability of the prosthesis, comfort and reliability to the patient.

A set of piezoresistive PeDOT sensors were placed in a hip prosthesis and mechanical fatigue test in the compressive mode were performed according to standard ISO 7206 [25] (figure 4.8a). According to the testing conditions, a maximum load was applied to the material and then a dynamical load was applied from a minimum load of 10 % of the maximum load up to the maximum load, during 1000 cycles. The mechanical conditions applied to the hip-joint prosthesis involved three forces (1300 N, 2600 N and 4000 N) and for each force three frequencies of oscillation (0.5 Hz, 1 Hz and 5 Hz) were used. The electrical response of the sensors was obtained by the same electronic circuit used to characterize the sensors array and matrix.

Figure 4.8b) shows the typical response of the sensors as a function of displacement of the hip-prosthesis in a real test condition. The results show that the electrical response allows to precisely quantify the mechanical solicitations applied to the hip prosthesis. In this case the response is the inverse to the mechanical request since the sensor is placed in a zone in which there is a distension of the material when the prosthesis is subjected compression as observed in figure 4.8a).

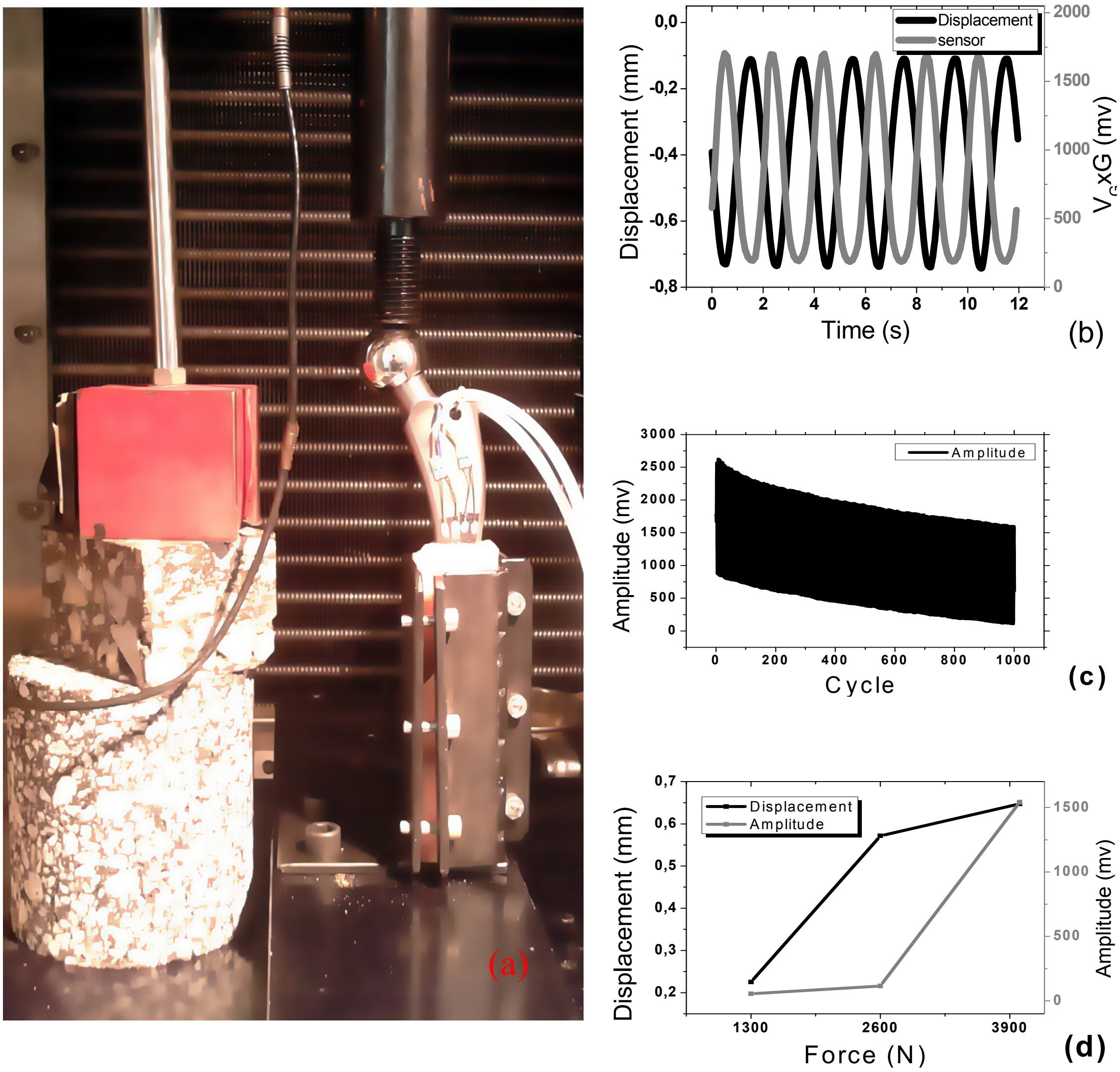

Figure 4.8 – a) Picture of the hip-prosthesis with the implemented sensors in the stress-strain experimental setup, b) PR measurement for the PeDot PR sensors performed with a maximum force of 4000 N, c) sensor response to 1000 cycles and c) prosthesis displacement and sensor amplitude response as a function of the applied force.

Figure 4.8c) shows a d.c. variation over time but a stable dynamic response as the sensor response maintains the amplitude variation over the 1000 cycles, which ensures the reproducibility of the sensor response. Finally figure 4.8d) shows the vertical displacement of the prosthesis and the amplitude as a function of the applied force. It is verified that the amplitude response of the sensor varies with the applied force on the prosthesis although this response is not linear due to the geometry of the prosthesis.

In this way, both frequency and force variation are detected and quantified by the developed sensors which show good stability up to 1000 mechanical cycles, indicating their suitability for this and related applications.

4.4. Conclusions

Multiple strain sensors with different architectures such as single, array and matrix have been developed by inkjet printing technology based on silver conductive ink (strain gages), PeDOT and TIPS-pentacene (piezoressitive sensors). The different materials and layers are optimized to achieve sensors with dimensions of 1.5 mm x 1.8 mm with interdigitated structures of 30 µm of distance between the fingers lines.

Characterized sensors show gauge factors up to 2.48 have been achieved with PeDOT, though larger values can be obtained depending on the curing conditions. The straing gages show gage factor around 0.35. The good reproducibility and robustness of the printed sensors are demonstrated through performance testes including 1000 mechanical cycles for the development of smart prosthesis applications.

It is therefore concluded that ink-jet printing is a technology suitable for the production of force and deformation sensors that can certainly be expanded to other type of sensor through suitable ink formulation and printing architecture design.

4.5. References

[1] S. H. Ko, H. Pan, C. P. Grigoropoulos, C. K. Luscombe, J. M. J. Fréchet, and D. Poulikakos, “All-inkjet-printed flexible electronics fabrication on a polymer substrate by low-temperature high-resolution selective laser sintering of metal nanoparticles,” *Nanotechnology*, vol. 18, no. 34, p. 345202, Aug. 2007.

[2] S. H. Ko, J. Chung, H. Pan, C. P. Grigoropoulos, and D. Poulikakos, “Fabrication of multilayer passive and active electric components on polymer using inkjet printing and low temperature laser processing,” *Sensors and Actuators A: Physical*, vol. 134, no. 1, pp. 161–168, Feb. 2007.

[3] M. Mantysalo, V. Pekkanen, K. Kaija, J. Niittynen, S. Koskinen, E. Halonen, P. Mansikkamaki, and O. Hameenoja, “Capability of inkjet technology in

electronics manufacturing," *Electronic Components and Technology Conference, 2009. ECTC 2009. 59th*. pp. 1330–1336, 2009.

[4] B. Ando and S. Baglio, "Inkjet-printed sensors: a useful approach for low cost, rapid prototyping [Instrumentation Notes]," *Instrumentation & Measurement Magazine, IEEE*, vol. 14, no. 5. pp. 36–40, 2011.

[5] A. Pacquit, J. Frisby, D. Diamond, K. T. Lau, A. Farrell, B. Quilty, and D. Diamond, "Development of a smart packaging for the monitoring of fish spoilage," *Food Chemistry*, vol. 102, no. 2, pp. 466–470, 2007.

[6] N. Leopold, S. Busche, G. Gauglitz, and B. Lendl, "IR absorption and reflectometric interference spectroscopy (RIfS) combined to a new sensing approach for gas analytes absorbed into thin polymer films," *Spectrochimica Acta Part A: Molecular and Biomolecular Spectroscopy*, vol. 72, no. 5, pp. 994–999, Jun. 2009.

[7] J. Spadavecchia, G. Ciccarella, P. Siciliano, S. Capone, and R. Rella, "Spin-coated thin films of metal porphyrin–phthalocyanine blend for an optochemical sensor of alcohol vapours," *Sensors and Actuators B: Chemical*, vol. 100, no. 1–2, pp. 88–93, Jun. 2004.

[8] B. B. Kale, "Ink-Jet Printed Conducting Polyaniline based Flexible Humidity Sensor," in *14th International Meeting on Chemical Sensors - IMCS 2012*, 2012, pp. 1112–1115.

[9] B. Andò, S. Baglio, S. La Malfa, and G. L. Episcopo, "All inkjet printed system for strain measurement," in *IEEE sensors, 2011*, 2011, pp. 215–217.

[10] K. Abe, K. Suzuki, and D. Citterio, "Inkjet-printed microfluidic multianalyte chemical sensing paper.," *Analytical chemistry*, vol. 80, no. 18, pp. 6928–34, Sep. 2008.

[11] L. R. Allain, D. N. Stratis-Cullum, and T. Vo-Dinh, "Investigation of microfabrication of biological sample arrays using piezoelectric and bubble-jet printing technologies," *Analytica Chimica Acta*, vol. 518, no. 1–2, pp. 77–85, Aug. 2004.

[12] M. S. Hasenbank, T. Edwards, E. Fu, R. Garzon, T. F. Kosar, M. Look, A. Mashadi-Hossein, and P. Yager, "Demonstration of multi-analyte patterning

using piezoelectric inkjet printing of multiple layers," *Analytica Chimica Acta*, vol. 611, no. 1, pp. 80–88, Mar. 2008.

[13] "All-Inkjet-Printed Organic Thin-Film Transistors with Silver Gate, Source/Drain Electrodes," *Japanese Journal of Applied Physics*, vol. 50, no. 3, p. 03CB05, 2011.

[14] S. Chung, S. O. Kim, S.-K. Kwon, C. Lee, and Y. Hong, "All-Inkjet-Printed Organic Thin-Film Transistor Inverter on Flexible Plastic Substrate," *IEEE Electron Device Letters*, vol. 32, no. 8, pp. 1134–1136, Aug. 2011.

[15] P. Alpuim, V. Correia, E. S. Marins, J. G. Rocha, I. G. Trindade, and S. Lanceros-Mendez, "Piezoresistive silicon thin film sensor array for biomedical applications," *Thin Solid Films*, vol. 519, no. 14, pp. 4574–4577, May 2011.

[16] D. R. Myers and A. P. Pisano, "Torque measurements of an automotive halfshaft utilizing a MEMS resonant strain gauge," *Solid-State Sensors, Actuators and Microsystems Conference, 2009. TRANSDUCERS 2009. International*. pp. 1726–1729, 2009.

[17] M. Erinc, H. J. van de Wiel, R. J. Werkhoven, A. Pongracz, G. Battistig, and H. R. Fischer, "Vibration characterization of a MEMS 3D force sensor," *Thermal, Mechanical and Multi-Physics Simulation and Experiments in Microelectronics and Microsystems (EuroSimE), 2011 12th International Conference on*. pp. 1/6–6/6, 2011.

[18] J. N. Pereira, P. Vieira, a. Ferreira, a. J. Paleo, J. G. Rocha, and S. Lanceros-Méndez, "Piezoresistive effect in spin-coated polyaniline thin films," *Journal of Polymer Research*, vol. 19, no. 2, pp. 0–6, Feb. 2012.

[19] A. Ferrreira, J. G. Rocha, A. Ansón-Casaos, M. T. Martínez, F. Vaz, and S. Lanceros-Mendez, "Electromechanical performance of poly(vinylidene fluoride)/carbon nanotube composites for strain sensor applications," *Sensors and Actuators A: Physical*, vol. 178, no. 0, pp. 10–16, May 2012.

[20] P. Costa, J. Silva, V. Sencadas, R. Simoes, J. Viana, and S. Lanceros-Méndez, "Mechanical, electrical and electro-mechanical properties of thermoplastic elastomer styrene–butadiene–styrene/multiwall carbon nanotubes composites," *Journal of Materials Science*, vol. 48, no. 3, pp. 1172–1179, 2013.

[21] A. Ferreira, P. Cardoso, D. Klosterman, J. a Covas, F. W. J. van Hattum, F. Vaz, and S. Lanceros-Mendez, “Effect of filler dispersion on the electromechanical response of epoxy/vapor-grown carbon nanofiber composites,” *Smart Materials and Structures*, vol. 21, no. 7, p. 075008, Jul. 2012.

[22] RS-Components., “Mild steel foil strain gauge,” 2012. [Online]. Available: http://uk.rs-online.com/web/p/strain-gauges/0632168/.

[23] J. P. Lynch, A. Partridge, K. H. Law, T. W. Kenny, A. S. Kiremidjian, and E. Carryer, “Design of Piezoresistive MEMS-Based Accelerometer for Integration with Wireless Sensing Unit for Structural Monitoring,” *Journal of Aerospace Engineering*, vol. 16, no. 3, pp. 108–114, Jul. 2003.

[24] S. Sugiyama, K. Kawahata, M. Yoneda, and I. Igarashi, “Tactile image detection using a 1k-element silicon pressure sensor array,” *Sensors and Actuators A: Physical*, vol. 22, no. 1–3, pp. 397–400, Jun. 1989.

[25] ISO, “Implants for surgery -- Partial and total hip joint prostheses.” International Organization for Stardardization, 2010.

[26] U. FUJIFILM, “Dimatix DMP-2800,” 2012. [Online]. Available: http://www.fujifilmusa.com/products/industrial_inkjet_printheads/index.html. [Accessed: 06-Oct-2012].

[27] a. J. Paleo, F. W. J. Hattum, J. G. Rocha, and S. Lanceros-Méndez, “Piezoresistive polypropylene–carbon nanofiber composites as mechanical transducers,” *Microsystem Technologies*, vol. 18, no. 5, pp. 591–597, Mar. 2012.

[28] F.-C. Chang, J.-P. Hung, and Y.-L. Lai, “Finite Element Analysis on the Mechanical Effect of a Roughened Stem for Cemented Hip Prosthesis,” *Computer Science and Information Engineering, 2009 WRI World Congress on*, vol. 3. pp. 254–258, 2009.

[29] J. B. Park, “Hip Joint Prosthesis Fixation-Problems and Possible Solutions.,” in *The Biomedical Engineering Handbook, Second Edition.*, 2nd ed., J. D. . Bronzino, Ed. CRC Press, 1999.

[30] S. Pramanik, A. K. Agarwal, and K. N. Rai, “Chronology of Total Hip Joint Replacement and Materials Development,” vol. 19, no. 1, pp. 15–26, 2005.

5. Adaptive Sensor Interface Circuit for Piezoresistive Sensor Arrays

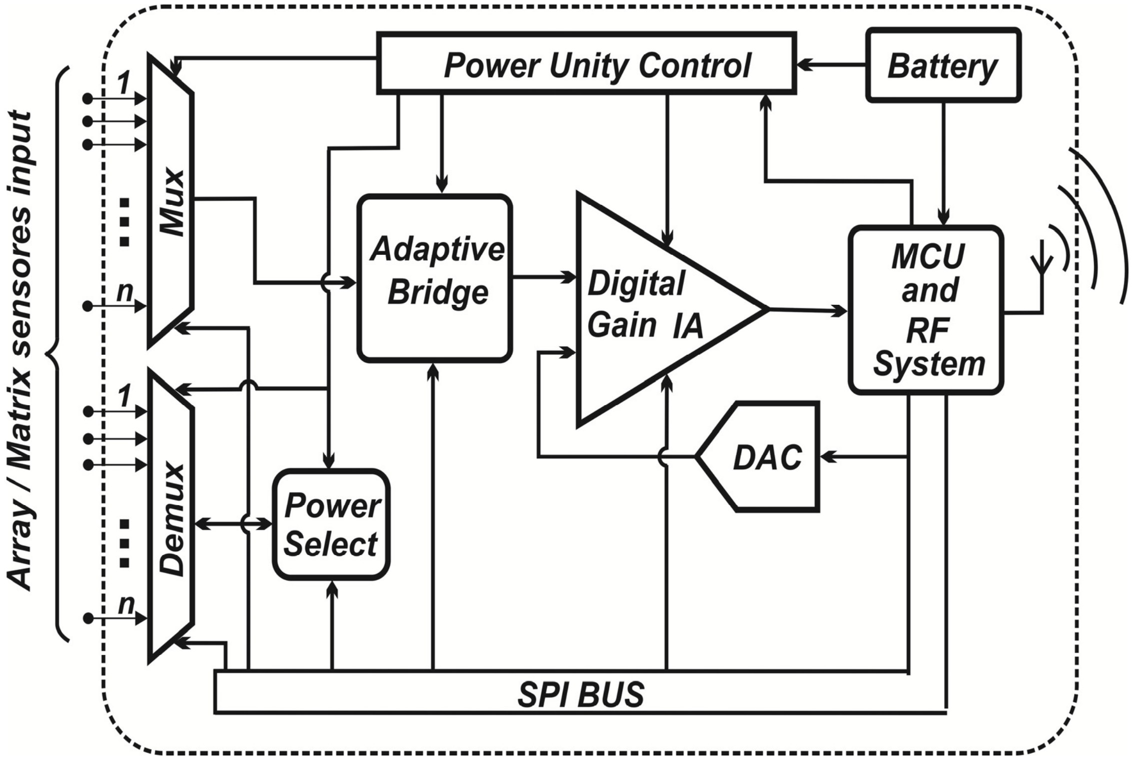

This chapter is based on the following publication: V. Correia, J. G. Rocha, V. Sencadas and S. Lanceros-Mendez. Adaptive Sensor Interface Circuit for Piezoresistive Sensor Arrays. Submitted to IEEE Sensors, 2013.

5.1. Introduction

Advances in materials technology allow creating an increasing number of sensors that can be implemented in different application fields such as biomedical and aeronautics. Moreover, technology development promotes an increasing demand of sensors, in particular micro-sensors, for a wide spectrum of applications, from automation, industrial process control and automotive industry, among many others [1].

The increasing application range and demand of sensors also implies the need to develop novel signal conditioning and signal processing systems able to support a large number of sensors simultaneously, with a precise and reliable reading of the measured signals. Therefore, parallel to the development of sensor technologies, the field of signal conditioning and processing has also evolved in terms of size of the electronic components, processing capacity and energy consumption in order to meet the increasingly demanding needs [2], [3].

There are already some systems integrating the conditioning circuit and processing unit with the transducers [1], [4], [5], entitled as smart sensor generation. Whenever is needed the development and measurement of flexible sensors arrays built using different sensors or sensors technologies [6], it arises the need for implementation of different measurement circuit for each sensor type. In other cases this need is due to differences in the characteristics and response of the sensors due to processing restrictions in their construction, e.g. in printing sensor technologies. This problem becomes particularly important when the sensors aim to be applied within the human body, as restrictions are also imposed in terms of biological compatibility, dimensions, energy consumption and calibration, as it is not possible to calibrate the circuit after body implantation due to access restrictions.

Developments in systems that allows the connection of different types of sensors [7-9] or multi-channel reading circuits for a single type of sensor [10], [11] have been therefore developed. In order to avoid single sensor calibration, a system able to support self-test and self-calibration, supporting multi-ranging within a single sensor, dissipating low power, occupying small die area and, preferentially, with no external components must be settled. Yazdi et al. [7] developed a generic interface circuit for capacitive sensors within a smart multi-element microsystems, able to interface with a large variety of capacitive sensors with base capacitance and sensitivity spread over a wide range, supporting communication with a microcontroller over a standard sensor bus, with programmable gain and offset control, supporting sensor self-test and with low power consumption. Later on, Xi et al. [9] presented a multi-sensor system-on-chip (SoC) integrating programmable processor, universal sensor interface and an analogic to digital converter as well as others on chip resources. This technology integrates an 8-channel reconfigurable sensor interface that employs a Wheatstone bridge and switched-capacitor topologies to perform signal conditioning for a wide range of resistive and capacitive sensors. These systems nevertheless support a large variety of sensors at the cost of resolution and hardware efficiency and do not have the processing capabilities necessary to make the auto calibration of the circuit.

The present work shows the development of an electronic system allowing measuring piezoresistive sensor arrays with sensors of different characteristics that can automatically adapt its hardware and firmware parameters to the sensor to be read and that guarantees the highest accuracy as a function of hardware efficiency. It represents therefore a multiplexed input system which allows connecting all sensors to a single circuit. The adaptive sensor interface was applied in a piezoresistive sensor array for implantable hip joint prostheses and the sensor signal was acquired.

The following sections show the circuit architecture and its major building blocks, as well as the circuit implementation and the developed firmware to command the architecture.

5.1.1. Adaptive system architecture

For integration as a part of piezoresistive sensor system for applications in areas such as biomedical, the sensors readout circuit should occupy the lowest possible area and should be able to operate with the lower possible power consumption. Furthermore, sensor block interface should be highly configurable to allow system control to perform self-test and self-sensor calibration.

In the present work, all the sensors are piezoresistive, which allows building an optimized circuit specifically for this type of sensors with larger hardware efficiency and minimum power consumption (figure 5.1). The developed microsystem uses an open architecture, using a single read out circuit for all sensors, allowing a substantial reduction of the implementation area.

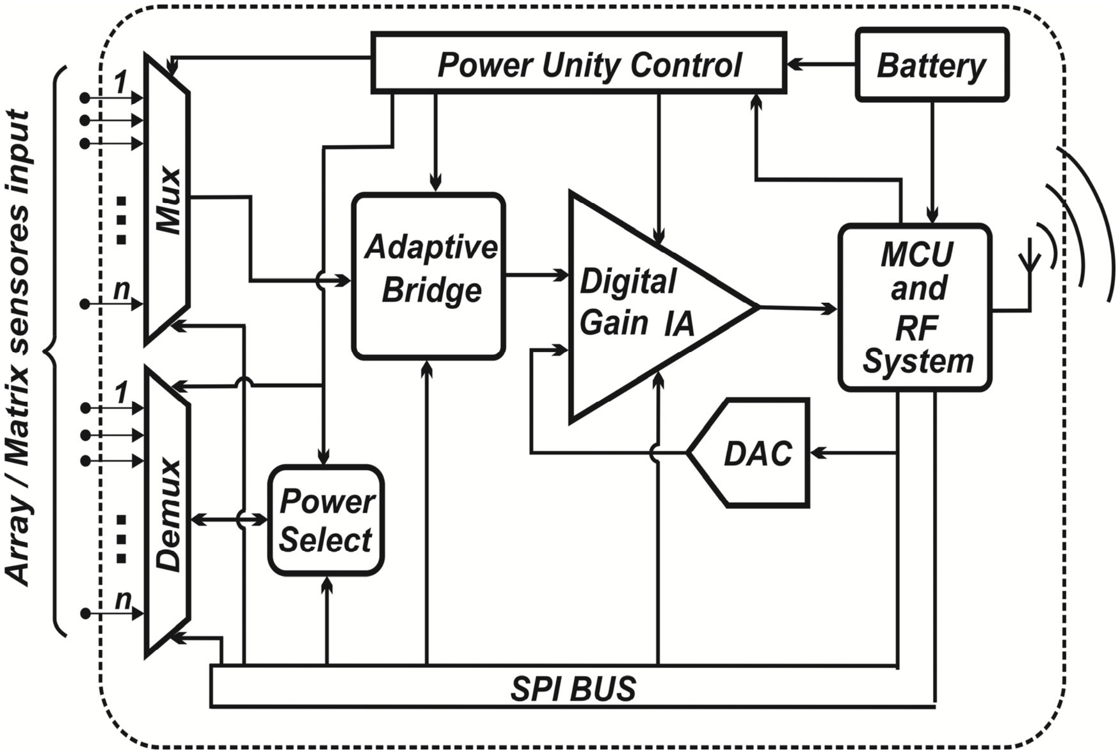

Figure 5.1 - Block diagram of the adaptive multi-sensor interface circuit.

In figure 5.1 it is shown that the various sensors are connected to a multiplexer circuit allowing the activation of each sensor independently, thus ensuring that the rest are in open circuit and does not affect the measurement and no power is spent. A multiplexing circuits for eight channels was developed, but it can be easily up-scaled to a larger number of channels as the read out circuit is independent of the number of input channels.

The aim of this adaptive multi-sensor interface circuit is to be implemented in in-body biomedical applications, thus it is necessary to remove all components for manual calibration as, once sensors are implemented, they can no longer be accessed. In order to overcome this issue, a non-balanced (NB) adaptive bridge a approach was adopted, that is connected to the digital gain instrumentation amplifier (IA) being the NB compensated by the digital-to-analog converter (DAC) connected to the other input of the IA.

The heart of this microsystem is a microcontroller unit (MCU), where the control program and the standard calibration data of all sensors to read are stored as well as the implementation of the specific software routines for sensors calibration and digital compensation for each sensor. The communication of the MCU with the various blocks of read out circuit uses a serial peripheral interface (SPI) bus, which allows to control all circuits devices quickly and with a minimum of connections, and consequently with a minimum energy loss.

In order to minimize the energy consumption, a power unit control (PUC) responsible for disabling all system peripherals during the sleep mode and for enabling the peripherals when they are needed was implemented. It is controlled by the MCU, who is also responsible for the read-out and communication rate. The developed adaptive multi-sensor interface circuit is able to send the data via radio frequency (RF) to a remote platform, which is the final responsible for data recording. In order to maximize energy savings, the data transmissions is not performed in real time, but stored in the MCU memory to form a large package before sending, allowing to use the active transmission mode less often.

5.1.2. Circuit implementation

The developed architecture was implemented using commercial electronic components which enable a quick transition from the developed architecture to a functional prototype and to evaluate how the developed system meets the requirements. Figure 5.2 show the schematic circuit developed.

The sensors are connected between two 8:1 analog switches (IC1 and IC2) that allow the selection of the sensor to be measured, remaining the other ones in open circuit. On state resistance is a key factor in the choice of the analog switches, as for sensors with low nominal resistance, the internal resistance of the analog switch will interfere with the sensor measurement itself. Taking into account this issue, our choice fell on NX3L4051 by NXP Semiconductors [12] analog switches, because is a low-ohmic analog switch with a typical internal resistance of 0.5Ω for a voltage supply higher than 2.7 V. The overall dimension of the entire electronic circuit is very important, as it is intended to maintain the area of the sensors and the adaptive interface circuit as small as possible. In this sense, the above referred analog switch has 3 x 3x 0.5 mm^3, which is suitable for the intended purpose. Further, IC4 (figure 5.2) have the same characteristics as IC1 and IC2 but with only 2 channels available, allowing sensor selection source Vdd or GND.

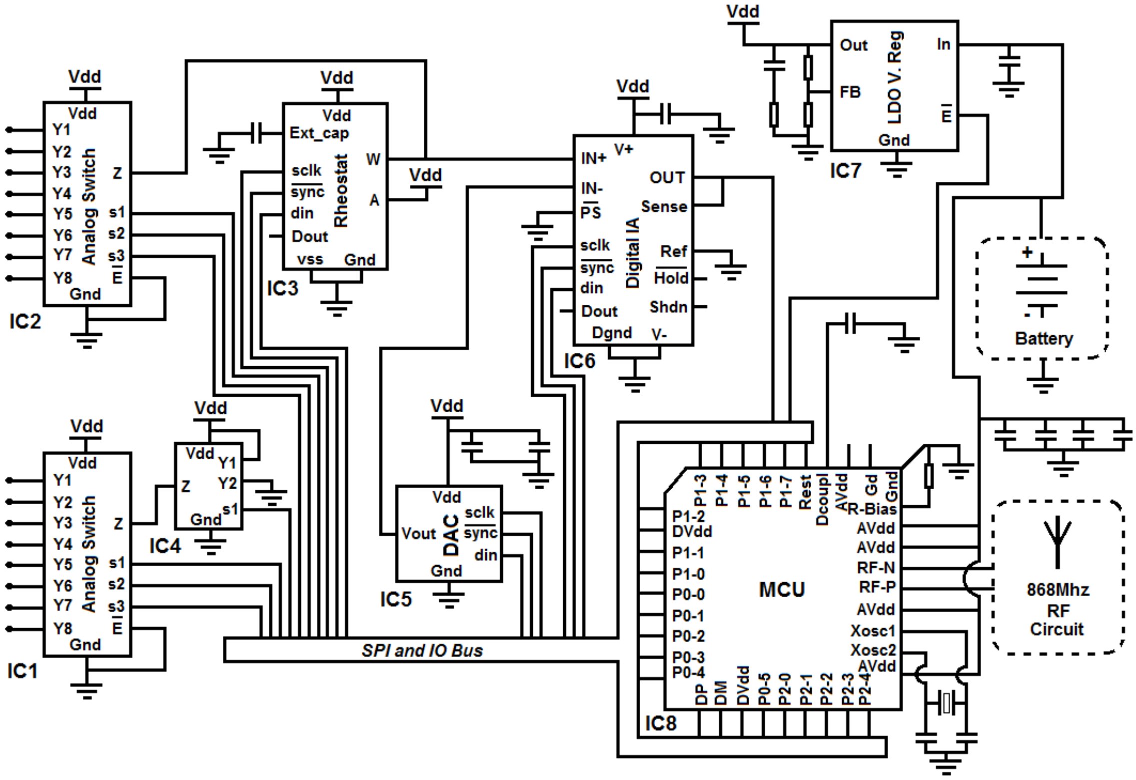

Figure 5.2 - Schematic of the adaptive interface circuit. The sensors are connected between the terminals of analog switch IC1 and IC2.

Once the selection of the sensor to be read is performed in IC1 and IC2, a digital rheostat connected in series and forming a non-balanced half bridge is used. In order to achieve an improved system resolution, it was selected a digital rheostat AD5270 by Analog Devices [13] with 10 bits of resolution and a 20 kΩ of full scale resistance with a maximum ± 1% of nominal resistor tolerance with a package dimensions of 3 x 3 x 0.8 mm^3. In figure 5.2, the middle point of the half bridge is connected to the positive input of the instrumentation amplifier (IA) with digitally programmable gain (IC6) and the negative input is connected to the output voltage of a 16 bits DAC (IC5) which allows adjusting the voltage and thus obtaining the maximum resolution of sensor measurement, completing the non-balanced bridge. It was used for IC6 the LTC6915 by Linear Technology [14], with fourteen levels of programmable gain and a size of 4 x 3 x 0.8 mm^3. IC5 is a AD5061 from Analog Devices [15] that is a low power 16 bits buffered out voltage DAC with a maximum error of 3 mV and a size of 3 x 3 x 1.2

mm^3. The output voltage of IA is converted to a digital signal using one of the 12 bits Analog to Digital Converter (ADC) present in the MCU (IC8). Beyond the signal conversion, the MCU is also responsible for the control of all circuit devices and performs the communication of all sensor data to a remote acquisition platform using RF communication (figure 5.1).

In this work it was used an MCU from Texas instruments (CC1111F32) [16], due to low power SoC with a standard enhanced 8051 MCU, 32 kB of in-system programmable flash memory, with 4 kB of RAM and a low power sub-1GHz RF transceiver, occupying only a volume of 6 x 6 x 0.8 mm^3.

Finally, IC7 is responsible for ensuring a regulated voltage to the circuit and allows turning off the power of the circuit when it is not needed by the control line, which is controlled by MCU. The IC used in this work is the NCP4682 from ON Semiconductors [17], with a low dropout line (LDO) voltage regulator and 1 x 1 x 0.6 mm^3 in size.

5.1.3. Firmware design

The developed adaptive multi-sensor interface circuit is totality based on digital components, allowing to be controlled by the MCU, and for which it was necessary the development of control and readout firmware. Being this an adaptive circuit and before starting to read the sensors, it is necessary to find the calibration parameters for each single sensor. Once the calibration parameters are found, they will be added to an algorithm implemented in the MCU (figure 5.3), which will be run once for each sensor.

The working method of the algorithm is divided in two stages: the first stage was designed to find the ideal resistance (R_{out}) value of the digital rheostat (DP). The algorithm starts to select the sensor to calibrate, changes the IA gain to 1 and puts the DAC output voltage to 0 V, in order to increase the range of readout of the circuit. Then, the R_{out} value will be changed until the voltage read on ADC (ADC_{read}) exceeds 0.5 V as described in the algorithm, the optimal R_{out} value is calculated, and the system will select and use the nearest available resistance.

The working method of the algorithm is divided in two stages: the first stage was designed to find the ideal resistance (R_{out}) value of the digital rheostat (DP). The algorithm starts to select the sensor to calibrate, changes the IA gain to 1 and puts the DAC output voltage to 0 V, in order to increase the range of readout of the circuit.

Then, the R_{out} value will be changed until the voltage read on ADC (ADC_{read}) exceeds 0.5 V as described in the algorithm, the optimal Rout value is calculated, and the system will select and use the nearest available resistance.

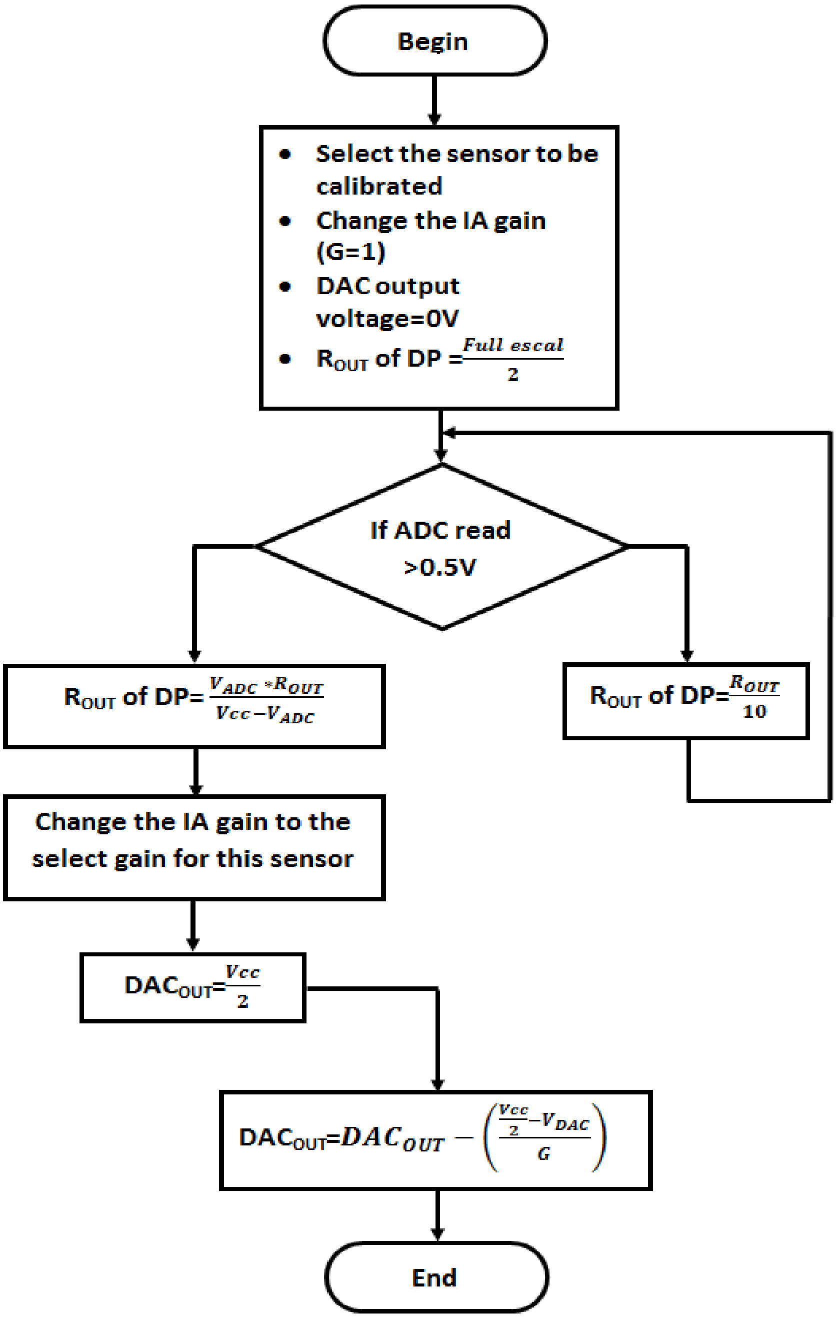

Figure 5.3 - Algorithm construction to determine the calibration parameters of the adaptive circuit for a particular sensor.

The second stage is used to determine the value of the output voltage of the DAC (DAC_{out}), so that the voltage read on the ADC for each sensor without solicitation is in half-scale, allowing to detect negative and positive variations, since the circuit just uses a single power supply. To determine this parameter, the value of the DAC_{out} is placed equal to half-scale and then the difference for the desired value is measured and compared to the new DAC_{out} value that certifies the half-scale. Finally, the calibration parameters found for each sensor are stored in the MCU memory to be used whenever a specific sensor is read.

Once the calibration parameters for each single sensor are found, the circuit is ready to perform measurements. Sensor selection and circuit configuration will be done by the parameters stored in memory and the ADC voltage will be measured. The value of measured voltage (ADC_{read}) is associated to the sensor resistance (R_{sensor}) according to equation 5.1:

$$R_{sensor} = \frac{R_{out}\left(ADC_{read} + (DAC_{out}G)\right)}{G(Vcc - DAC_{out}) - ADC_{read}}$$

(eq. 5.1)

The measured values are saved in memory and only when the memory is full the RF sending data routine is started, saving energy, as data communication is the process that consumes more energy and it will be just started whenever needed. Between measurements the system goes into sleep mode turning off all circuit, being only the MCU active but in operating mode 2 with timer interrupt wake-up.

5.2. Experimental work and results

The adaptive sensor interface circuit was implemented in a small printed circuit board (PCB) using just 135 mm^2 of area for all circuit and 225 mm^2 for the RF circuit. The range of input sensor resistance is between 50 Ω and 100 kΩ ensuring the same gain for each sensor within this range, managing to achieve a reading rate of 2 kHz. If the system considers that sending data package is needed to a remote platform, the read rate drops to 1 kHz. The minimum transmission time for a 256 kb package is 0.5 ms or 1 ms in normal communication mode.

Energy consumption of the adaptive multi-sensor interface circuit in the different operation modes has also been evaluated (figure 5.4). The values reported in figure 4 represent the worst possible situations and energy consumption can be optimized, depending on the distance of the remote platform, sensor characteristics and the electrical difference between sensors. The system was submitted to a series of experiments in order to evaluate and validate the operation mode of the system and the respective firmware, and the obtained data is presented in figure 5.4.

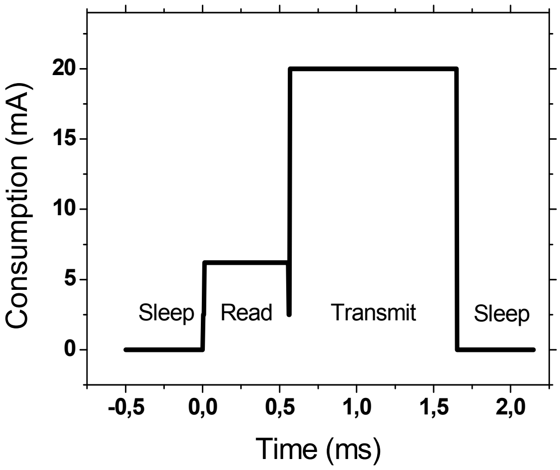

Figure 5.4 - Circuit consumption in the various operation states.

Finally, a set of sensors was placed on a surface of a hip-joint prosthesis and mechanical fatigue test in compressive mode were performed according to standard ISO 7206 [18] (figure 5.5a). Briefly, a typical mechanical fatigue test consists on the fitting of the prostheses to a 60% of the CT length (distance between the lower end of the prostheses to the geometrical center of the head) within the mold with inclination angles α (10º ±1) and β (9º ±1) of the axis of the prosthesis with respect to the front and lateral sides of the mold cavity. With respect to the testing conditions, a maximum load was applied to the material and then a dynamical load was applied from a minimum load of 10 % of the maximum load up to the maximum load, during 1000 cycles. The mechanical conditions applied in the experiments performed in the hip-joint prosthesis are summarized in table 5.1 and a schematic view of experimental setup is presented in figure 5.5a). The mechanical conditions applied to the hip-joint prosthesis involved three forces (1300, 2600 and 4000 N) and for each force three frequencies of oscillation (0.5, 1 and 5 Hz) were used.

Piezoresistive sensor characteristics are shown in figure 5.5b). The sensors were selected as they show different initial resistances when they are without mechanical solicitation, therefore, an adaptive multi-sensor interface circuit to perform sensors measurement with accuracy under dynamic conditions is an advantage. Typical sensor response under mechanical solicitation is reported in figure 5.5c). It can be observed that the electrical response follows the dynamic strain signal applied to the prosthesis, and as expected, sensors with different characteristics show electrical responses with dissimilar amplitude.

(a)

Sensor	Type	R0 (Ω)	Ref.
S1	Commercial Strain Gauge	120	[12]
S2	Printed Piezoresistive sensor	881	[13]
S3	Piezoresistive Silicon film sensor	17850	[14]
S4	PVDF Piezoresistive sensor	388	[15]
S5	SVS Piezoresistive sensor	640	[16]

(b)

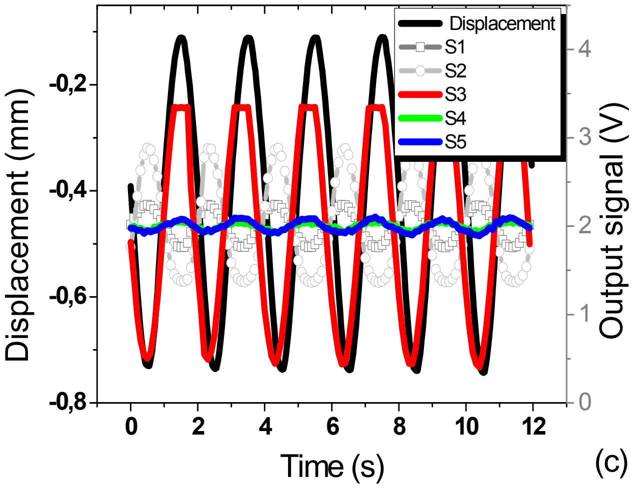

(c)

Figure 5.5 - a) Mechanical and electrical experimental setup of the hip-joint prosthesis; b) Sensor characteristics used to validate the adaptive multi-sensor interface circuit and c) Electrical and mechanical response of the instrumented hip-joint prosthesis for a maximum mechanical load of 4 kN.

Commercial strain gauge (S1) and ink-jet printed piezoresistive sensor (S2) show an electrical response in phase opposition when compared to the mechanical load due to the region of the prosthesis were the sensors are placed, as there is a material distension when the prosthesis is submitted to compression (figure 5.5a and c). Furthermore, the system reveals to provide good and accurate results for each sensor, despite their specific characteristics.

Taking into account the validation results for the adaptive multi-sensor interface circuit with different sensor characteristics, a flexible ink-jet printed sensor array with similar R0 for all sensors (figure 5.6a), was used in order to assure the accuracy, reproducibility and stability of the electronic system. In this measurement, a maximum mechanical deformation under compression of 2 mm was applied to the hip-joint prosthesis, at a speed of 1mm/min at room temperature, during 5 cycles (figure 5.6b).

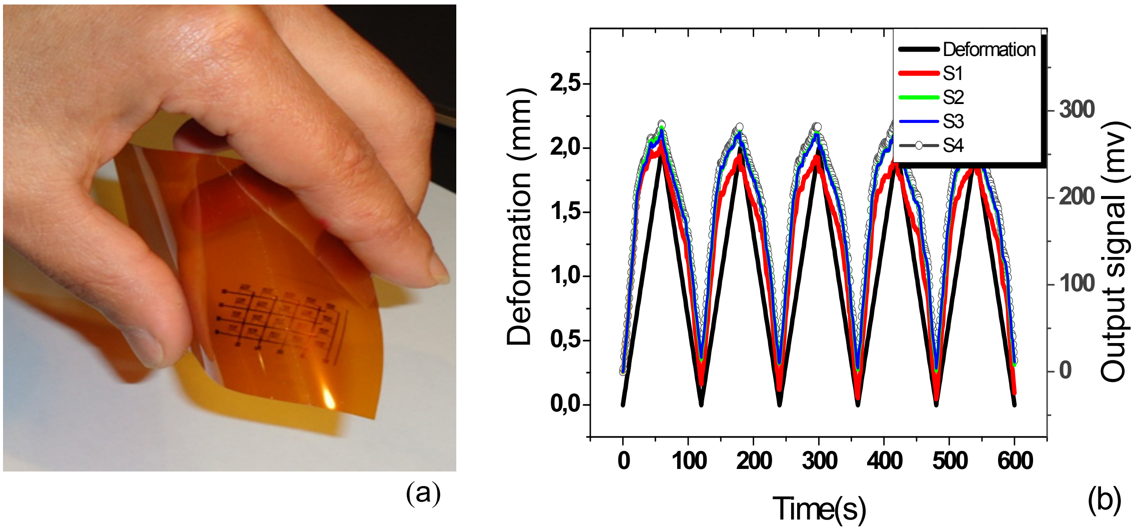

(a)

(b)

Figure 5.6 – a) Picture of the sensor matrix using in the experimental setup and b) mechanical deformation signal and amplitude response of three sensors.

Flexible inkjet-printed sensor array of 16 sensors showed that the electrical response from the sensors follows the mechanical solicitation, with a very similar electrical response between sensors (figure 5.6b), which demonstrates the stability and reproducibility of the developed adaptive multi-sensor interface circuit.

5.3. Conclusions

An adaptive readout system allowing the measurement of piezoresistive sensor arrays with different characteristics and high accuracy by multiplexing has been developed. This system can be up-scaled to read a large number of sensors, simply increasing the number of multiplexed input. This system is able to measure piezoresistive sensors with resistances from 50 Ω to 100 kΩ, with a maximum read rate of 2 kHz, meeting the requirements defined for the system. The area for the adaptive multi-sensor interface circuit is 135 mm^2, which is compatible with applications in in-body biomedical engineering. Energy consumption was optimized by adding the option to store in the internal memory the recorded data and sending the data just when the internal memory is full.

Mechanical experiments in a hip-joint prosthesis with piezoresistive sensor array with different characteristics and with an 16 inkjet-printed sensor array reveals that the adaptive multi-sensor interface circuit is able to measure with accuracy the sensor electrical response. Finally, this system is prepared to be size reduced by building the whole system on-chip.

5.4. References

[1] L. Dan, L. Ting, and Z. Dacheng, "A Monolithic Piezoresistive Pressure-Flow Sensor With Integrated Signal-Conditioning Circuit," *Sensors Journal, IEEE,* vol. 11, pp. 2122-2128, 2011.

[2] P. D. Dimitropoulos, S. P. Nikolaidis, D. P. Karampatzakis, and G. I. Stamoulis, "A low-power CMOS-VLSI circuit for signal conditioning in integrated capacitive sensors," in *Sensors, 2004. Proceedings of IEEE*, 2004, pp. 202-205 vol.1.

[3] A. Drumea, A. Vasile, M. Comes, and M. Blejan, "System on Chip Signal Conditioner for LVDT Sensors," in *Electronics Systemintegration Technology Conference, 2006. 1st*, 2006, pp. 629-634.

[4] Z. Yong, G. Yikang, V. Vlatkovic, and W. Xiaojuan, "Progress of smart sensor and smart sensor networks," in *Intelligent Control and Automation, 2004. WCICA 2004. Fifth World Congress on*, 2004, pp. 3600-3606 Vol.4.

[5] N. Medrano, M. T. Sanz, P. A. Martinez, S. Celma, and G. Zatorre, "An Analog-Digital Neural Processor for Integrated Sensor Conditioning," in *Electronics, Circuits and Systems, 2006. ICECS '06. 13th IEEE International Conference on*, 2006, pp. 926-929.

[6] Y. J. Yang, M. Y. Cheng, W. Y. Chang, L. C. Tsao, S. A. Yang, W. P. Shih, F. Y. Chang, S. H. Chang, and K. C. Fan, "An integrated flexible temperature and tactile sensing array using PI-copper films," *Sensors and Actuators A: Physical,* vol. 143, pp. 143-153, 2008.

[7] N. Yazdi, A. Mason, K. Najafi, and K. D. Wise, "A generic interface chip for capacitive sensors in low-power multi-parameter microsystems," *Sensors and Actuators A: Physical,* vol. 84, pp. 351-361, 2000.

[8] Y. Chao, A. Mason, X. Jinwen, and Z. Peixin, "Configurable Hardware-Effcient Interface Circuit for Multi-Sensor Microsystems," in *Sensors, 2006. 5th IEEE Conference on*, 2006, pp. 41-44.

[9] X. Jinwen, Y. Chao, A. Mason, and Z. Peixin, "Adaptive Multi-Sensor Interface System-On-Chip," in *Sensors, 2006. 5th IEEE Conference on*, 2006, pp. 50-53.

[10] Z. Jichun and A. Mason, "Characterization of a configurable sensor signal conditioning circuit for multi-sensor microsystems," in *Sensors, 2004. Proceedings of IEEE*, 2004, pp. 198-201 vol.1.

[11] Z. Jichun, Z. Kun, W. Zhigang, and A. Mason, "A Universal Micro-Sensor Interface chip with network communication bus and highly programmable sensor readout," in *Circuits and Systems, 2002. MWSCAS-2002. The 2002 45th Midwest Symposium on*, 2002, pp. II-246-II-249 vol.2.

[12] NXPSemiconductors. (2012). *Single low-ohmic 8-channel analog switch*. Available: http://www.nxp.com/documents/data_sheet/NX3L4051.pdf

[13] Analog_Devices. (2009, 2012). *AD5270/AD5271 - Memory Digital Rheostat*. Available: http://www.analog.com/static/imported-files/data_sheets/AD5270_5271.pdf

[14] L. Technology. (2012). *LTC6915 - Zero Drift, Precision Instrumentation Amplifier with Digital Programmable Gain*. Available: http://cds.linear.com/docs/Datasheet/6915fb.pdf.

[15] Analog_Devices. (2011). *16-Bit Vout nanoDAC*. Available: http://www.analog.com/static/imported-files/data_sheets/AD5061.pdf

[16] T. Instruments. (2012). *Low-Power SoC with MCU, Memory Sub-1GHz RF Transceiver*. Available: http://www.ti.com/lit/ds/swrs033g/swrs033g.pdf

[17] O. Semiconductor. (2012). *150 mA, Ultra Low Supply Current, Low Dropout Regulator*. Available: http://www.onsemi.com/pub_link/Collateral/NCP4682-D.pdf

[18] I. S. Organization, "Implants for surgery - Partial and total hip joint prostheses," vol. ISO 7206, ed: International Standard Organization, 2002.

[19] RS Amidata S.A. (2012). *Foil Strain Gauges And Accessories*. Available: http://docs-europe.electrocomponents.com/webdocs/0077/0900766b80077de6.pdf

[20] V. C. Correia, Cristina; Casellas, C; Francesch, Laura; Rocha, Gerardo; Lanceros-Mendez, Senentxu, "Development of inkjet printed strain sensors," *ACS Applied Materials & Interfaces,* vol. Submitted on 19-01-2013, 2013.

[21] P. Alpuim, V. Correia, E. S. Marins, J. G. Rocha, I. G. Trindade, and S. Lanceros-Mendez, "Piezoresistive silicon thin film sensor array for biomedical applications," *Thin Solid Films,* vol. 519, pp. 4574-4577, 2011.

[22] A. Ferrreira, J. G. Rocha, A. Ansón-Casaos, M. T. Martínez, F. Vaz, and S. Lanceros-Mendez, "Electromechanical performance of poly(vinylidene fluoride)/carbon nanotube composites for strain sensor applications," *Sensors and Actuators A: Physical,* vol. 178, pp. 10-16, 2012.

[23] P. Costa, J. Silva, V. Sencadas, R. Simoes, J. C. Viana, and S. Lanceros-Méndez, "Mechanical, electrical and electro-mechanical properties of thermoplastic elastomer styrene–butadiene–styrene/multiwall carbon nanotubes composites," *Journal of Materials Science,* vol. 48, pp. 1172-1179, 2013/02/01 2013.

6. Ultra-High Band Radiowave Propagation Analysis for implanted Biosensors Communication System

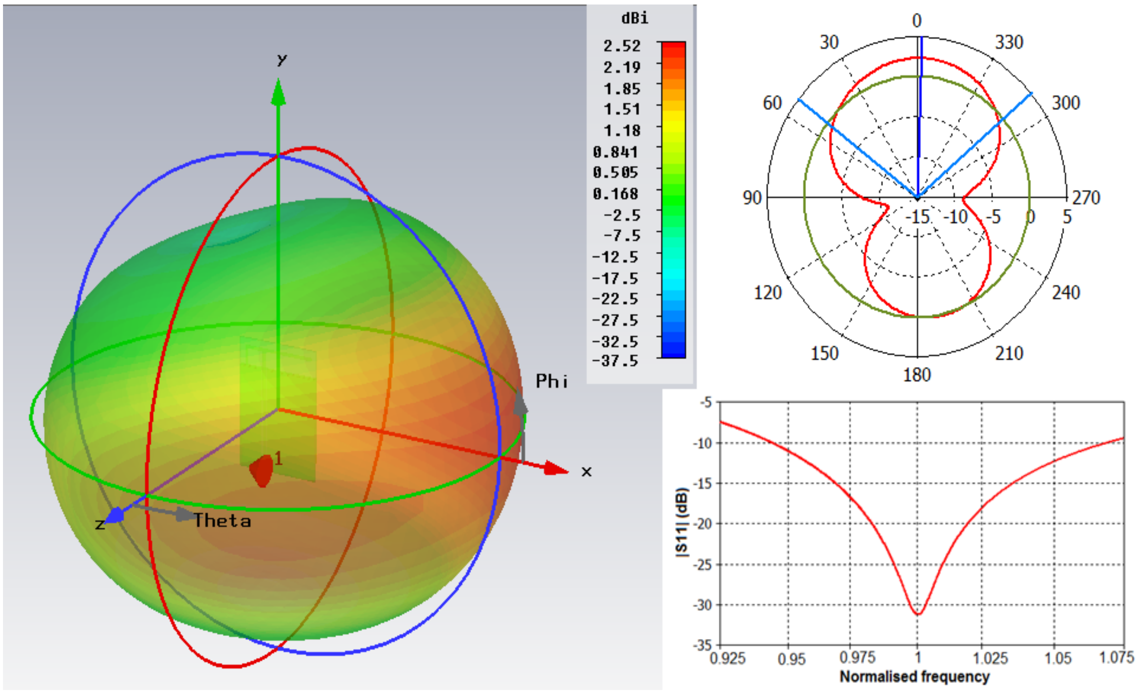

This chapter is based on the following publication: V. Correia, J. G. Rocha, C. Ribeiro and S- Lanceros-Mendez. *Ultra-High Band Radiowave Propagation Analysis for implanted Biosensors Communication System.* Submitted to IEEE Transactions on Biomedical Engineering, 2013.

6.1. Introduction

In the last years, medical implants are increasingly used in modern medicine as a key to success in the treatment of certain pathologies and allowing a substantial improvement of living conditions of the patients.

In 1958, with the development and implantation of the first Pacemaker by Rune Elmqvist, a new area in the medical implant field was opened [1], as it was the first implanted electronic device. Medical electronic implants have a remarkable history of success by being able to monitor patients conditions and to allow diagnosis and treatment of many diseases.

Nowadays, a large number of different electronic medical implants have been developed and/or are of common use such as brain pacemaker for the treatment of Parkinson´s disease [2], muscle stimulators [2], nerve signal decoders for robotic prostheses control [3], implantable drug pumps [4] and blood glucose sensing [5].

All of these implants require some kind of data communication system, which can be in one or two directions. Due to the recent developments on wireless communications devices there is a considerable interest in long distance communication between the implant and a remote platform. For example in [6], the neuronal activity and the activity of the nervous system are decoded to a dynamic control of the heart rate of a pacemaker. In this case, by a bidirectional link it is possible to reprogram the therapy and obtain the necessary diagnostic information in real time without the necessity of surgery.

Traditionally, the communication systems for implants make use of inductive communication that operate at medium-frequency (MF) or high-frequency (HF) [7]. With this approach the communication speed is typically low and requires a large area communication system, which hinders many potential implementations. The most attractive band for medical and biological implants is the ultrahigh frequency band (UHF). This band presents several advantages, such as allowing reduced antenna dimensions with low levels of interference, high data communication rates, offering a large frequency spectrum 300 MHz to 3 GHz and having a low cost due to its high use in mobile telecommunications systems.

The development of these devices requires surpassing some important challenges, including minimization of dc power requirement, problems related to the physical dimensions and wire-free communication. There are extensive investigations studying the influence of human body in UHF communications [8, 9], but these studies are mainly focused in the external antennas.

In this work, it is evaluated the influence of the human body in implanted antennas. The main objective is to obtain the antenna model and the frequency that better fits to the requirements for implantable devices. Therefore, it was investigated how the depth, the position of the antenna and the different layers that composed the human body affect the antenna response. The first step in the investigation was to find a frequency where radio signal could penetrate in body tissue and communicate with an external receptor. Three types of antennas (dipole antenna, circular antenna and the Inverted-F antenna (IFA)) were used working at three different frequencies, 433 MHz, 868 MHz and 2400 MHz. These frequencies were chosen because there are the no allocated frequency´s in UHF in Europe [10]. The study was performed using numerical techniques for solving electromagnetic wave propagation based in Finite Integration Technique (FIT) and Perfect Boundary Approximation technology (PBA) with the CST Microwave Studio software (CST MWS) and the Transient Solver option for the analysis of the antenna response.

6.2. Modeling and analysis

6.2.1. Computational technique

The CST MWS software which is a package for electromagnetic analysis in the high frequency range for 3D approach was used for the simulation of the antenna models.

This software is based on FIT which corresponds a spatial discretization scheme to numerically solve of electromagnetic field problems in time and frequency domains [11]. The main idea of this approach is to apply the Maxwell equations [12] in integral form to a set of staggered grids. This method stands out due to the high flexibility in modeling and boundary handling, as well as the incorporation of new materials with specified electrical, magnetic and mechanical properties. A finite calculation domain is then defined which is consequently split up into mesh cells, them are further split into two orthogonal grid systems. The use of a consistent dual orthogonal grid combining with an explicit time integration scheme leads to computing and memory-efficient algorithms, which are especially adapted for transient field analysis in radio frequency (RF) applications.

For this study, a transient solver option to perform the analysis of antenna response was used. This is a flexible time domain simulation module that calculates the transmission of energy between ports and open space of the simulated model. In this way, a frequency range of ±40% from the center frequencies, being these 433 MHz, 868 MHz and 2400 MHz, was used. The boundary conditions selected for all models are the open (add space) options for all axis, and in this way the model will be analyzed as being inside of an open space, which is desirable because it is intended to obtain the response of the antenna outside the human tissues. The model was excited with a Gaussian pulse in time domain and the hexahedral automatically mesh generator with a minimum resolution of 15 lines per wavelength was selected. The maximum truncation error was limited to 1% or -40 dB for all simulations.

This area was subject to a series of international standards [13] with the objective to protect the persons from RF risks. The most relevant restriction for these types of applications is a maximum peak of SAR level (specific absorption rate) inside the head and trunk of the user of 2 W.kg-1. These guidelines are accomplished for the simulated devices as they use an extremely low power and low duty-cycle by operating in a short-range network. Typically, this device uses 1 μW to 2 mW peak of radiated power with 1% of duty-cycle.

6.2.2. Antenna models

Antenna design is a common science and an engineering discipline with a large number of design manuals [14-16] and ongoing research [17-21]. However, most available information is devoted to antennas placed in a non-conducting surrounding with a relative permittivity of 1, i.e., the antennas are placed in vacuum or air. On the other hand, a completely different response is found when the antenna is placed inside the human body. In this case, the antenna is surrounded by a lossy material with high permittivity. UHF antennas are becoming attractive for medical and biological implants [22] and their investigation is still scarce and most of the few publications [23-25] are quite recent.

As described previously, three different types of antennas were investigated. The simulated models for each antenna type will be presented as well as the response in open space in order to compare to the simulations allowing to understand how the human body influences the antenna response.

6.2.2.1. Dipole antenna

The dipole antenna is a simple and common type of RF antenna, being widely used and incorporated into many other RF antenna designs [14-16].

As previously mentioned, each antenna model was simulated at three different frequencies. Three different antennas (one for each frequency) were thus designed with the dimensions described in table 6.1.

Table 6.1 - Dipole antenna dimension for 2400, 868 and 433MHz.

Frequency (MHz)	Dipole length (mm)	Wire diameter (mm)
2400	59.55	0.25
868	164.64	0.69
433	330.04	1.38

It is important to note that this type of antenna has a typical input impedance of 73 Ω. After the design of the antenna models, they were simulated in open space, the typical response of the dipole antenna being illustrated in figure 6.1, where it is represented the 3D radiation pattern, the polar radiation pattern and the return loss.

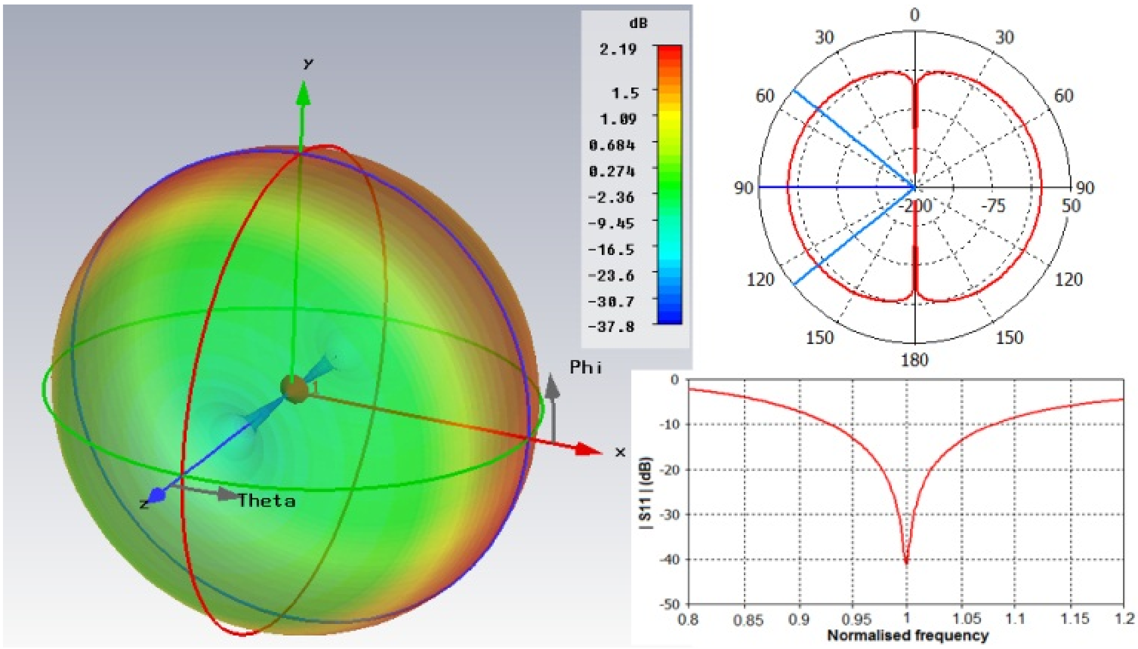

Figure 6.1 - Radiation pattern and return loss for a dipole antenna in free space for a frequency of 868MHz.

For the implemented dipole antenna, a main lobe magnitude of approximately 2.2 dB at 868 MHz with a variation of ~0.2 dB between the different frequencies was verified. This is an excellent response for this type of antenna and an angular width (3 dB) of approximately 77.2 degrees with a main lobe direction of 90 degrees was also verified (figure 6.1). In summary, this antenna has an excellent response in free space with practically 98% of radiation efficiency for all three frequencies.

6.2.2.2. Circular antenna

The circular loop antenna is a metallic conductor bent into the shape of a closed curve, making it a simple and versatile type of antenna. The loop antenna can take many others different configurations such as rectangular, square, triangular and elliptical but all presents similar electrical and magnetic behavior. This antenna type is commonly classified into two categories: electrically small and electrically large loops. The small loop antenna has a poor efficiency, so in this case, the electrically large loop type was used. This occurs since the self-resonant antenna has a circumference diameter approximately equal to the wavelength, and in this way the radiation efficiency is also high.

As for the circular antenna, three different antennas were designed with the dimensions presented in table 6.2.

Table 6.2 - Circular antenna dimension for 2400, 868 and 433 MHz.

Frequency (MHz)	Loop diameter (mm)	Wire diameter (mm)
2400	21.55	0.9
868	59.6	2.4
433	119.55	4.7

This type of antenna has a typical input impedance of 150 Ω. After the construction of these models, simulations in open space were conducted and the usual response of circular loop antennas was obtained, as represented in figure 6.2.

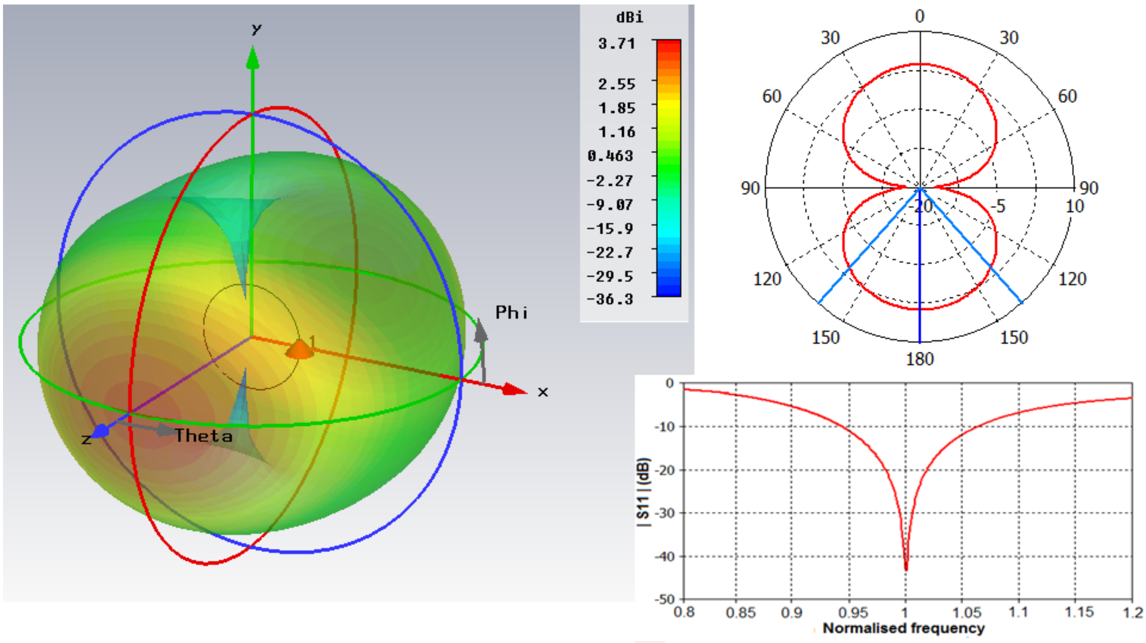

Figure 6.2 - Radiation pattern and return loss for a circular antenna in free space for a frequency of 868 MHz.

In the implementation of the circular antenna, it is observed a main lobe magnitude of approximately 3.7 dB at 868 MHz with a variation of ~ 0.6 dB between the different frequencies. This is an excellent response for this antenna and an angular width (3 dB) of approximately 82.8 degrees with a main lobe direction of 180 degrees was also verified with the radiation pattern represented in figure 6.2. In summary, this antenna in free space has an excellent response with ~ 97% of radiation efficiency for all three frequencies, which is similar to the value obtained for the dipole antenna.

6.2.2.3. IFA antenna

The IFA antenna typically consists on a rectangular planar element located above a ground plane, a short circuiting plate or pin, and a feeding system for the planar element. The Inverted F antenna or bent monopole antenna represents a variation at the level of the transmission line, where the top section has been folded down in order to be parallel with the ground plane. This is done to reduce the height of the antenna, while maintaining a resonant trace length. This parallel section introduces capacitance to the input impedance of the antenna, which is compensated by the implementation of a short-circuit stub. The stub’s end is connected to the ground plane in a way that the resulting antenna geometry resembles the letter F.

The antenna ground plane plays a significant role in its operation. The current excitation in the printed IFA will cause current excitation in the ground plane. The resulting electromagnetic field is formed by the interaction of the IFA and an image of itself below the ground plane. Its behavior as a perfect energy reflector is consistent only when the ground plane is infinite or much larger in its dimensions than the monopole itself. The ground plane should be at least as wide as the IFA length (L), and the ground plane should be at least $\lambda/4$ in height. The optimum location of the IFA in order to achieve an omni-directional far-field pattern and a 50 Ω impedance matching was found to be close to the edge of the Printed Circuit Board [26].

For the simulation of this type of antenna, three models with different dimensions were also drawn. Figure 6.3 shows the model and the dimensions of IFA antenna used for the simulations.

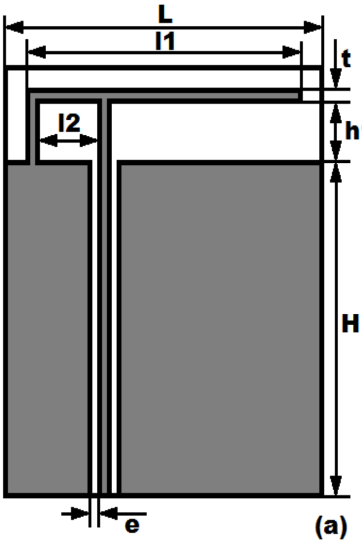

Dimension (mm)	2400 MHz	868 MHz	433 MHz
L	26	82	160
L1	23	78	156
L2	5	16	32
e	0.5	2	2
H	31	92	184
h1	5	18	36
t	1	2.3	3.7

(b)

Figure 6.3 - Model used for IFA antenna simulation: a) the antenna schematic and b) the antenna dimensions for 2400, 868 and 433 MHz.

The antenna was implemented on a 1.5 mm thick FR-4 as it is a widely used substrate. It is to notice that the IFA bandwidth increases with increasing thickness. The IFA antenna has a complex model where there is a large set of dimensions should be changed for the different frequencies. The dimensions used for the simulations were obtained at a first stage through the existing literature [27-29] and in a second stage by the optimization of these models.

After constructing the antenna models, they were simulated in open space. The usual response of the IFA antenna is illustrated in figure 6.4.

For the IFA antenna it was verified a main lobe magnitude of approximately 2.5 dB with a variation of 0.1 dB between the different frequencies and also an angular width (3 dB) of approximately 101 degrees with a main lobe direction of 358 degrees, as observed in the radiation pattern of figure 4. This antenna shows a very good response in free space with ~ 96% radiation efficiency for all three frequencies. This antenna does not show a better efficiency that the previous ones but, on the other hand, it is smaller, easier to integrate and allows implementation on the PCB where the electronic circuit is implemented.

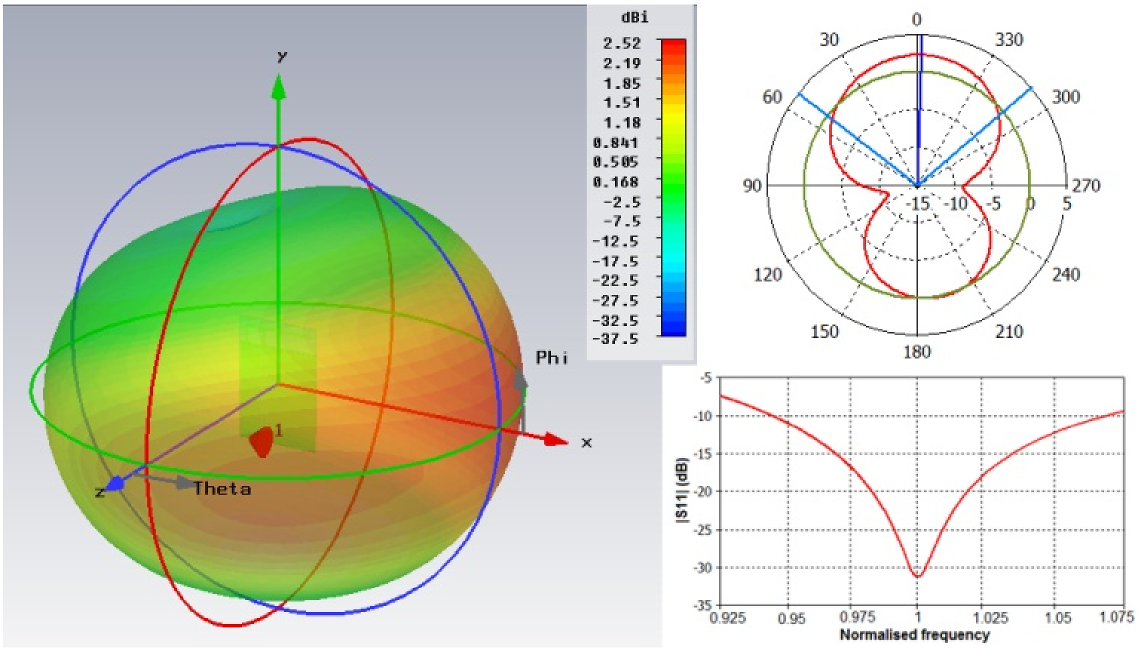

Figure 6.4 - Radiation pattern and return loss for a IFA antenna in free space for a frequency of 868MHz.

6.3. Human body model

The electromagnetic properties of human tissues shows a strong frequency dependence [29], [30]. In this way, the propagation characteristics of UHF signal will be largely affected once the antenna is placed inside the body.

To determine how the antenna response is influenced by each layer of human tissue, a spherical model was built with the antenna placed at the middle. For the simple evaluation of the influence of each human tissue layer on signal propagation, an analysis layer by layer and the simulation of various thicknesses for each layer were performed. In this way, the best position for the placement of the transition antenna can be defined for specific implementations.

Another spherical model composed by various layers that compose the hip region of human leg, including bone, was also constructed, again with the communication system in the center of the spherical model. In this case, the main purpose it to evaluate the best options for the communication system for the development of smart hip-prosthesis [31, 32]. So, based on a standard anatomy [33] the dimension used in the simulation [34] for the various layers that constitute the human hip region are shown in table 6.3.

Table 6.3 - Hip region model layer thickness [34].

Layer	**Thickness (mm)**
Skin	2
Fat	15
Muscle	40
Cortical bone	15
Antenna encapsulation	1.5

The values of the electrical conductivity (σ) (S/m) and relative permittivity (ε) for each tissue layer used in the simulation and for the antenna encapsulation are shown in table 6.4.

Table 6.4 - Tissure and encapsulation electrical parameters at 433, 868 and 2400 MHz [36].

Tissue	**Property**	**433 MHz**	**868 MHz**	**2400 MHz**
Skin	σ ε	0.70190 46.079	0.85617 41.576	1.44070 38.063
Fat	σ ε	0.04165 5.5667	0,05028 5.467	0.10235 5.2853
Muscle	σ ε	0.80484 56.873	0.93213 55.109	1.70500 52.791
Cortical bone	σ ε	0.09429 13.074	0.13950 12.484	0.38459 11.410
PDMS	σ ε	0.001 2.60	0.003 2.55	0.01 2.50

It is considered that the device is coated with a 1 mm layer of polymethylsiloxance (PDMS) as this is one of the most used materials for biocompatible encapsulations [35]. The abovementioned properties are shown in table 6.4 for the three simulated frequencies [36].

6.4. Results and discussion

After the construction of the models, the simulation at the selected frequencies for the various human tissue layers was performed using the CST MWS software and a series of graphs of radiation efficiency and power flow representative of the models response at various depths for the different layers were obtained.

The antenna radiation efficiency (e_{rad}) is defined by the ratio of gain (G) to directivity (D) or, similarly, the ratio between the radiated (P_{rad}) to accepted (input) (P_{in}) power of the antenna shown in equation 6.1:

$$e_{rad} = \frac{G(\theta,\varphi)}{D(\theta,\varphi)} \; or \; e_{rad} = \frac{P_{rad}}{P_{in}}$$

(eq. 6.1)

On the other hand, the power flow in the simulations represents the maximum value (peak value) of the power flow at every spatial point within a given period of time, being therefore a time independent result.

The study was also performed for the hip-prosthesis model which corresponds to placing the communication system inside the *femur* and evaluate the behavior of the system outside of human body to the described frequencies of 433, 868 and 2400 MHz. Although the main objective of the present study is to be as generic as possible, the implementation of a real situation helps to elucidate the potential of the developed methodology and also helps as a base for the development of a hip prosthesis monitoring system, which is already under development [13, 32].

A series of simulations at the different frequencies was then performed to verify the influence of the various layers on the communication signal. With the obtained data graphs for each different layer were created allowing best approach for the placement of a transmission system within the human body.

Figure 6.5 shows the results of the radiation efficiency for a dipole, circular and IFA antennas at 868 MHz and the figure 6.6 illustrates the radiation efficiency for IFA antenna at 433, 868 and 2400 MHz.

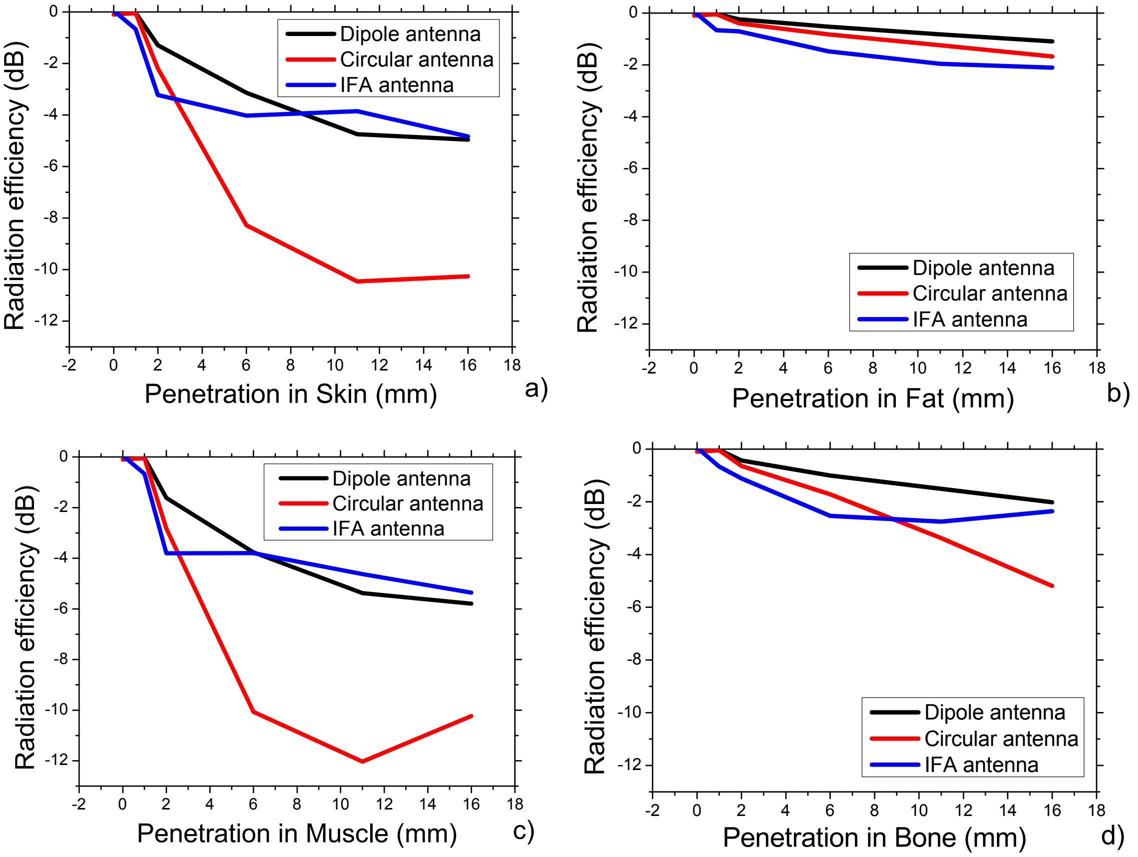

Figure 6.5 - Radiation efficiency for a dipole, circular and IFA antennas at 868 MHz: (a) Skin layer, (b) Fat layer, (c) Muscle layer and (d) Bone layer.

Figure 6.5 shows the radiation efficiency (dB) variation as a function of depth for the three antenna models and for the different tissues. The evaluated thickness of each layer is 15 mm for all layers in order to facilitate de comparative study between the layers.

For the frequency of 868 MHz (figure 6.5), the results demonstrate a larger efficiency loss in the region of the skin (figure 6.5a) and muscle (figure 6.5c) due to the larger higher σ and ε. In the case of the circular antenna, this loss is more pronounced with increasing penetration, showing also a small recovery of efficiency after 10 mm of penetration. It also verified that the IFA antenna shows a rather sharp efficiency loss in the first millimeters as compared to the others antennas. It is therefore shown that materials with low σ and ε, such as the fat layer (figure 6.5b), practically do not differences with respect to the choice of the antenna. In the case of the bone layer (figure 6.5d), it is possible to verify some differences, with the circular antenna presenting the worst performance. For higher values of electrical conductivity and larger penetration depths, the results of the dipole antenna and IFA antenna tend to converge.

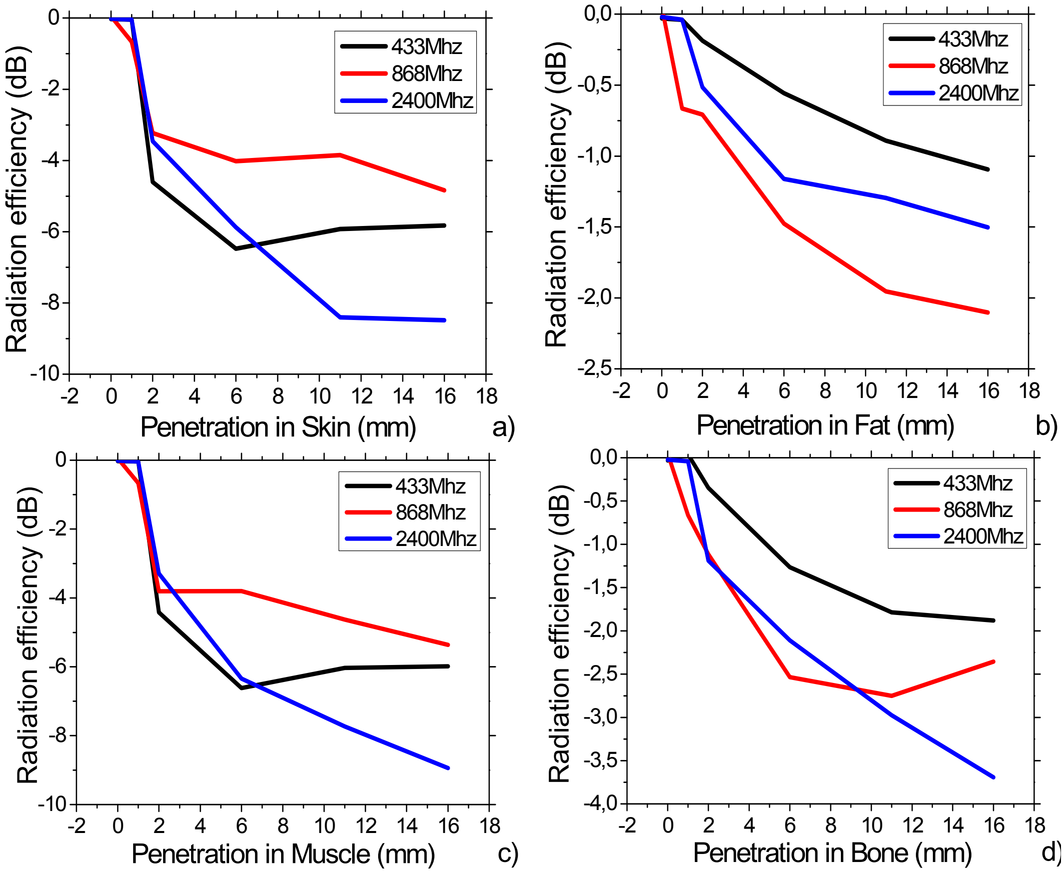

Figure 6.6 - Radiation efficiency for IFA antenna at 433, 868 and 2400MHz: (a) Skin layer, (b) Fat layer, (c) Muscle layer and (d) Bone layer.

Comparing the different frequencies (figure 6.6), the results showed similar trends, with a larger loss of efficiency in the muscle and skin regions due to the larger σ and ε values with the circular antenna showing again a more pronounced loss with increasing penetration depth. With the antenna chosen to demonstrate the frequency behavior of the various layers, it is possible to verify that the best choice in terms of frequency would be 868 MHz due to better efficiency in most critical layers.

IFA antenna presents a rather sharp loss in efficiency in the first millimeters of layer as compared to the others antenna types but compensate this loss with the increase of the penetration (figure 6.6). So, it is concluded that for materials with low σ and ε there are no substantial differences between the different types of antenna. However, for higher values and larger penetration depth in the tissue layer, it is concluded that the IFA antenna shows the best performance.

Figure 6.5 shows that the placement of the antenna influences its performance, the losses being most significant when the wavelength is much smaller than the size of object in which the antenna is inserted.

In this way the electromagnetic field inside of human body will present variations of amplitude and phase according to the frequency emitted and the body layers between the antenna and the exterior. Since the human body shows different layers with different electromagnetic properties, this leads to a phase and amplitude variation when passing between the different layers. The layers with higher σ and ε cause a larger reduction of wavelength amplitude.

With the aim of studying the behavior within the human body, simulations for the hip region were performed for of each antenna operating at the different frequencies. The results are presented in figure 6.7. In this case, the power flow (dB VA/m) versus thickness of penetration for the main lob direction along a straight line was evaluated.

Figure 6.7 shows that a higher slope in the power flow loss occurs in the layer with higher σ and ε which correspond to the muscle and skin layers. The results are common for all antenna models.

At a frequency of 433 MHz, the power flow outside the human body is approximately -15 dB on the IFA and Dipole antennas. These antennas show a similar behavior due to the similar antenna radiation characteristics. In the case of the circular antenna, a larger power loss slope was detected around 42 mm, with a later power flow recovery after 45 mm with a power flow outside the body of ~ -9 dB. Therefore, it is observed in figure 6.7a that the circular antenna has a better performance as compared to the other under consideration.

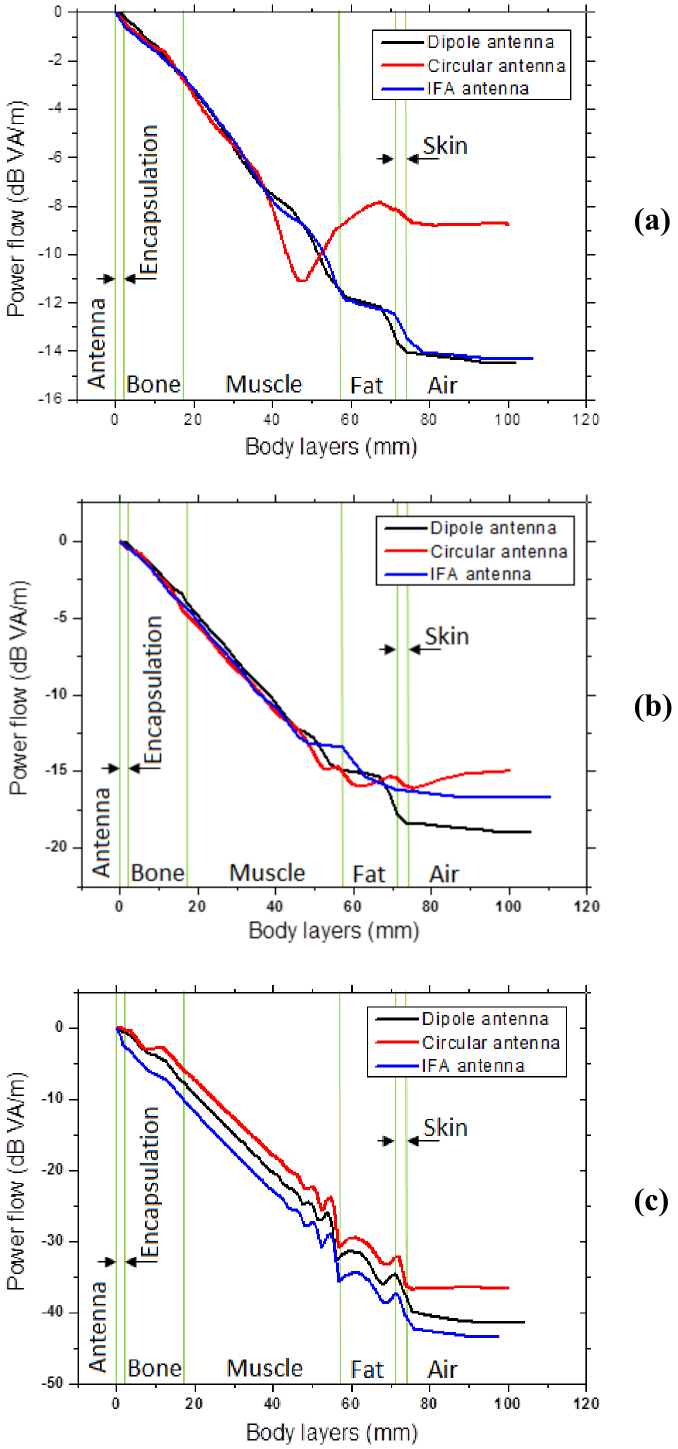

Figure 6.7 - Power flow in hip region for dipole, circular and IFA antenna at: a) 433 MHz; b) 868 MHz and c) 2400 MHz.

At a frequency of 868 MHz, the power flow outside the human body is approximately 19 dB, -17 dB and -15 dB for the dipole, IFA and circular antennas, respectively. All antennas show nevertheless a similar behavior at 50mm as shown in figure 6.7b). In the case of the circular antenna from this depth (50 mm) the same value of the power flow is maintained until the penetration into air. Thus, it is concluded that the circular antenna at 868 MHz registers along the analysis line points with higher power flow as compared with the other ones under consideration, being therefore possible to predict a good performance in the main direction.

At a frequency of 2400 MHz, the power flow outside the human body is approximately -44 dB, -41 dB and -36 dB on IFA, dipole and circular antennas, respectively. After 40 mm of penetration, an oscillation of power flow was detected. These oscillations are ascribed to phase variations in the electromagnetic wave at the interfaces, being the circular antenna more susceptible to the oscillations for operating in resonance. Figure 6.7c) shows that the circular antenna has a slightly better performance as compared to the others antennas, but with no significant differences.

It is important to note that the velocity of propagation decreases with increasing σ and ε, and also the losses in the material will affect both the near-field and the wave propagation [36].

It is verified a sharp attenuation in radiation efficiency in the first millimeter for each layer, for all studied frequencies. However, for the 433 MHz and 868 MHz the decay rate becomes lower with increasing penetration layer, and in the case of 2400 MHz the decay rate tends to remain sharper as compared to the previous frequencies.

With increasing frequency, there is an increase in the effective σ of the material (table 6.4), which causes a decrease in the propagation speed and therefore increasing propagation difficulty.

For a small penetration, the best results are registered for the dipole antenna type in all tested frequencies but for large penetrations, the IFA antenna shows good results which are similar to the ones for the dipole antenna. This fact is actually expected as the Inverted F antenna is a variation of the transmission line or bent monopole antenna, as previously mentioned. Furthermore, it is possible to verify that the circular antenna shows a reduction in efficiency difference regarding to other antennas, with the increase of model penetration, as observed in figure 6.5c).

Analyzing the influence of frequency on the power flow for the hip region, it is possible to observe an increase of power flow loss with increasing frequency. Whereas from 433 MHz to 868 MHz a small variation of approximately 3 dB was identified, from 433 MHz to 2400 MHz a variation of approximately 25 dB of power flow loss is obtained.

The radiation efficiency for all frequencies was also calculated and the results of the simulations are shown in table 6.5. Table 6.5 shows the radiation efficiency, expressed as a percentage and corresponding to the net body loss in dB for the different antenna models at 433 MHz, 868 MHz and 2400 MHz. These results show that implanting an UHF communication system in the human body for the hip region reaches an efficiency range between 10.62% and 0,109%, depending on the cases under study.

Table 6.5 - Radiation efficiency for a hip region antenna model at 433, 868 and 2400MHz

Antenna type	**433 MHz**		**868 MHz**		**2400 MHz**	
	η_b%	Body Loss (dB)	η_b%	Body Loss (dB)	η_b%	Body Loss (dB)
Dipole	7,56	11,28	6,59	11,81	0,162	27,90
Circular	5,45	12.54	5,57	12,54	0,109	29,62
IFA	8,93	10,49	10,62	9,74	0,140	28,53

The best frequency and the best antenna model for this specific application (table 6.5) is an IFA antenna operating at 868 MHz as it shows a good relationship between dimension, efficiency and transmission rate. Further, it has additional advantages for a hip prosthesis monitoring system as the antenna can be included in the PCB together with the sensor read system.

6.5. Conclusions

The electromagnetic simulation of three different types of ultra wideband antennas, dipole, IFA and circular antennas, for in-body applications has been performed for excitation frequencies of 433 MHz, 868 MHz and 2400 MHz.

The numerical simulation for electromagnetic wave propagation was carried out using Finite Integration Technique software to perform the analysis of all antennas response.

Based on the analysis is possible to note that the frequencies between 433 MHz and 868 MHz are a good solution for implantable devices, in particular closer to 868 MHz as they allow a larger transmission rate, which enhances the possibilities of implantable devices.

It is also concluded that the shape and layer where the device is placed deeply influences the performance of the system. Therefore, according to the application is important to determine the optimum position to place the device as a function of the σ and ε value corresponding to the different tissue layer to be crossed by the RF signal in order to optimize performance. In particular, it is to notice that the case of muscle layer strongly reduces the efficiency of the communication system.

By the comparison of the various antenna types it is verified that the IFA antenna and its variations will be a good solution for implantable devices, since it is easily integrated in the electronic circuit and widely used and investigated for its use in GSM.

6.6. References

[1] C. Brunckhorst, R. Candinas, and S. Furman, "Obituary: Ake Senning 1915-2000," *Journal of pacing and Clinical Electroplysiology,* vol. 23, 2000.

[2] *Spectrum, IEEE,* Title 41, *Neural engineering's image problem*, 2004, pp. 32-37.

[3] *Engineering in Medicine and Biology Society, 2003. Proceedings of the 25th Annual International Conference of the IEEE,* Title 2, *Implantable myoelectric sensors (IMES) for upper-extremity prosthesis control- preliminary work*, 2003, pp. 1562-1565 Vol.2.

[4] H. Gensler, R. Sheybani, L. Po-Ying, R. Lo, S. Zhu, Y. Ken-Tye, I. Roy, P. N. Prasad, R. Masood, U. K. Sinha, and E. Meng, "Implantable MEMS drug delivery device for cancer radiation reduction." pp. 23-26.

[5] Biomedical Engineering, IEEE Transactions on, Title 41, A telemetry-instrumentation system for monitoring multiple subcutaneously implanted glucose sensors, 1994, pp. 937-942.

[6] Engineering in Medicine and Biology Magazine, IEEE, Title 24, Bionic cardiovascular medicine, 2005, pp. 24-31.

[7] R. S. MacKay, Bio-Medical Telemetry: Sensing and Transmitting Biological Information from Animals and Man: Wiley, 1998.

[8] Selected Areas in Communications, IEEE Journal on, Title 27, Cooperative Communications in Ultra-Wideband Wireless Body Area Networks: Channel Modeling and System Diversity Analysis, 2009, pp. 5-16.

[9] Consumer Electronics, IEEE Transactions on, Title 56, Improved performance of UWB system for wireless body area networks, 2010, pp. 1373-1379.

[10] E. R. C. (ERC). "The European Table of Frequency Allocations and Utilisations Covering the Frequency Range 9 kHz to 275 GHz," 2012.

[11] T. Weiland, “A Discretization Method for the Solution of Maxwell's Equations for Six-Component Fields,” *Electronics and Communications AEUE,* vol. 31, pp. 116-120, 1977.

[12] M. Clemens, and T. Weiland, “Discrete Electromagnetism with the Finite Integration Technique,” *Progress In Electromagnetics Research,* vol. 32, pp. 65-87, 2001.

[13] A. Ahlbom, U. Bergqvist, J. H. Bernhardt, J. P. Cesarini, L. A. Court, M. Grandolfo, M. Hietanen, A. F. McKinlay, M. H. Repacholi, D. H. Sliney, J. A. J. Stolwijk, M. L. Swicord, L. D. Szabo, M. Taki, T. S. Tenforde, H. P. Jammet, R. Matthes, and P. Int Commission Nonionizing Radiation, “Guidelines for limiting exposure to time-varying electric, magnetic, and electromagnetic fields (up to 300 GHz),” *Health Physics,* vol. 74, no. 4, pp. 494-522, Apr, 1998.

[14] J. D. Kraus, and R. J. Marhefka, *Antennas for all applications*: McGraw-Hill, 2002.

[15] P. S. Kildal, *Foundations of Antennas: A Unified Approach*: Professional Publishing Svc., 2000.

[16] C. A. Balanis, *Antenna Theory: Analysis and Design*: John Wiley & Sons, 2005.

[17] D. Mandal, M. A. I. Ansari, R. Kar, and S. P. Ghoshal, “Non-uniform Concentric Circular Antenna Array Design using IPSO Technique for Side Lobe Reduction,” *Procedia Technology,* vol. 6, no. 0, pp. 856-863, 2012.

[18] S. Mondal, and P. P. Sarkar, “Wideband Bidirectional Planar Shorted Circular Monopole Antenna,” *Procedia Technology,* vol. 4, no. 0, pp. 421-426, 2012.

[19] L. Zhan, and Y. Rahmat-Samii, “Optimization of PIFA-IFA combination in handset antenna designs,” *Antennas and Propagation, IEEE Transactions on,* vol. 53, no. 5, pp. 1770-1778, 2005.

[20] L. Jianxin, C. C. Chiau, C. Xiaodong, and C. G. Parini, “Study of a printed circular disc monopole antenna for UWB systems,” *Antennas and Propagation, IEEE Transactions on,* vol. 53, no. 11, pp. 3500-3504, 2005.

[21] K. J. Vinoy, K. A. Jose, and V. K. Varadan, "Multi-band characteristics and fractal dimension of dipole antennas with Koch curve geometry." pp. 106-109 vol.4.

[22] W. G. Scanlon, J. B. Burns, and N. E. Evans, “Radiowave propagation from a tissue-implanted source at 418 MHz and 916.5 MHz.,” *IEEE transactions on bio-medical engineering,* vol. 47, pp. 527-34, 2000.

[23] C. Furse, “Design an antenna for pacemaker communication,” *Microwaves & Rf,* vol. 39, no. 3, pp. 73-+, Mar, 2000.

[24] A. Khaleghi, and I. Balasingham, “On the Ultra Wideband Propagation Channel Characterizations of the Biomedical Implants,” *VTC Spring 2009 - IEEE 69th Vehicular Technology Conference*, pp. 1-4, 2009.

[25] A. Eesuola, Y. Chen, and G. Y. Tian, “Novel Ultra-Wideband Antennas for In-Body Wireless Communication and Medical Imaging Applications,” vol. 2, pp. 3129-3132, 2011.

[26] D. M. Pozar, *Microwave Engineering, 3Rd Ed*: Wiley India Pvt. Limited, 2009.

[27] *Vehicular Technology Conference, 2004. VTC 2004-Spring. 2004 IEEE 59th,* Title 1, *Small wideband PIFA for mobile phones at 1800 MHz*, 2004, pp. 27-29 Vol.1.

[28] Z. Zhang, *Antenna Design for Mobile Devices*: Wiley, 2011.

[29] C. Gabriel, "Compilation of the Dielectric Properties of Body Tissues at RF and Microwave Frequencies." p. 21.

[30] IFAC-CNR, “Calculation of Dielectric Properties of Body Tissues in the frequency range 10Hz – 100GHz,” *1997-2012*, 2012.

[31] P. Alpuim, V. Correia, E. S. Marins, J. G. Rocha, I. G. Trindade, and S. Lanceros-Mendez, “Piezoresistive silicon thin film sensor array for biomedical applications,” *Thin Solid Films,* vol. 519, no. 14, pp. 4574-4577, 2011.

[32] D. D. D'Lima, S. Patil, N. Steklov, J. E. Slamin, and C. W. Colwell Jr, “Tibial Forces Measured In Vivo After Total Knee Arthroplasty,” *The Journal of Arthroplasty,* vol. 21, no. 2, pp. 255-262, 2006.

[33] I. C. o. R. P. T. G. o. R. Man, *Report of the Task Group on Reference Man: a report*: Pergamon Press, 1975.

[34] I. SAS. "Human anatomy, medical imaging and illustrations," 10-10-2012, 2012;

[35] M. Ionescu, B. Winton, D. Wexler, R. Siegele, A. Deslantes, E. Stelcer, A. Atanacio, and D. D. Cohen, “Enhanced biocompatibility of PDMS (polydimethylsiloxane) polymer films by ion irradiation,” *Nuclear Instruments and Methods in Physics Research Section B: Beam Interactions with Materials and Atoms,* vol. 273, pp. 161-163, 2012.

[36] IFAC-CNR. "Dielectric Properties of Body Tissues," 24-10-2012, 2012.

7. Conclusions and future work

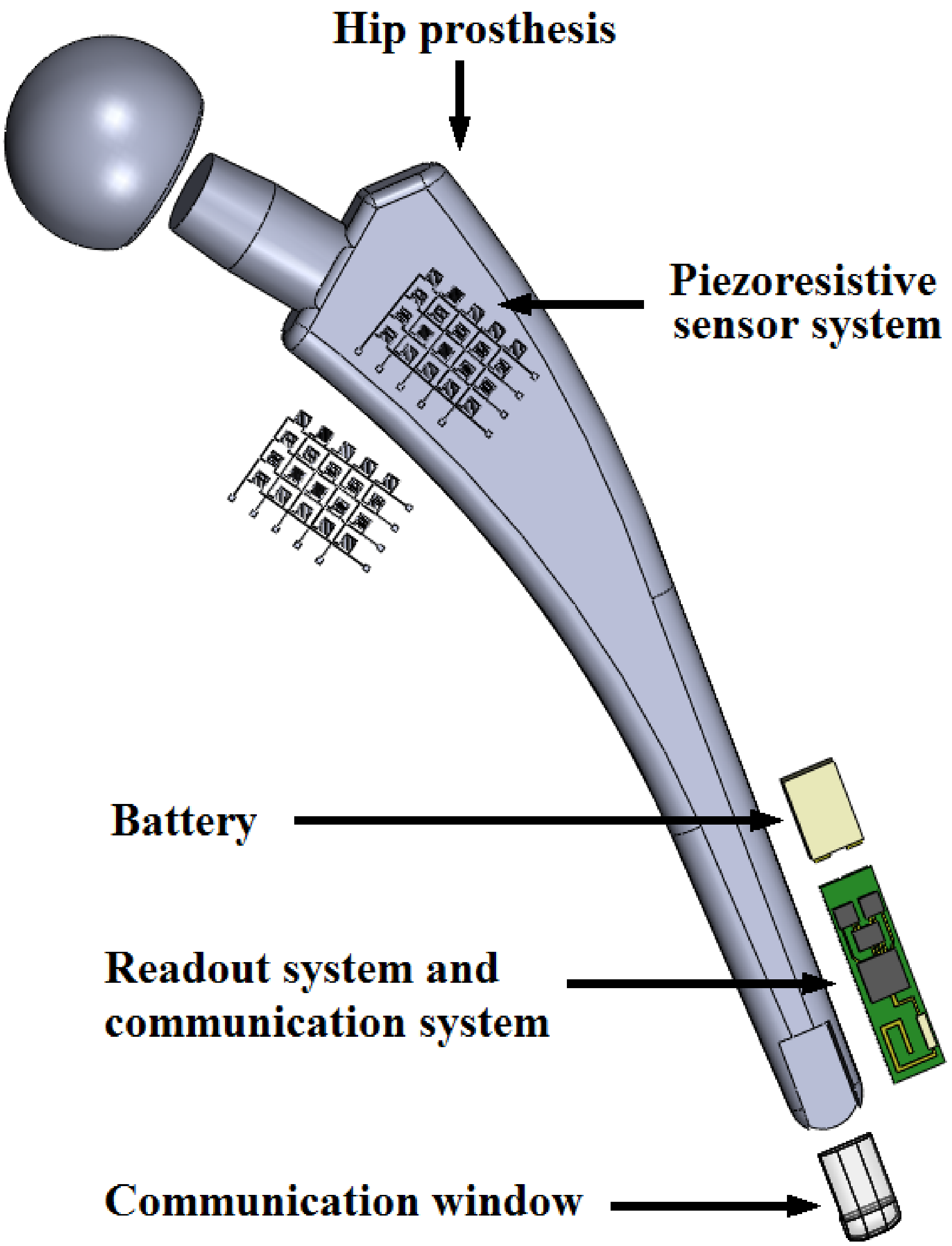

7.1. Conclusions

The main objective of this work was the development of a flexible matrix of piezoresistive sensors for the measurement of strain and force. In particular, it was focused in biomedical applications and most specifically in the implementation of a smart implantable hip prosthesis.

To meet this objective it was necessary to develop the following specific tasks:

- a piezoresistive flexible sensor matrix for the measurement of strain and forces;
- a test system for the sensors simulating real use conditions;
- a matrix sensor readout system, able to adapt to the particular sensor to be measured.
- a wireless communication system for biomedical applications;

As a conclusion, the main achievements in the different tasks and in the overall work were the following:

Flexible strain sensors based on the piezoresistive property of n^+-nc-si:H thin films were fabricated using hot-wire chemical vapor deposition (HWCVD) at 150 ºC on a polymeric substrate, using standard lithographic technics to make the patterns of the sensors. The sensors show a gauge factor of -28, for low frequency deformation cycles.

Further, ink-jet printed piezoresistive sensors were developed and characterized by electro-mechanical measurements under 4-point bending mechanical solicitation. Sensors based on silver nanoparticles and sensors based on PeDot were printed in polymer substrates in the form of single sensors, arrays and matrix of 4 x 5 sensors. Gauge factor up to 2,5 were obtained with excellent reproducibility in sensors with a 1.8 x 1.5 mm^2 active area.

Electro-mechanical tests were conducted in order to characterize and validated the response of the various sensors under conditions similar to the ones corresponding to a real use in hip-prosthesis implants. Therefore, a prosthesis coated with the developed sensors was produced, cemented on a metallic support and subject to a number of deformation cycles in an universal mechanical testing machine at three different levels of exerted forces according to the standard ISO7206.

A finite element simulation of the experimental test was previously performed in order to better select the placement of the sensors and to validate the obtained experimental results.

All developed sensors -silicon, silver ink and PeDot ink based sensors - proven to be suitable for the intended application, reacting with variation of the electrical resistance to the mechanical solicitation in a suitable, systematic and reproducible way..

Due to the different characteristics of the sensors that a sensor network can present, an adaptive readout system for piezoresistive sensors was developed. The readout system allows the reading of a maximum of 8x8 sensors, but it is scalable to a larger number of sensors by increasing the number of inputs of the multiplexer.

This system is able to measure piezoresistive sensors with a broad R0 value from 50Ω to 100 kΩ, with a maximum readout rate of 2 kHz, meeting the requirements defined for the application.
Moreover, the implementation area for the adaptive multi-sensor interface circuit is 135 mm^2, which is compatible for in-body biomedical applications. Energy consumption was also optimize by adding the option to store in the internal memory the recorded data and sending them just when the memory is full. The system goes into sleep mode between the measurements turning off all circuit. In this mode, the MCU is just active with timer interrupt wake-up.

The read circuit was experimentally validated with a test on the sensor matrix.

Finally, simulations were performed in order to evaluate the best options for the implementation of a wireless communication system for bio-applications.

Three possible ranges of working frequencies and three different types of standard antennas were considered. The communication system was introduced into a model simulating the various layers constituting the human body.

The simulations allowed defining the frequencies range most appropriate for implantable devices, as well as, the type of antenna most appropriate for this environment. It was also possible to evaluate the influence of the different tissue layers on the communication signal, helping the decision of the best placement of the antenna for a given application.

The best results for the case under consideration were obtained for an IFA antenna working at 868 MHz.

Therefore, all subsystems necessary for the development of a smart hip prostheses, sensors, readout and communication systems, were successfully developed.

7.2. Future work

Despite of the successful development of the prototype, several steps should be implemented for further improve the systems and allow a commercial product.

Thus, for a future work, it is recommended to implement a passive or even an active encapsulation for the sensors allowing to accelerate osseo-integration and thereby reducing the post-operative period.

The in vivo tests are needed to evaluate the behavior of the developed system in a real environment.

To monitor the behavior of the system in real time, it is necessary to develop a dedicated platform for receiving data. This platform will follow the patient all the time during the most critical postoperative period. It can also incorporate an internet communication system enabling the monitoring in real time by the doctor.

In a final stage it will be also important to establish a partnership with a company producing hip prosthesis for suitable product engineering for the integration and production of the equipment, as well as to undertake the necessary certification for this type of equipment's.